Dissertation

submitted to the

Combined Faculties of the Natural Sciences and Mathematics

of the

Ruperto-Carola-University of Heidelberg, Germany

for the degree of

Doctor of Natural Sciences

Put forward by

Marc Schuh

born in Bergisch Gladbach, Germany

Oral examination: 22 May 2019

Simulations of the image charge effect in high-precision PENNING traps and the new IGISOL ion buncher

Referees:

Prof. Dr. Klaus Blaum
Prof. Dr. Yuri A. Litvinov

Zusammenfassung

Simulationen des Spiegelladungseffekts in hochpräzisions Penning-Fallen und des neuen IGISOL Ionen Pulsers

Penning-Fallen sind die vorläufige Spitze einer langen Entwicklung in der Massenspektrometrie, die um 1900 begonnen hat. Mit einer relativen Genauigkeit von bis zu 10^{-12} erlauben Penning-Fallen durch Massenmessungen das Testen verschiedener physikalischer Theorien wie zum Beispiel der Quantenelektrodynamik (QED), des CPT-Theorems (für englisch charge, parity, time = Ladung, Parität, Zeit) und der speziellen Relativitätstheorie.
Um diese Genauigkeit zu erreichen, müssen viele Geräte aufeinander abgestimmt und Messungen häufig wiederholt werden. Diese Aufgabe wird durch Computer übernommen. Diese Arbeit stellt die Grundstruktur eines neu entwickelten und auf Python basierendem Kontrollsystem für das Experiment THe-Trap am Max-Planck-Institut für Kernphysik in Heidelberg, Deutschland, vor. Bei der Entwicklung wurde der Fokus darauf gelegt, dass der Benutzer mit einem Blick auf das Kontrollsystem erkennen kann, in welchem Zustand sich das Experiment befindet. Zudem ist es möglich, mit externen, ebenfalls auf Python basierenden Skripts das Experiment zu steuern und zu automatisieren.
Hochpräzisions Penning-Fallen Experimente weltweit mit der oben beschriebenen Genauigkeit werden unter anderem durch den sogenannten Spiegelladungseffekt limitiert. Dieser Effekt wird durch die Spiegelladungen hervorgerufen, welche das Ion in den umgebenden Elektroden der Penning-Falle induziert. Diese Spiegelladungen erzeugen ein zusätzliches elektrisches Feld, welches die Eigenfrequenz des Ions und dadurch das Messergebnis systematisch verschiebt. Diese Arbeit stellt eine numerische Berechnung des Spiegelladungseffekts für verschiedene Experimente mit Hilfe der Finiten-Elemente-Methode unter Benutzung von COMSOL multiphysics™ vor. Die Ergebnisse der Simulation haben eine Unsicherheit von 1 % und stimmen mit den Messergebnissen, die eine Genauigkeit von ca. 5 % haben, überein.
Flugzeitmessungen zeigen ihre Stärke bei der Massenbestimmung von kurzlebigen Nukliden mit einer Halbwertszeit von unter 100 ms. Dabei werden Ionen mehrfach reflektiert, um die Flugstrecke zu verlängern, was den Geräten den englischen Namen multi-reflection time-of-flight mass spectrometer (MR-ToF MS) eingebracht hat. Zudem dienen sie als schneller Massenseparator. Jedoch benötigen MR-Tof MS Ionenpulse mit einer zeitlichen Ausdehnung von etwa 100 ns oder kürzer. In dieser Arbeit wurde für das Experiment IGISOL in Jyväskylä, Finnland, ein Ionenpulser unter Benutzung von SIMION entwickelt, gebaut und getestet. Beim Test konnte eine Pulsbreite von 107 ns erreicht werden.

Abstract

Simulations of the image charge effect in high-precision Penning traps and the new IGISOL ion buncher

Penning traps are currently the most precise mass measurement devices resulting from a long development, which started around 1900. With a relative precision of up to 10^{-12}, Penning traps allow testing of various physical theories by means of mass measurements, such as quantum electrodynamics (QED), the CPT (charge, parity and time) theorem and theory of special relativity.
In order to achieve this precision, many devices have to be coordinated and measurements have to be performed repeatedly. This work presents the basic structure of a newly-developed Python based control system for the THe-Trap experiment at the Max-Planck-Institute for Nuclear Physics in Heidelberg, Germany. During the development the focus was placed on enabling the user to recognize the state of the experiment at just one glance. It is also possible to control and automate the experiment with external scripts based on Python as well.
High-precision Penning trap experiments worldwide with the above-mentioned precision are limited among other things by the so-called image charge effect. This effect is caused by the image charges induced by the ion in the surrounding electrodes of the Penning trap. These image charges generate an additional electric field, which systematically shifts the frequency of the ion and thus the measurement result. This thesis presents a numerical calculation of the image charge effect for various experiments using the finite element method in COMSOL multiphysics™. The results of the simulation have an uncertainty of 1 % and agree with the measurement results, which have an uncertainty of about 5 %.
Time-of-flight measurements show their strength in determining the mass of short-lived nuclides with a half-life of less than 100 ms. Ions are reflected several times to extend the flight distance, which has given the instruments the name multi-reflection time-of-flight mass spectrometer (MR-ToF MS). They also serve as fast mass separators. However, MR-Tof MS require ion pulses with a temporal width of about 100 ns or shorter. In this work, an ion buncher using SIMION was developed, built, and tested for the IGISOL experiment in Jyväskylä, Finland. During the test a pulse width of 107 ns could be achieved.

Contents

List of Figures

List of Tables

1. Introduction

Physics is the best description of the basic phenomena of nature by using the language of mathematics. It spans from the biggest objects in the Universe, like galaxies, black holes and stars, to the smallest, like atoms, protons, neutrons, electrons, neutrinos etc. Physics also investigates the question of our existence. From the moments after the Big Bang, when only hydrogen, helium and a bit of lithium existed, it was a long way to create all the elements, we consist of. In all approaches to describe the world surrounding us, it is essential to know the mass of its constituents of matter. Mass measurements offer the opportunity to test several physical theories and help to explain the way our world looks like. They can test the equivalence between mass and energy, between matter and anti-matter and contribute in the understanding of nucleosynthesis. In the following a short historical development of mass measurements up to the present is given. This is followed by various applications of mass measurements for stable and unstable nuclides and their current limitations.

1.1. History of atomic mass measurements

In 1907 Thomson built a spectrograph with parallel magnetic and electric fields. This spectrograph had a mass resolving power of $R = 10 - 20$, which is defined as

$$R = \frac{m}{\Delta m} \quad , \tag{1.1}$$

where m is the mass and Δm is the full width at half maximum (FWHM) of the line in the measured spectrum. In 1913 he discovered that neon exists with a mass number A of 20 and 22. This was the discovery of isotopes. In 1919, Thomson's student Aston further improved this device by being able to focus his apparatus on ions of the same species but with different velocities. He found that hydrogen has a mass of 1.008 u instead of 1 u [Ast20]. This led to the discovery of the mass defect. The mass defect means, that the nucleus is lighter than the summed masses of its constituents. At that time, the atomic mass unit u was defined as one sixteenth of the mass of ^{16}O, i.e. $1\,\mathrm{u} = 1/16 \cdot \mathrm{m}(^{16}\mathrm{O})$. The "missing" mass is transformed into the nuclear binding energy. From this, the astronomer Eddington concluded the nuclear synthesis and the mechanism how energy is produced in the sun [Edd20]. In 1937 Aston could improve the mass resolving power with a second order focusing mass spectrograph to $R = 2000$ [Ast37]. The improvement in mass resolving power also led to an increased precision in the determination of atomic masses
Figure 1.1 shows the development of the the mass uncertainty of tritium over time. With the second order focusing mass spectrograph even finer deviations in nuclear masses from integers of hydrogen mass could be observed, revealing the first nuclear shell structures and nuclear magic numbers [Els33]. This device was developed further by improving the geometry of the

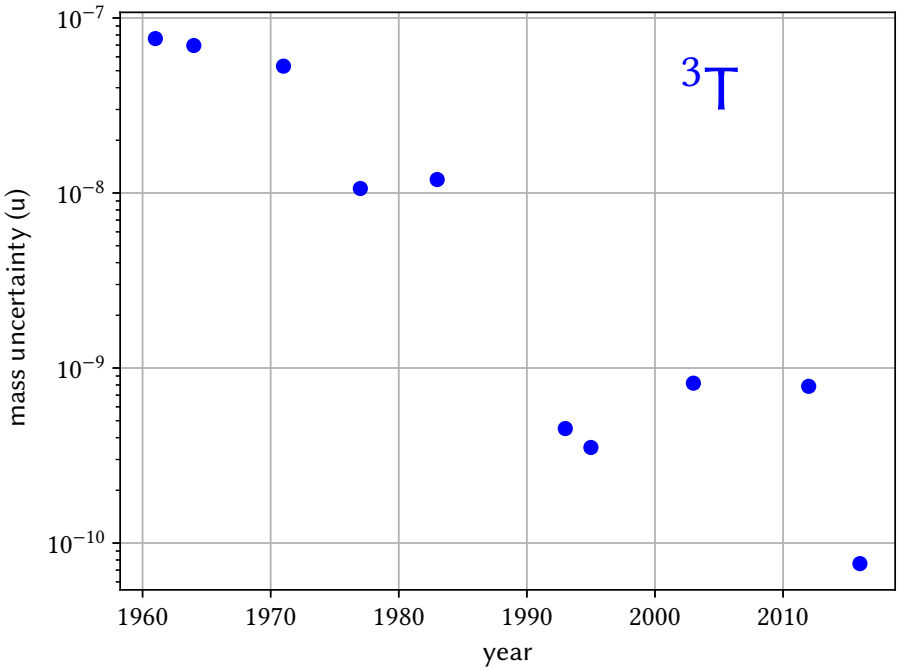

Figure 1.1.: Showing the mass uncertainty of tritium from the atomic mass evaluation (AME) over time. The increase of the mass uncertainty from 1995 to 2003 is probably based on different judgments by the evaluators of the AME. Data and explanation of the increase are from Reference [Hua19].

device until the late 1950s and a mass resolution of up to 200,000 could be achieved [Nie55]. At CERN in 1970 for the first time such a mass spectrometer was connected to an accelerator to measure the mass of unstable nuclides [KPT+73]. In the same year, Dehmelt and co-workers at the University of Washington had the idea to use a Penning trap for a measurement of the magnetic moment anomaly [WED73, vDSD87]. Afterwards, Penning traps quickly established themselves as high-precision mass spectrometers. In 1980 Kluge at the University of Mainz had the idea to use Penning traps for the measurement of radioactive nuclides at ISOLDE/CERN and could thus achieve a mass resolving power exceeding one million, which even allowed to resolve excited nuclear states, so-called isomers [SBB+90]. The concept of the Penning trap was for the first time used for mass measurements of stable nuclides, in this case for protons, by Van Dyck Jr. at the University of Washington [vDMFS86]. The mass measurement of molecules at the Massachusetts Intitute of Technology by Pritchard at an uncertainty level of 10^{-10} [CWB+89] and the measurement of anti-protons at Harvard University by Gabrielse [GPQ+95] followed. Dehmelt was awarded together with Paul and Ramsey the Nobel Prize in 1989. The first two received it "for the development of the ion trap technique" [oS89]. The latter one "for the invention of the separated oscillatory fields method and its use in the hydrogen maser and other atomic clocks" [oS89].

1.2. Today's motivation for high-precision mass measurements

As already described in the previous section, precise mass measurements have led to significant discoveries in physics. In the following current research fields of mass spectrometry are presented.

1.2.1. Charge, parity, and time reversal symmetry

The charge, parity, and time (CPT) reversal symmetry theorem states that physics is invariant under the simultaneous transformation of charge conjugation, parity transformation and time reversal. Therefore, the charge-to-mass ratio for a particle and its antiparticle must be identical except for the sign. This is confirmed for the ratio between anti-protons and H^- at a level of 10^{-12} [USM+15]. Similarly, the magnetic moment of protons and anti-protons in a PENNING trap was compared and found to be equal [SSH+17, SMB+17] at a level of $8 \cdot 10^{-7}$.

1.2.2. Quantum electrodynamics

The previously mentioned magnetic moment, characterized by the so-called g-factor, opens up the possibility to test another physical theory. The g-factor depends among other parameters also on the mass of the investigated ion and the mass of the electron. The value of g can be predicted by quantum electrodynamics (QED) for hydrogen-like ions with low nuclear charge numbers such as oxygen or carbon at a level of $1 \cdot 10^{-11}$ [PCJY05]. Measurements of the g-factor in PENNING traps can confirm the value or are even more accurate [HBH+00, VDacS+04]. If the QED theory is assumed to be correct, the mass of the electron can be determined from the measurements, to be better than one part-per-billion [SKZ+14]. For ions with higher nuclear charge numbers such as silicon, nuclear effects become larger. Here, the PENNING-trap experiments with an uncertainty of $5 \cdot 10^{-11}$ are even an order of magnitude better than the theoretical predictions [SWK+13].

1.2.3. Neutrino mass

The observed neutrino oscillations [FHI+98] indicate that at least two of the three neutrino eigenstates have a mass. Additionally, a hierarchy of the masses can be concluded from experiments. However, the determination of a single mass is not possible by the oscillation experiments as they can only determine the difference of the masses squared. In a PENNING trap the mass of a neutrino also cannot be determined directly, but the trap can make a substantial contribution to the mass determination efforts as described in the following.
The decay of tritium ^{3}T to helium-3 ^{3}He can be described by the process:

$$^3\mathrm{T} \rightarrow {}^3\mathrm{He}^+ + e^- + \bar{\nu}_e + E_0 \quad . \tag{1.2}$$

The released energy E_0 is distributed between the electron e^-, the helium-3 and the anti-electron neutrino $\bar{\nu}_e$. The Karlsruhe-Tritium-Neutrino-Experiment (KATRIN) is a large electron spectrometer [BBE+17]. The goal is to reduce the upper limit of the anti-electron neutrino mass to $0.2\,\mathrm{eV/c^2}$. To achieve this the endpoint of the energy spectrum of the electron emitted in

the decay has to be determined with a precision of 6 meV [Ott10]. The shape of the spectrum depends, among other parameters, on the Q-value of the reaction. The Q-value in this case is:

$$Q = (m_{^3\mathrm{T}} - m_{^3\mathrm{He}})\,c^2 = E_0 + m_{\bar{\nu}_e} \cdot c^2 \quad , \tag{1.3}$$

where $m_{^3\mathrm{T}}$ is the atomic mass of tritium, $m_{^3\mathrm{He}}$ the atomic mass of helium-3 and $m_{\bar{\nu}_e}$ the mass of the anti-electron neutrino. KATRIN will measure the energy of the emitted electron near its endpoint. The resulting spectrum will be fitted and among other parameters, e.g. the endpoint, it will also return the Q-value for the decay of tritium from the shape of the spectrum.
The measurement of KATRIN is prone to systematic errors. Here, Penning-trap mass spectrometry can help, by providing a Q-value from the mass-ratio measurement of tritium to helium-3. The best Q-value measurement for this reaction has an uncertainty of $4 \cdot 10^{-6}$, which required a mass ratio measurement uncertainty at the level of $6 \cdot 10^{-11}$ [Mye13]. Thus, it serves as a model-independent test. The determination of the tritium decay Q-value was also the goal of THe-Trap (short for tritium-helium-trap, see Section 4.2), where part of this thesis was carried out.

1.2.4. Nuclear models

The genesis of matter in stars is one of the most important fields of nuclear astrophysics. The reliability of the astrophysical models for the processes that create matter is based on the knowledge of the properties of the involved, short-lived nuclides. These include, for example, their half-life, mass and various particle capture cross sections. The formation of heavier elements is considered to be driven mostly by these processes:

1. the slow neutron capture, called s-process [LHL+03],
2. the rapid neutron capture, called r-process [AGT07, MSMA16],
3. the rapid proton capture, called rp-process [SAG+98].

Most of the heavier elements are formed when a star reaches its end of lifetime or in an accretion disk around a black hole. In the r- and rp- processes nuclei are involved which are either extremely neutron deficient (rp-process) or neutron rich (r-process). Studying the properties of the nuclei involved is thus quite challenging, because their production rate is low and they decay quickly (half-life < 1 s). But especially knowing their mass is crucial to test models of the nucleosynthesis in stars [WHW02].

1.3. Current limitations

The applications of Penning traps presented previously suffer from different limitations which make further progress difficult. These limitations are presented separately for Penning traps dedicated for stable and radioactive nuclides below.

1.3.1. Mass measurement of stable isotopes

For stable mass doublets the greatest limitations are magnetic field and voltage fluctuations as well as the reproducibility of the ion's position in the trap as the magnetic and electric field is highly position dependent at this level of precision. The magnetic field fluctuations can be well compensated by simultaneous measurement of the cyclotron frequency of two ions, as it is the case with PENTATRAP [RBCLU+12, Ris18]. Voltage fluctuations can also be detected and corrected by observing a third ion's axial frequency. All systematic effects are thereby highly suppressed.

For ion pairs with the same mass but different charge positioning problems arise as different voltages are often required to store and detect the ions. This results in different positions of the ion within the magnetic field. In most cases this leads to a systematically different magnetic field for the two ions and thus to a systematic shift, which must be corrected. This problem can be circumvented by two detection circuits matching for the ion's frequencies at the same voltage setting [HKLR+17].

For ion pairs with different charge-to-mass ratios, there are many other shifts, such as the dependency of frequency on ion motion amplitude, influence of detection system on frequency, tilting and ellipticity of the trap. All these shifts can be tuned away leaving the image charge shift (ICS) as the dominant one. This shift is caused by the image charges which are induced by the ion in the trap on the surface of the electrodes. These charges generate an additional electric field which systematically shifts the frequency of the ion and thus the final result. The effect dominates all other systematic uncertainties by a factor of

- 30 for the g-factor of $^{28}Si^{13+}$ [SWK+13].
- 120 for the mass of the electron [SKZ+14].
- 3 for the mass of the proton [HKLR+17].

This work presents a successful approach to calculate the ICS by using COMSOL MULTIPHYSICS™. The uncertainty in the prediction of the ICS is lowered to 1 % and can confirm already existing experimental results. See Section 2.2.1 for the theory of the ICS and Chapter 6 for its simulation.

Additionally, the technical complexity of the PENNING-trap experiments increases constantly and therefore a computer control system is essential. In Chapter 5 the new PYTHON based control system for the experiment THE-TRAP (see Section 4.2) is presented. It shows the user at a glance the current status of the experiment and offers the opportunity to write and perform PYTHON scripts during the run time of the control system. These scripts can control a measurement campaign autonomously and the control system takes care automatically of most of the documentation necessary for the analysis later on.

1.3.2. Mass measurement of radioactive isotopes

PENNING traps dedicated for mass measurements of short-lived ions work on different principles than the traps for stable ions and face different challenges. If stable nuclides are measured, contamination by other nuclides is usually not a problem. Most of the radioactive isotopes decay quickly and therefore they have to be produced continuously at the experiment during

the measurement campaign. In addition to the desired nuclide many unwanted nuclides are produced, too. These other nuclides interfere with the measurement and therefore an efficient and fast cleaning process is necessary.
For the cleaning and for the mass measurements of nuclides with a half-life time below 100 ms multi-reflection time-of-flight mass spectrometer (MR-ToF MS) became the tool of choice within the last years. The MR-ToF MS can separate the ions of interest from the contamination in the beam and send them either to other experiments, such as a PENNING trap or perform the mass determination itself. This work presents the development of an ion buncher for the IGISOL experiment. This new buncher should create ion pulses with a time and energy spread below 100 ns and 40 eV, respectively. The buncher is designed using SIMION. These short bunches are an essential requirement for the planned MR-ToF MS. The IGISOL experiment is introduced in Section 4.1. The simulation and the successful experimental characterization of the ion buncher is presented in Chapter 7.

2. Theory of ion traps

This chapter introduces three types of traps for the storage and manipulation of ions. The first Section 2.1 deals with PENNING traps, where one or a few ions are stored in a superposition of a static electric and a static magnetic field. A measurement of the ion's characteristic oscillation frequencies in the trap allows for many applications (see Section 1.2). In the ideal PENNING trap, several assumptions are made, for example infinitely large electrodes, perfectly harmonic fields and ideal alignment, which cannot be guaranteed in reality. In a real PENNING trap (see Section 2.2) these deviations from the ideal case need to be quantified in order to correct for systematic shifts in the oscillation frequencies and to reach the highest precision (see Section 1). Here, this thesis focuses on the image charge shift (ICS) (see Section 2.2.1), which is presently the largest systematic uncertainty in many PENNING-trap experiments worldwide.

In Section 2.3 the PAUL trap is introduced. In contrast to the PENNING trap, a PAUL trap uses a combination of a static and a high-frequency alternating electric field to confine ions. In recent years, its application as a purely electrical ion cage has led to many scientific breakthroughs especially in quantum information [SVWP14] and for fundamental studies like weak interaction in nuclear physics [Her03]. Here, with respect to applications in nuclear physics, this thesis distinguishes between a two-dimensional PAUL trap (see Section 2.3.1) and its expansion to three dimensions (see Section 2.3.2). Especially for the application in nuclear physics a cooling of ions with up to 50 - 100 eV kinetic energy is essential. In order to be widely applicable, the cooling process in a PAUL trap should be largely independent of the ion's mass and charge state. This requirement is fulfilled by buffer gas cooling (see Section 2.3.2).

The third trap introduced in this chapter is the electrostatic ion beam trap (EIBT) used as multi-reflection time-of-flight mass spectrometer (MR-ToF MS) (see Section 2.4). It extends the flight path of ions by reflecting them back and forth between electrostatic mirrors. It is a purely electrostatic device, which separates a bunch of ions by making use of the concept that ions with the same kinetic energy but different masses separate due to their different velocity after a certain time. This device has recently started to massively contribute to the mass determination of short lived nuclei [WWA+13, WBB+13, DPB+15].

2.1. Ideal PENNING trap

A PENNING trap is used to store one or many charged particles as electrons, protons, their antiparticles and molecules in ultra-high vacuum for up to months [SMF+15] and to link the particles' oscillation frequencies in the confining potential to its charge-to-mass-ratio [BG86]. In the following only the case of a single ion is investigated, which eliminates the need to analyze ion-ion interaction [RMSM06]. The confining potential is a combination of a homogeneous magnetic field $\vec{B} = B_0\vec{e}_z$, usually generated by a superconducting magnet and an electrostatic

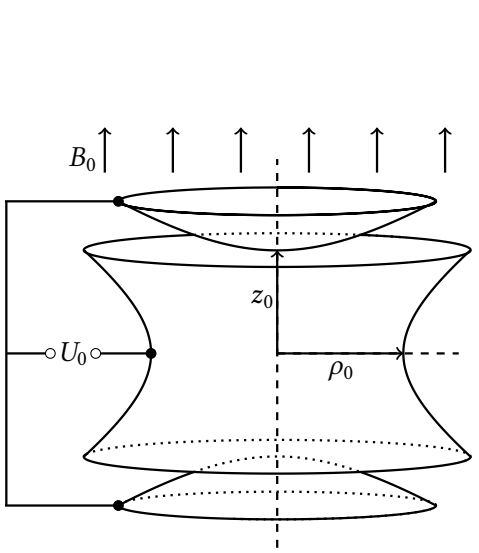

(a) Sketch of an ideal hyperbolic PENNING trap.

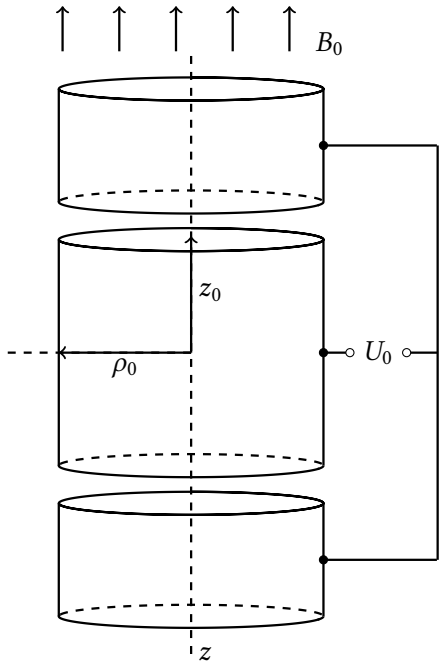

(b) Sketch of an ideal cylindrical PENNING trap.

Figure 2.1.: Sketch of two versions of an ideal PENNING trap. Both consist of two end caps and one ring electrode. The direction of the magnetic field B_0 is indicated by the arrows. The voltage U_0 is applied between the end caps and the ring electrode. In both traps the characteristic dimensions z_0 and ρ_0 are indicated. The vertical and horizontal dashed line indicate the z- and radial axis, respectively.

quadrupole potential Φ_2:

$$\Phi_2(z, \rho) = \frac{U_0 C_2}{2d^2}\left(z^2 - \frac{\rho^2}{2}\right) \quad . \tag{2.1}$$

Here, $\rho = \sqrt{x^2 + y^2}$ and d is the characteristic trap parameter, related to the other characteristic dimensions ρ_0 and z_0 (see Figure 2.1a and 2.1b) via

$$d = \sqrt{\frac{1}{2}\left(z_0^2 + \frac{1}{2}\rho_0^2\right)} \quad . \tag{2.2}$$

The dimensionless constant C_2 is usually close to unity for hyperbolic PENNING traps (see Figure 2.1a). A value of C_2 different from unity indicates that the quadrupole potential Φ_2 alone does not describe the shape of the electrodes correctly as for the hyperbolic trap the surface of the electrodes is an equipotential line for the quadrupole potential. The electrostatic potential Φ_2 is created by applying a voltage U_0 between the ring and the two end cap electrodes (see Figure 2.1a and 2.1b). However, the insertion of ions in hyperbolic traps is difficult, because a

hole in the end cap is necessary which then disturbs the electric potential. Therefore cylindrical PENNING traps (see Figure 2.1b) are more common today [BNW10, HKLR+17]. Both trap types usually have additional electrodes between the ring and the end cap or for the seven pole cylindrical trap even beyond the end cap electrodes to adjust the potential to get closer to the ideal case.

An ion with charge q and velocity $\vec{v}$ stored in this electromagnetic field experiences the LORENTZ force

$$\vec{F}_L = q\left(\vec{E} + \vec{v} \times \vec{B}\right) \quad , \tag{2.3}$$

where the electric field $\vec{E}$ can be derived from the potential Φ_2 defined in Equation (2.1) by

$$\vec{E} = -\vec{\nabla}\Phi_2 \quad . \tag{2.4}$$

Using NEWTONS second law on Equation (2.3) leads to the equation of motion

$$\begin{pmatrix} \ddot{x}' \\ \ddot{y}' \\ \ddot{z}' \end{pmatrix} = \frac{qB_0}{m}\begin{pmatrix} \dot{y}' \\ -\dot{x}' \\ 0 \end{pmatrix} + \frac{qU_0C_2}{2md^2}\begin{pmatrix} x' \\ y' \\ -2z' \end{pmatrix} \quad , \tag{2.5}$$

where m is the ion's mass. Primed variables are used to describe the ion position. The variables are primed to distinguish them from the general coordinates (e.g. of the potential). Solving this differential equation leads to three independent eigenmotions with the eigenfrequencies:

$$\nu_z = \frac{1}{2\pi}\sqrt{\frac{qU_0C_2}{md^2}} \quad , \tag{2.6}$$

$$\nu_\pm = \frac{1}{2}\left[\nu_c \pm \sqrt{\nu_c^2 - 2\nu_z^2}\right] \quad , \tag{2.7}$$

where ν_z is the axial-, ν_- the magnetron and ν_+ the modified cyclotron frequency. The so-called free-space cyclotron frequency is defined as

$$\nu_c = \frac{1}{2\pi}\frac{q}{m}B_0 \quad . \tag{2.8}$$

The resulting three-dimensional motion of the charged particle is displayed in black in Figure 2.2. There, implicitly, the corresponding amplitudes $\hat{z}$ and $\hat{\rho}_\pm$ of the oscillations are introduced. In a PENNING-trap only $\nu_\pm$ and ν_z are directly measurable, but of physical interest is usually the free-space cyclotron frequency, which can be obtained from the eigenfrequencies through

$$\nu_c^2 = \nu_z^2 + \nu_+^2 + \nu_-^2 \quad , \tag{2.9}$$

which is in the literature referred to the invariance theorem [BG86]. The hierarchy of the frequencies is $\nu_- \ll \nu_z \ll \nu_+$. Typcially, the frequencies range from a few kHz for ν_- up to a few tens of MHz for ν_+. This makes it necessary to measure the high frequencies particularly precise, as their uncertainty contributes most to that of the free cyclotron frequency.

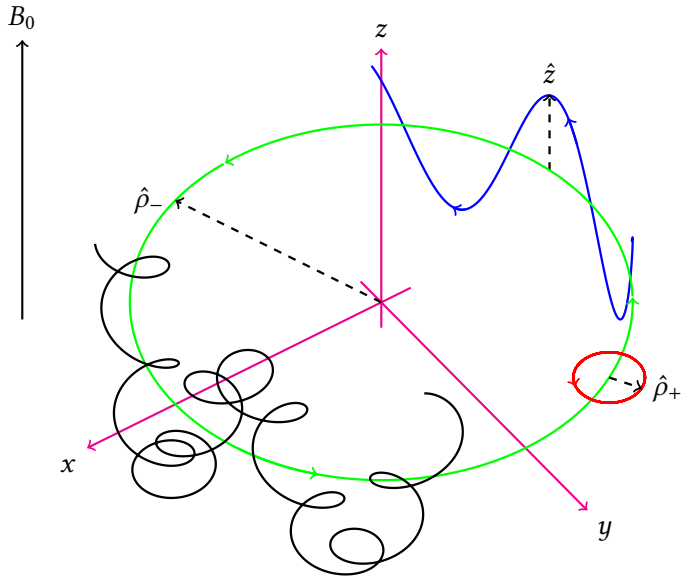

Figure 2.2.: Motion of a charged particle in a PENNING trap. The green circle indicates the magnetron-, the blue circle the axial- and the red circle the modified cyclotron-motion. The thick black line shows the combined motion of all three independent eigen motions. The dashed black arrows define the amplitudes.

2.2. Real PENNING trap

The ideal model of the PENNING trap contains some assumptions, which cannot be fulfilled in reality. For example, the electrodes cannot be infinitely long, the shape deviates from the ideal case due to manufacturing tolerances and in hyperbolic traps a hole in the end cap is necessary to inject ions or for a field emission point to create the ions in the trap [SEH+14]. All these deviations from the ideal case do normally not break the cylindrical symmetry and so the deviations can be quantified by the following expansion [KEH+14b]:

$$\Phi(r,\theta) = \frac{U_0}{2} \sum_{i=2,4,6,\dots}^{\infty} C_i \frac{r_i P_i\left(\cos(\theta)\right)}{d^i} \quad . \tag{2.10}$$

Here, spherical coordinates $r = \sqrt{x^2 + y^2 + z^2}$ and $\theta = \arccos\left(\frac{z}{r}\right)$ are used and $P_i\left(\cos(\theta)\right)$ are the LEGENDRE polynomials. The terms with azimuth angle $\phi = \arctan\left(\frac{y}{x}\right)$ vanish due to the rotational symmetry. Only even terms are listed, as odd terms are strongly suppressed by the mirror symmetry in axial direction. The variable C_i gives the strength of i-th higher order potential component. Only taking $i = 2$ into account, this expression reduces to the ideal case shown in Equation (2.1). All terms for i larger than two are deviations from the ideal case and lead to frequency shifts. Therefore, it is necessary to determine the deviations from the ideal case and to calculate the frequency shifts in order to correct for them. How this is done for higher order field deviations and other shifts as e.g. a tilt of the trap or an ellipticity can be found in e.g. these references [KEH+14a, KEH+14b].

2.2.1. Image charge shift

This section introduces the image charge shift, which is unavoidable by the concept of the ion frequency detection in the trap. The description is in large parts already presented in the article M. Schuh *et al.* [SHE+18], in which the main results from this thesis have been published. The oscillating trapped ion induces image charges on the surrounding trap electrodes. While these induced image charges are essential for the detection of the ion's oscillation frequencies [WD75, Gab84, WVST06], they cause a systematic shift to the ion's frequencies by generating an undesired electrostatic field $\vec{E}_{\text{image}}$, which acts back on the ion and slightly shifts the ion's eigenfrequencies (see Figure 2.3). $\vec{E}_{\text{image}}$ can be approximated by

$$\vec{E}_{\text{image}}(x', y', z') = n\left(\mathcal{E}_x x'\vec{e}_x + \mathcal{E}_y y'\vec{e}_y + \mathcal{E}_z z'\vec{e}_z\right) \quad , \tag{2.11}$$

where the parameters $\mathcal{E}_i$ are the so called electrostatic linear field gradients (LFG) and n is the charge state of the ion. Higher-order terms are present in reality as well, but they are only relevant when the amplitude of the motion becomes comparable to the characteristic trap parameters z_0 and ρ_0 which is usually not the case, as the ion is cooled to the smallest amplitudes [SWSB11]. The term in parentheses represents the LFG induced by one positive elementary charge. Due to the cylindrical symmetry of the PENNING trap electrodes, the LFG of the ICS should be the same in x- and y-direction:

$$\mathcal{E}_\rho \equiv \mathcal{E}_x = \mathcal{E}_y \quad . \tag{2.12}$$

In the following a derivation of the frequency shift due to the ICS is presented. This is only a summary and the full derivation can be found in the Reference [Ket15].

The force $\vec{F} = q\vec{E}_{\text{image}}$ caused by the image charges of the ion leads to an additional term in the radial equation of motion. It is assumed that the image charges cause a perturbation $\epsilon_\rho = n\frac{e\mathcal{E}_\rho}{4\pi^2 m\nu_z^2}$ to the ion motion. This changes the normal radial equation of motion (see Equation (2.5)) to

$$\begin{pmatrix}\ddot{x}'\\ \ddot{y}'\end{pmatrix} = 2\pi\nu_c\begin{pmatrix}\dot{y}'\\ -\dot{x}'\end{pmatrix} + 2\pi^2\nu_z^2\begin{pmatrix}x'\\ y'\end{pmatrix} \quad . \tag{2.13}$$

The radial frequency shifts under the assumption $\nu_- \ll \nu_+$ are

$$\Delta\nu_\pm = \mp n\frac{\mathcal{E}_\rho}{2\pi B_0} \quad . \tag{2.14}$$

It becomes evident from this equation, that the radial sideband frequency $\nu_c = \nu_+ + \nu_-$ is immune to the ICS. The axial shift can be calculated as:

$$\Delta\nu_z = -n^2\frac{q}{m}\frac{\mathcal{E}_z}{8\pi^2\nu_z} \quad . \tag{2.15}$$

The shift of the free-space cyclotron frequency, obtained by using the invariance theorem (see

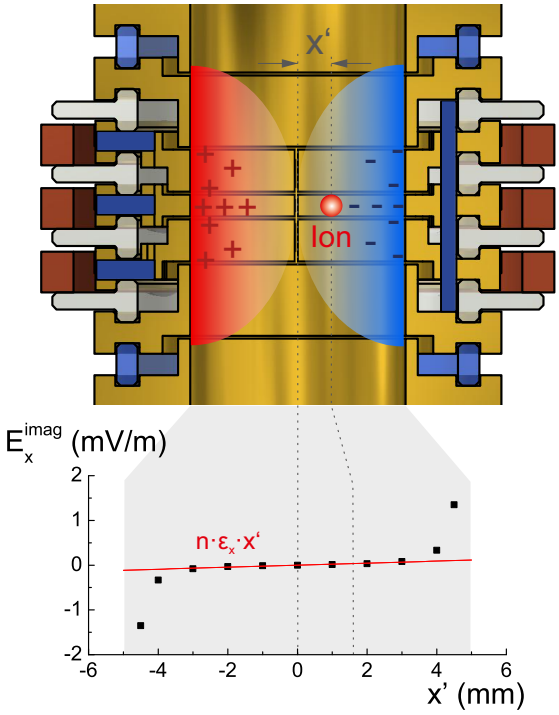

Figure 2.3.: Illustration of the image charge shift (ICS): In the upper part the cylindrical PENNING trap of the LIONTRAP (see Section 6.2.2) experiment is shown with a single positively charged ion shifted in x-direction to position x'. On the surface of the cylindrical electrodes the relative change of the induced image charges is shown, which results from the displacement of the ion from the center position. Less induced image charges result in a relative positive change and is sketched in red and more image charges are sketched in blue. In the lower part the x-component of the simulated electric field at the ion's position is shown, which is generated by the induced image charges when the ion is placed at position x'. Error bars are smaller than the point size. The red line indicates the linear approximation of the induced electric field: $\mathcal{E}_{\text{image},x}(x') = \mathcal{E}_x x'$, where $\mathcal{E}_x$ is the linear field gradient in x direction. Figure taken from [SHE+18].

Equation (2.9)), is then[1]

$$\Delta\nu_c \approx n\frac{2\mathcal{E}_\rho + \mathcal{E}_z}{4\pi B_0} \quad . \tag{2.16}$$

The unperturbed free-space cyclotron frequency ν_c can be obtained from the measurement frequency $\tilde{\nu}_c$ by

$$\nu_c = \tilde{\nu}_c + \Delta\nu_c \quad . \tag{2.17}$$

Focusing on cylindrical PENNING traps (see Figure 2.1b), for a first order calculation of the ICS the electrode surfaces can be approximated as an infinitely long cylinder with radius ρ_0. In this case, an analytical solution of the ICS exists [HBD+03]:

$$\nu_\pm = \mp\frac{q^2}{16\pi^3\epsilon_0 m\rho_0^3\nu_c} \quad , \tag{2.18}$$

where ϵ_0 is the vacuum permittivity. Consequently, the relative shift of the free-space cyclotron frequency

$$\Delta\nu_c/\nu_c \approx m/(4\pi\epsilon_0 B_0^2\rho_0^3) \tag{2.19}$$

shows, that the ICS is most relevant for measurements of heavy ions. Furthermore, it illustrates the strong impact of the trap size: $\Delta\nu_c \propto 1/\rho_0^3$.
For realistic hyperbolic and cylindrical PENNING-trap geometries $\mathcal{E}_\rho$ and $\mathcal{E}_z$ cannot be determined analytically. Therefore, they are determined with the help of COMSOL MULTIPHYSICS™ by using the finite element method (see Section 3.1.1).

2.3. PAUL trap

A PAUL trap is a device that combines static and high-frequency alternating electric fields to confine and manipulate ions. In the following a basic introduction to PAUL traps is given. This section is deliberately kept short, because for this work it is only important to know that PAUL traps can store ions and eject them quickly. A more detailed introduction to PAUL traps including their common use as mass spectrometer can be found here: [vBP61, MD86, BT64, ALB92, BGM+98, BGM+00]. First the linear PAUL trap (Section 2.3.1) is introduced, which confines ions only in two spatial directions. The linear trap can be used to store ions by adding end cap electrodes. This device is called three-dimensional PAUL trap (see Section 2.3.2). In the same section the buffer gas cooling is introduced which allows for slowing down ions with a wide range of kinetic energy and mass.

[1] Note the change in sign convention here. While the shifts in the previous two Equations (2.14) and (2.15) need to be added to the frequencies of the ideal trap - that is, without image charges - in order to yield the actual frequencies in the presence of image charges, the shift in the following Equation (2.16) needs to be added to the measured frequency in order to obtain the free-space cyclotron frequency in the absence of image charges.

2.3.1. Linear Paul trap

The storage of a charged particle in a purely electrostatic potential is impossible [Ear42]. But instead of using a magnetic field as in the Penning trap, it is also possible to combine a static and a high frequency alternating electric field. In an ideal Paul trap, these fields are applied to four infinitely long hyperbolic rods (see Figure 2.4). Opposite electrodes have the same phase and neighboring electrodes are 180° phase shifted in the oscillating potential. This results in the following ideal undisturbed quadrupole potential:

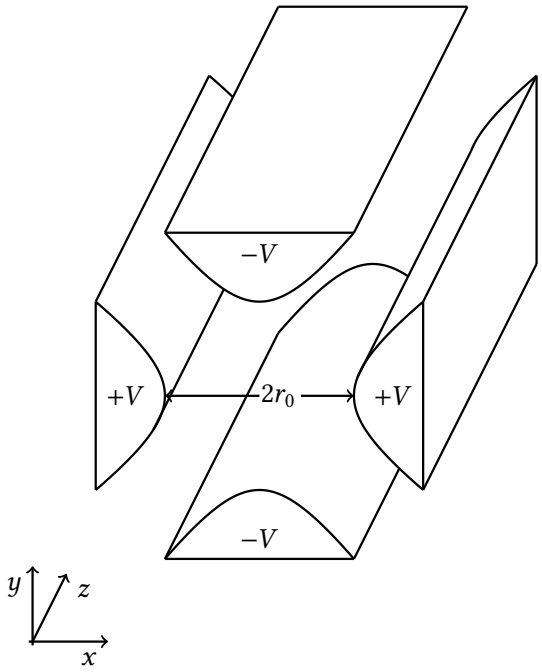

Figure 2.4.: Arrangement of the hyperbolic electrodes of the infinitely long ideal Paul trap extending in z-direction. The ions can pass this trap in z-direction. The trap electrodes have a distance of $2r_0$ from each other. In addition, the electrodes are marked with the oscillating voltage component at a certain time (see Equation (2.20)). Figure modified from [PRvZ58].

$$\Phi(x, y, t) = (U + V \cdot \cos(\Omega t)) \frac{x^2 - y^2}{r_0^2} \quad , \tag{2.20}$$

where U is the constant, $V \cdot \cos(\Omega t)$ the alternating voltage and Ω the oscillation frequency. The electrodes are separated by $2r_0$ from each other. Taking again the negative gradient of Φ and inserting the resulting electric field into the equation of the Lorentz force (see Equation (2.3))

leads, in absence of a magnetic field, to the following equation of motion:

$$\begin{pmatrix} \ddot{x}' \\ \ddot{y}' \\ \ddot{z}' \end{pmatrix} = \frac{2q}{mr_0^2}(U + V \cdot \cos(\Omega t)) \begin{pmatrix} -x' \\ \dot{y}' \\ 0 \end{pmatrix} \quad . \tag{2.21}$$

It should be noted, that the motion in z-direction is not confined. In order to solve these differential equations, the following transformation parameters are introduced:

$$a_x = -a_y = \frac{8qU}{mr_0^2\Omega^2} \quad , \quad q_x = -q_y = \frac{4qV}{mr_0^2\Omega^2} \quad , \quad \Omega t = 2\zeta \quad . \tag{2.22}$$

Inserting these parameters Equation (2.21) yields two Mathieu differential equations [PRvZ58]:

$$\frac{\mathrm{d}^2x'}{\mathrm{d}\zeta^2} + (a_x + 2q_x \cdot \cos(2\zeta)) \cdot x = 0 \quad , \tag{2.23}$$

$$\frac{\mathrm{d}^2y'}{\mathrm{d}\zeta^2} - \left(a_y + 2q_y \cdot \cos(2\zeta)\right) \cdot y = 0 \quad . \tag{2.24}$$

This differential equation can be reduced to its normal form because both movements follow the same equation :

$$\frac{\mathrm{d}^2u}{\mathrm{d}\zeta^2} + (a_u - 2q_u \cdot \cos(2\zeta)) \cdot u = 0 \quad \text{for} \quad u = x, y \quad . \tag{2.25}$$

The exact solution of this equation can be represented as the sum of two independent linear combinations in FOURIE form [MH66]. The solution can generally be divided into two types:

1. Stable motion: The ion oscillates with a limited amplitude in the x- and y- direction and can cross the PAUL trap in the z-direction without hitting the electrodes.

2. Unstable motion: The motion amplitude in the x- or y-direction increases exponentially, so that the ion is lost in the collision with the electrodes.

Whether the solution is stable or unstable depends on the parameters U, V, Ω, m and q in Equation (2.22). This can best be represented in a stability diagram (see Figure 2.5). If the parameters a and q are in the gray area, the movement in the PAUL trap is stable.

2.3.2. 3-dimensional PAUL trap

The three-dimensional PAUL trap can be realized either by segmenting the electrodes, as it is done in Figure 2.6, or adding additional electrodes to the linear PAUL trap. In the ideal case, the radial and axial movements can be considered independent of each other. Thus, the equation of motion in z-direction looks similar to that in a cylindrical PENNING trap, because also only the static electric field is necessary for the restriction in that direction [Gho95]. The restriction is achieved with the PAUL trap by applying an additional voltage U_{end} (see Figure 2.6) to the end segments.

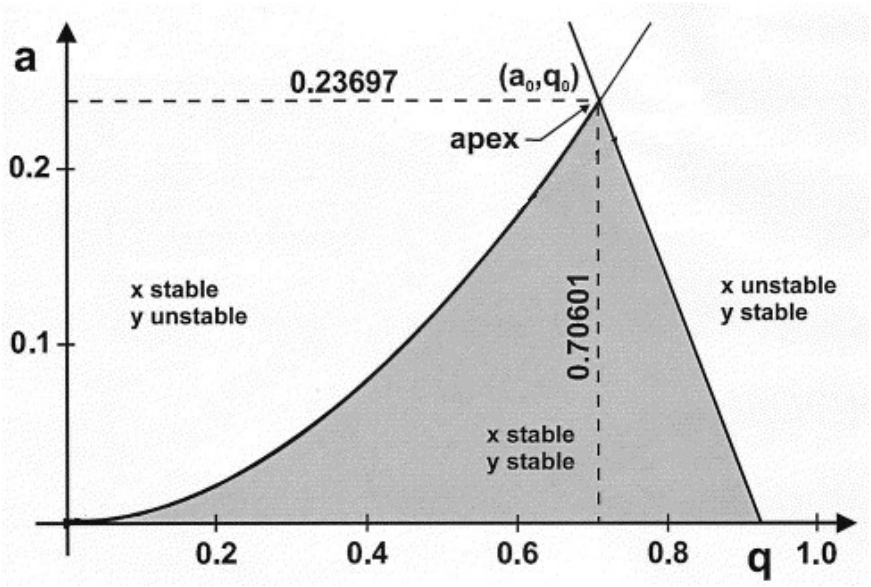

Figure 2.5.: Stability diagram for a linear Paul trap. Only (a, q)-parameters in the gray shaded areas lead to a stable ion motion, i.e. limited oscillating amplitudes in the x- and y-direction. Figure modified from [BGM+98].

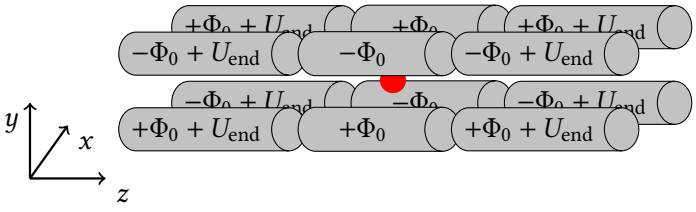

Figure 2.6.: 3-dimensional Paul trap with four segmented cylindrical rods. The same voltage settings as in Equation (2.20) and Figure 2.4 are applied to all twelve electrodes. In addition, the outer eight electrodes have an additional voltage U_{end} to confine the ion indicated in red in z-direction.

In addition, most real three-dimensional traps are build by round instead of hyperbolic rods, as round rods allow easier access to the inside of the trap. These deviations from the ideal hyperbolic trap add additional complexity in the mathematical description of the potential [vBP61]. The resulting equations of motion are well described in Reference [BGM+98]. At this point it is only relevant that the motion of the ions in the real cylindrical and segmented Paul trap cannot be described analytically. Therefore, a simulation is necessary, when the motion of an ion inside of a three-dimensional cylindrical Paul trap has to be calculated.

Buffer gas cooling

Paul traps can be used, among others, for the selection, guiding and storage of short-lived ions. The latter are often produced by shooting high energy beams onto targets (see Section 4.1). Since their lifetime is short, they need to be accelerated strongly to reach the experiments quickly, before they decay. Due to this production process, they have a kinetic energy of up to several 10 eV [NHJ+01]. In order to cool the ions and send them to other experiments, an efficient cooling mechanism independent of charge and mass of the ion of interest is essential. The idea of buffer gas cooling was already proposed by Major and Dehmelt in 1968 [MD68]. The first direct suggestions for Paul traps was made by Douglas and French [DF92, Dou98]. Since then, the idea has been successfully realized in many installations worldwide [NHJ+01, KKMV01, JLMP03, Her03, BSB+12].

When buffer gas cooling is applied, the Paul trap is usually filled with an atmosphere of 10^{-4} to 1 mbar of helium [LBM92, NHJ+01, Her03]. The nuclides release their energy via inelastic scattering to the cooling gas. The transfer efficiency of ions through a Paul trap with buffer gas cooling is about 50 % or better [NHJ+01, Her03]. The ions usually reach equilibrium with the buffer gas latest after a few milliseconds, often after a few microseconds depending on the pressure [LBM92].

As already described above, the ion movement in a Paul trap with cylindrical rods is difficult to describe analytically. If cooling by buffer gas is added to this movement, it becomes impossible. The process of cooling itself can be simulated by scattering hard spheres [MD68]. However, analyzing the behavior of ions in a Paul trap with cooling is important to find improvements for the ion buncher (see Chapter 7). The first simulation of a buffer gas cooled ion movement was done by Lubman *et al.* [LH97] using SIMION in 1997.

2.4. Multi-reflection time-of-flight mass spectrometer

A multi-reflection time-of-flight mass spectrometer (MR-ToF MS) is a device which separates ions with the same kinetic energy by their different velocities. In an MR-ToF MS ions are typically injected as a compact bunch which has been ejected before from a Paul trap. They are reflected back and forth in the MR-ToF device by electrostatic lenses up to a few thousand times [DPB+15]. An example setup of such an MR-ToF MS is shown in Figure 2.7. A time-of-flight mass spectrometer with and without multiple reflection requires that ions with charge q and mass m are all accelerated by the same voltage U from rest. By that it is ensured that they have a very similar kinetic energy. If the spectrometer has a length d and based on the equation for the kinetic energy $E = \frac{1}{2}mv^2$ and $E = qU$, where v is the velocity of the ion, it

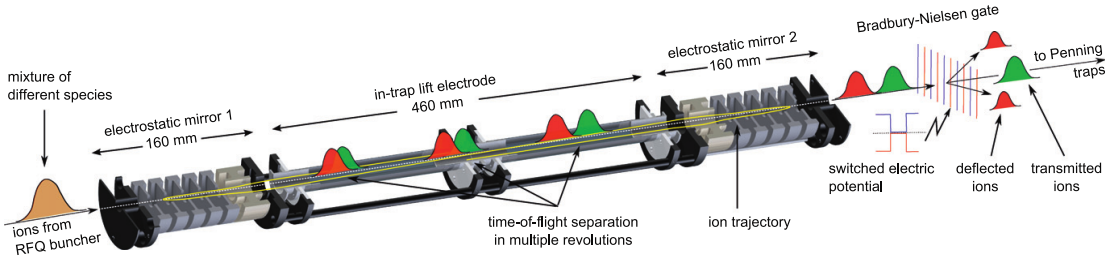

Figure 2.7.: Illustration of an multi-reflection time-of-flight mass spectrometer (MR-ToF MS). On the left a mixture of two ions is injected into the MR-ToF mass separator (sectional view). The bunch shape is indicated by the brown filled Gaussian. It is assumed that the ions have similar kinetic energy. They are separated due to their different mass-to-charge ratios in multiple revolutions inside the MR-ToF MS. After ejection, they pass the Bradbury-Nielsen gate where the contaminant species are deflected. Figure taken from [WBB+12].

needs the time

$$t = \frac{d}{\sqrt{2U}}\sqrt{\frac{m}{q}} \quad , \tag{2.26}$$

to pass it. Assuming that the ions enter the MR-ToF as an ion buch with a full width at half maximum (FWHM) of Δt in the time domain, the mass resolution without reflection can be described by [PDS13]:

$$\frac{m}{\Delta m} = \frac{t}{2\Delta t} \quad . \tag{2.27}$$

This means that the shorter the ion bunch is in the time domain and/or the longer the mass spectrometer, the greater is the mass resolution. The temporal width of the ion bunch is often limited by the trapping and ejection parameters of the Paul trap. Thus, in order to increase the resolution, the length of the MR-ToF device needs to be extended. Since it is difficult to build a vacuum structure of a few kilometer in length, the ions are instead reflected several times (multi reflection) by electrostatic mirrors. After n revolutions the resolution can be described by [WEMS11]:

$$\frac{m}{\Delta m} = \frac{nT}{2\sqrt{\Delta t^2 + n^2 \Delta T^2}} \quad , \tag{2.28}$$

where ΔT is the time spread gained per reflection. Defocusing effects of the electrostatic lenses are neglected here, but they are well described in [WWA+13]. After a certain number of reflections the different species have separated by more than their FWHM, which is needed to distinguish them. Then the potential in the electrostatic lenses which traps the bunches is lowered. The two separate bunches can fly towards the consecutive experiments. A Bradbury-Nielsen gate is used to deflect the unwanted ions and it transmits the desired bunch [BN36]. A typical storage time is in the range of several 10 ms which corresponds to a few 100 or 1000

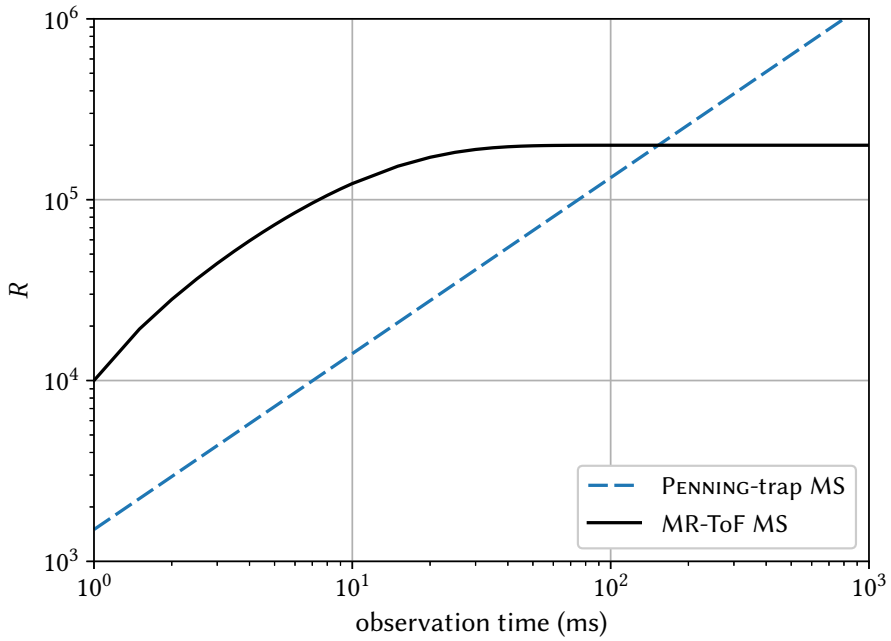

Figure 2.8.: Comparison of the mass resolving power R (see Equation (1.1)) between a Penning-trap mass spectrometer and an MR-ToF MS as a function of time. Figure modified from [WWA+13].

reflections.

The advantage of an MR-ToF MS is shown in Figure 2.8. For a measurement time below 100 ms the MR-ToF MS achieves a better mass-resolving power than a Penning-trap MS [ISW+13, Wol13].

3. Computer numerics and controlling

This thesis is based in all three parts on the intensive use of current computer technology:

1. To simulate a physical effect that limits many PENNING-trap experiments worldwide: the image charge shift. It is simulated with COMSOL MULTIPHYSICS™ (see Section 3.1.2), which uses the finite element method (FEM).

2. To develop an ion buncher for IGISOL based on SIMION (see Section 3.1.3), which also uses the FEM to simulate the electric field inside of the buncher. The ion trajectory is calculated based on the electric field using the 4th order Runge-Kutta method.

3. To build a control system for THE-TRAP based on PYTHON (see Section 3.2).

A basic knowledge of the FEM is therefore essential to understand this work. Thus, a brief introduction to this topic is given in the following section (see Section 3.1). In addition, the programs based on FEM (COMSOL MULTIPHYSICS™ and SIMION, see Section 3.1.2 respectively 3.1.3) are briefly presented. The last section (see Section 3.2) explains what kind of programming language PYTHON is and why it is well suited for the use in the control system of THE-TRAP.

3.1. Solving PDE with FEM

In experimental physics, questions frequently arise where the underlying partial differential equations (PDE) are known, but the complex geometries and associated boundary conditions make finding an analytical solution impossible. In this case an approximate solution has to be found and for finding this solution the finite element method (FEM) is often used. This section gives an introduction to FEM, which is strongly inspired by [Zoh17]. As FEM consists of several steps, an overview is given in Figure 3.1. The individual steps of this figure are explained in the following sections.

3.1.1. Mathematical basics for FEM

The easiest way to explain the FEM is to use an example. GAUSS's law is taken as an example, since MAXWELL equations are of central relevance in this work.

MAXWELL equation

GAUSS's law says [Max65]:

$$\vec{\nabla}\vec{D} = \rho \quad , \tag{3.1}$$

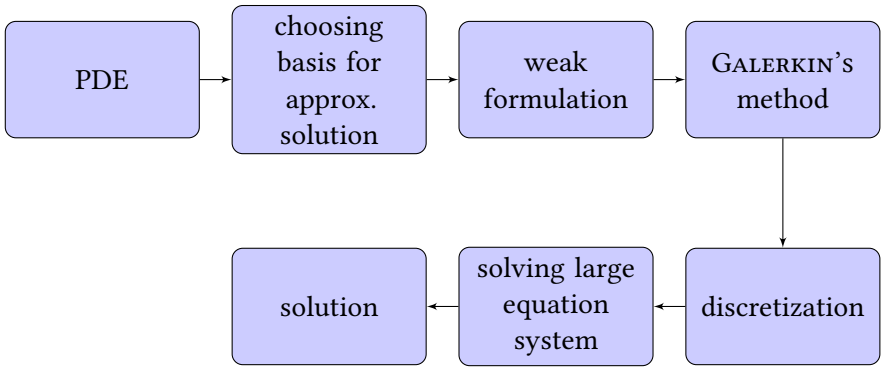

Figure 3.1.: Flow chart of the FEM. First the partial differential equation or equations including the boundary conditions must be known. Then an arbitrary base for the approximate solution of the partial differential equation (PDE) is chosen. The same base in a different linear combination is used for the weak formulation, which reduces the problem of discontinuities in the scope of the PDE. These non-continuous places can occur, for example, due to sudden changes in the material type. Galerkin's method is used to determine the best approximate solution. The next step is to define the base which is still arbitrary up to this point. To make an ideal choice is an optimization problem, which is not discussed here. The choice of the base is at the same time the discretization or also called "mesh", since the base is defined only section by section. Based on the now known base, the system of equations can be created. Solving it results in the approximate solution of the PDE.

where $\vec{D}$ is the electric displacement field and ρ is the distribution of the electric charge. The electric displacement field is linked to the electric field $\vec{E}$ as follows

$$\vec{D} = \epsilon \vec{E} \quad , \tag{3.2}$$

where ϵ is the permittivity. As the electric field $\vec{E}$ can be derived from the potential ϕ by

$$\vec{E} = -\vec{\nabla}\phi \quad , \tag{3.3}$$

the following partial differential equation is obtained

$$\vec{\nabla}\left(\epsilon\vec{\nabla}\phi\right) + \rho = 0 \quad , \tag{3.4}$$

neglecting polarization. To simplify and clarify the formulas, the following description is limited to the one dimensional case:

$$\underbrace{\frac{\mathrm{d}}{\mathrm{d}x}\left(\epsilon\frac{\mathrm{d}\phi}{\mathrm{d}x}\right)}_{\sigma(\phi)} + \rho = 0 \quad . \tag{3.5}$$

In the following, the way to find ϕ for given ϵ, ρ and boundary conditions of ϕ is explained. For a lower chance of confusion by multiple derivations, $\sigma(\phi)$ is introduced implicitly. It will be resolved later.

Basis of approximation solution

First the basis of the approximate solution has to be set. At the moment it is not necessary to put too much thought into how exactly the approximation should look like. But it is reasonable to assume a set of basis functions γ_i. They get multiplied with prefactors a_i, which have to be determined later by solving a linear equation system (see Figure 3.1). Since one out of the set of basis functions will not give a good approximation or the basis has to be very complex a linear combination of the basis functions is chosen. This gives the N-th order approximation ϕ^N

$$\phi^N(x) = \sum_{i=1}^{N} a_i \gamma_i(x) \quad , \tag{3.6}$$

of the searched potential ϕ.

Weak formulation

Physical questions sometime show discontinuities in the form of internal boundary conditions, e.g. ϵ will jump when the medium changes. To reduce this problem, a so-called "weak form" is introduced now.
For this weak form a new function v is defined. Be v an arbitrary and smooth scalar function. It is reasonable that v can be expressed in the same base as the arbitrary solution (see Equation (3.6)), but in a different linear combination:

$$v^N(x) = \sum_{i=1}^{N} b_i \gamma_i(x) \quad . \tag{3.7}$$

The arbitrary function which has the only requirement to be continuous and differentiable should have the same order as the approximate solution defined in Equation (3.6). Multiplying v with Equation (3.5) and taking the integral form results in:

$$\int_\Omega \left(\frac{\mathrm{d}\sigma}{\mathrm{d}x} - \rho \right) v \mathrm{d}x = 0 \quad , \tag{3.8}$$

where Ω is the volume or, in the one dimensional case, the length of the body. Applying the product rule on $\int(\sigma v)\mathrm{d}x$ leads to

$$\int_\Omega \frac{\mathrm{d}v}{\mathrm{d}x} \sigma \mathrm{d}x = \int_\Omega \rho v \mathrm{d}x + \sigma v|_{\partial\Omega} \quad . \tag{3.9}$$

Plugging the definition of σ (see Equation (3.5)) back in results in

$$\int_\Omega \frac{\mathrm{d}v}{\mathrm{d}x}\epsilon\frac{\mathrm{d}\phi}{\mathrm{d}x}\mathrm{d}x = \int_\Omega \rho v \mathrm{d}x + \sigma v|_{\partial\Omega} \quad . \tag{3.10}$$

In Equation (3.5), ϵ must be differentiable, here this condition is weakened. This makes it clear why it is called weak formulation.

Galerkin's method

Next, a concept is needed to determine the prefactors a_i from Equation (3.6). For this, it is necessary to calculate the quality of the selected approximation. This section will show that maximizing the quality is equivalent to solving a system of equations.
The quality of the introduced approximation ϕ^N can be estimated by plugin it into Equation (3.5). In the ideal case it returns zero. The size of the deviation from zero is the so-called residual r^N:

$$r^N(x) = \frac{\mathrm{d}}{\mathrm{d}x}\sigma\left(\phi^N(x)\right) + \rho \quad , \tag{3.11}$$

which is a function of $\phi^N(x)$. Since it is the goal to optimize the averaged quality of the approximation on the domain Ω, the distance must be positive semidefinite. The following choice is possible for the quality Q on the full domain

$$Q \equiv \int_\Omega \left(r^N(x)\right)^2 \mathrm{d}x \quad . \tag{3.12}$$

As mentioned above, the quality has to be maximized, which means in this case, that Q has to be minimized. The approximation fits best, if the residuals are minimal. In the widespread „Least Square“ method, the global residual minimum would now be determined by setting the individual derivatives to a_i zero.
Here another method is taken. Only the residuals at certain positions ($i = 1, 2, \ldots N$) are forced to be zero

$$r^N(x_i) = 0 \quad . \tag{3.13}$$

This can be rewritten as an integral using the Dirac functional:

$$\int_\Omega r^N(x)\delta(x - x_i)\mathrm{d}x = 0 \quad . \tag{3.14}$$

This approach is called "Method of weighted residuals". It generally has the form:

$$\int_\Omega r^N(x)\omega(x)\mathrm{d}x = 0 \quad , \tag{3.15}$$

where $\omega(x)$ is called "weight". This approach was also used to determine the image charge effect according to Porto's method (see Section 6.4).
Galerkin takes this method and expands it. Assuming the correct solution ϕ, the approximate

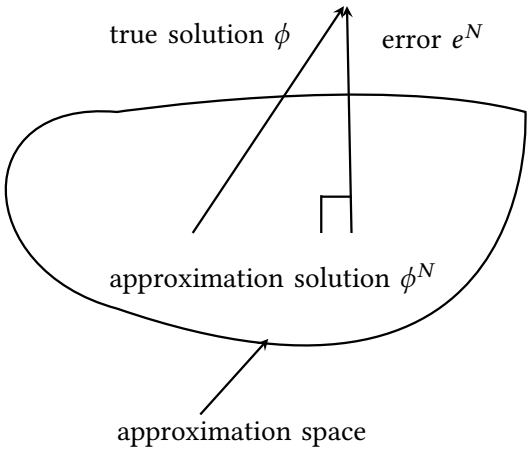

Figure 3.2.: Galerkin's method showing the relation between the true solution ϕ, the approximate solution ϕ^N and the error e^N. Figure modified from [Zoh17].

solution ϕ^N and the deviation e^N between the two, can be represented by the following relation:

$$\phi - \phi^N = e^N \quad . \tag{3.16}$$

It is helpful to imagine this connection as vectors (see Figure 3.2). The error e^N is smallest if it is orthogonal to ϕ^N. The problem is that the e^N is not known. However, the residuals are known (see Equation (3.11)) and here comes Galerkin's idea. It forces ϕ^N to be orthogonal to r^N. This is the same as taking ϕ^N for the weights $\omega(x)$ in Equation (3.15):

$$\int_\Omega r^N(x)\phi^N(x)\mathrm{d}x = \int_\Omega r^N(x) \sum_{i=1}^{N} a_i\gamma_i \mathrm{d}x = 0 \quad . \tag{3.17}$$

But this only leads to a single equation, which is not enough to determine all a_i. A system of equations with N equations for N unknown results if every single basic function of the approximation must result in the integral zero:

$$\int_\Omega r^N(x)a_i\gamma_i(x)\mathrm{d}x = 0 \Rightarrow \int_\Omega r^N(x)\gamma_i(x)\mathrm{d}x = 0 \quad . \tag{3.18}$$

That conclusion is not obvious but it would be beyond the scope of this thesis to reproduce this mathematically here. Instead, the interested reader is referred to further literature on this subject [Zoh17].

FEM Approximation

Plugin in Equations (3.6), (3.7) and the definition of σ (see Equation (3.5)) into Equation (3.10) results in the following system of equations:

$$\begin{aligned} &\int_\Omega \frac{\mathrm{d}}{\mathrm{d}x}\left(\sum_{i=1}^{N} b_i\gamma_i(x)\right)\epsilon\frac{\mathrm{d}}{\mathrm{d}x}\left(\sum_{j=1}^{N} a_j\gamma_j(x)\right)\mathrm{d}x \\ &= \int_\Omega \left(\sum_{i=1}^{N} b_i\gamma_i(x)\right)\rho\mathrm{d}x + \left(\left(\sum_{i=1}^{N} b_i\gamma_i(x)\right)\epsilon\frac{\mathrm{d}}{\mathrm{d}x}\sum_{i=1}^{N} a_i\gamma_i(x)\right)\Bigg|_{\partial\Omega} \quad . \end{aligned} \tag{3.19}$$

This must be valid for all b_i, because the function v (see Equation (3.7)) is an arbitrary function and so it can be rewritten as:

$$0 = \sum_{i=1}^{N} b_i\left(\int_\Omega \frac{\mathrm{d}\gamma_i}{\mathrm{d}x}\epsilon\frac{\mathrm{d}}{\mathrm{d}x}\sum_{j=1}^{N} a_j\gamma_j\mathrm{d}x - \int_\Omega \gamma_i\rho\mathrm{d}x - \gamma_i\epsilon\frac{\mathrm{d}}{\mathrm{d}x}\sum_{i=1}^{N} a_i\gamma_i\Bigg|_{\partial\Omega}\right) \tag{3.20}$$

$$\Rightarrow 0 = \sum_{i=1}^{N} b_i\left(\sum_{j=1}^{N} K_{ij}a_j - R_i\right) \tag{3.21}$$

$$\Rightarrow \vec{R} = \mathbf{K}\vec{a} \quad , \tag{3.22}$$

where the matrix $\mathbf{K}$ consists of the elements

$$K_{ij} \equiv \int_\Omega \frac{\mathrm{d}\gamma_i}{\mathrm{d}x}\epsilon\frac{\mathrm{d}\gamma_j}{\mathrm{d}x}\mathrm{d}x \quad , \tag{3.23}$$

$\vec{a}$ of the unkown variables and the vector $\vec{R}$ consists of

$$R_i \equiv \int_\Omega \gamma_i\rho\mathrm{d}x + \gamma_i\left.\frac{\mathrm{d}}{\mathrm{d}x}\sum_{i=1}^{N} a_i\gamma_i\right|_{\partial\Omega} \tag{3.24}$$

The system of equations (3.22) has to be solved in order to get the approximate solution of the PDE (see Equation (3.5)).

Discretization

The only variables not yet defined in Equation (3.22) are the basis functions γ_i. It has to be considered that the basis functions have to be calculated quickly on a computer, because they occur in large numbers.
Polynomials can be calculated on the computer with little effort and are therefore preferred. It has turned out that the attempt to introduce basis functions that describe the whole problem at once is difficult or impossible. Hence, the piecewise definition of basic functions is advantageous.

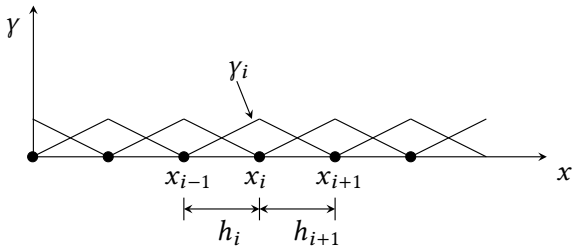

Figure 3.3.: Example of a one dimensional uniform mesh. The basis function γ_i is a linear polynomial and defined only over one interval. Otherwise it is at zero. Figure modified from [Zoh17].

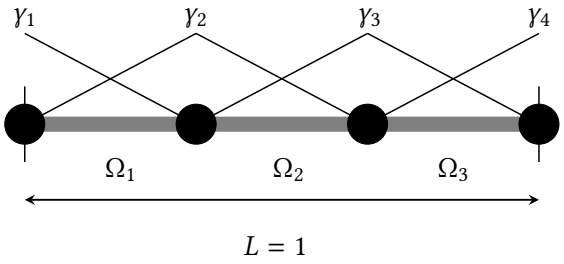

Figure 3.4.: Mesh of a finite problem with length $L = 1$, three domains, four mesh nodes and correspondingly four basis functions γ_i. Figure modified from [Zoh17].

A good candidate for a simple base is:

$$\gamma(x)_i = \frac{x - x_{i-1}}{h_i} \quad \text{for } x_{i-1} \leq x \leq x_i \quad , \tag{3.25}$$

where $h_i = x_i - x_{i-1}$ and

$$\gamma(x)_i = 1 - \frac{x - x_i}{h_{i+1}} \quad \text{for } x_i \leq x \leq x_{i+1} \quad , \tag{3.26}$$

and $\gamma(x)_i = 0$ otherwise. This definition leads to the uniform mesh displayed in Figure 3.3. This mesh offers the opportunity to evaluate Equation (3.22) piecewise over each subdomain $\Omega_e = x_i - x_{i+1}$ individually. In the end, this is merged by $K_{ij} = \sum_e K_{ij}^e$ and $R_i = \sum_e R_i^e$.

Application

Now that the basis has been introduced, an explicit example follows. The differential equation (see Equation (3.5)) remains. The area is not longer infinitely large, but should consist only of four mesh elements and has a total length of $L = 1$ (see Figure 3.4). The weak form following Equation (3.10) is now

$$\int_0^{L=1} \frac{\mathrm{d}v}{\mathrm{d}x} \epsilon(x) \frac{\mathrm{d}u}{\mathrm{d}x} \mathrm{d}x = \int_0^{L=1} \rho(x) v \mathrm{d}x + \left(\epsilon(x) \frac{\mathrm{d}u}{\mathrm{d}x} v \right) \Big|_0^{L=1} \quad . \tag{3.27}$$

Computing the first elements of Equation (3.22) over Ω_1 results in

$$\underbrace{\left(\int_0^{1/3} \frac{\mathrm{d}\gamma_1}{\mathrm{d}x}\epsilon(x)\frac{\mathrm{d}\gamma_1}{\mathrm{d}x}\mathrm{d}x\right)}_{K_{11}^{e=1}} a_1 + \underbrace{\left(\int_0^{1/3} \frac{\mathrm{d}\gamma_1}{\mathrm{d}x}\epsilon(x)\frac{\mathrm{d}\gamma_2}{\mathrm{d}x}\mathrm{d}x\right)}_{K_{12}^{e=1}} a_2 + \underbrace{\left(\int_0^{1/3} \frac{\mathrm{d}\gamma_1}{\mathrm{d}x}\epsilon(x)\frac{\mathrm{d}\gamma_3}{\mathrm{d}x}\mathrm{d}x\right)}_{K_{13}^{e=1}=0} a_3 + 0\,\text{etc} \tag{3.28}$$

and

$$R_1^{e=1} = \int_0^{1/3} \gamma_1(x)\rho(x)\mathrm{d}x + \epsilon(x)\gamma_1(x)\frac{\mathrm{d}}{\mathrm{d}x}\sum_{i=1}^{4} a_i\gamma_i(x)\Big|_{x=0} \quad . \tag{3.29}$$

In total the system of equations looks like:

$$\begin{bmatrix} K_{11}^{e=1} & K_{12}^{e=1} & 0 & 0 \\ K_{21}^{e=1} & K_{22}^{e=1} + K_{11}^{e=2} & K_{12}^{e=2} & 0 \\ 0 & K_{21}^{e=2} & K_{22}^{e=2} + K_{11}^{e=3} & K_{12}^{e=3} \\ 0 & 0 & K_{21}^{e=3} & K_{22}^{e=3} \end{bmatrix} \begin{bmatrix} a_1 \\ a_2 \\ a_3 \\ a_4 \end{bmatrix} = \begin{bmatrix} R_1^{e=1} \\ R_2^{e=1} + R_1^{e=1} \\ R_2^{e=2} + R_1^{e=3} \\ R_2^{e=3} \end{bmatrix} \tag{3.30}$$

One might wonder why e.g. the element $K_{22}^{e=3}$ is not named $K_{44}^{e=3}$ as its position would indicate. It is common to save memory in a computer to drop indices which have zero elements and the elements $K_{11}^{e=3}$ and $K_{22}^{e=3}$ are zero. The next coming indices are then reduced by two. By this renaming the memory allocation of this matrix drops from $N \times N$ to $3 \times N$. For large models or models, which require a fine mesh N can easily reach 100.000 and more. It would be impossible to store this matrix without memory saving.
To solve this system of equations, only the charge distribution $\rho(x)$, the permitivity $\epsilon(x)$ and the boundary conditions of ϕ are necessary. As a result, the potential can be calculated at any point.
The example shown here is very simple. In actual applications, higher order polynomials are used and the mesh density is much higher. In three dimensional applications the size of the matrix K_{ij} increases with the third power of the number of mesh elements. To solve this system of equations, special iterative solvers are used that allow parallelization. Nevertheless, the basic concept, as presented here, remains the same in the used tools COMSOL MULTIPHYSICS™ and SIMION.

3.1.2. COMSOL MULTIPHYSICS™

COMSOL MULTIPHYSICS™ is a commercial software that solves PDEs using FEM. Through a graphical user interface (GUI), which is shown in Figure 3.5, the PDEs and boundary conditions, such as the geometry of the problem, material properties or voltages and charge distribution can be defined. COMSOL MULTIPHYSICS™ offers software modules with pre-defined differential

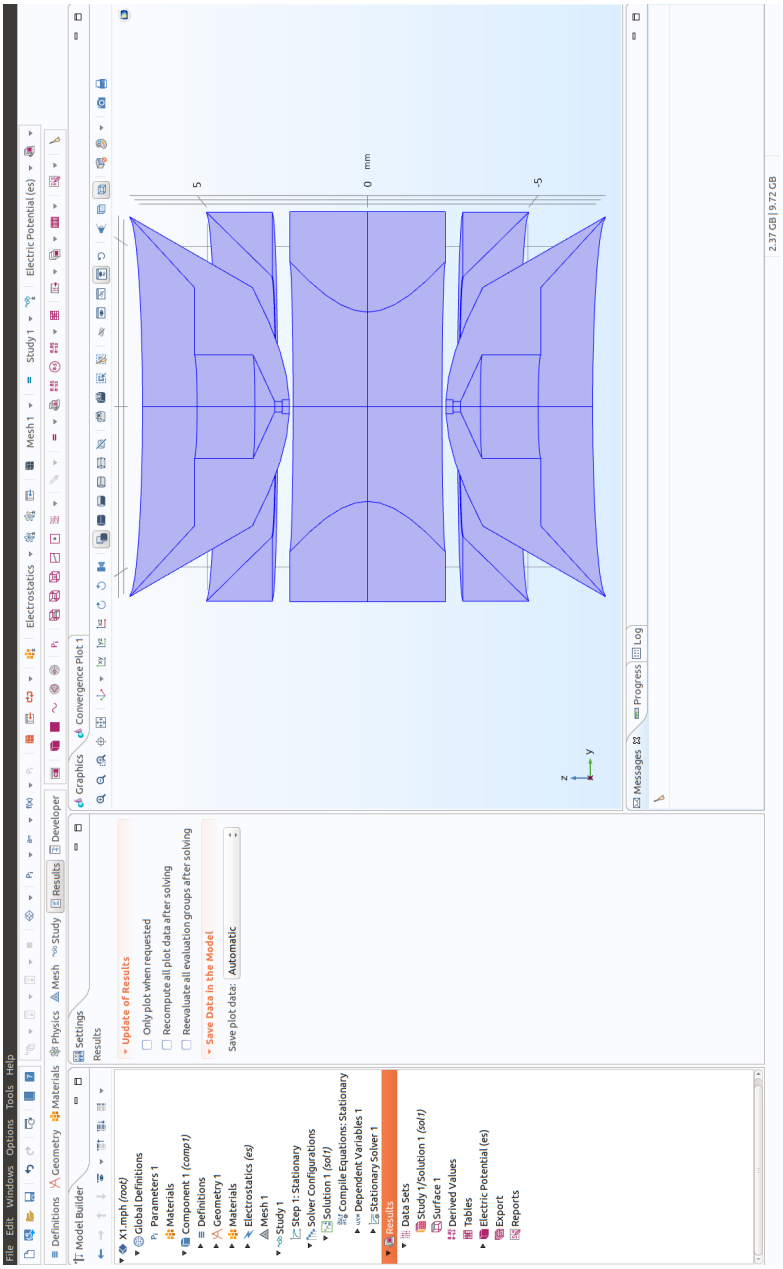

Figure 3.5.: COMSOL MULTIPHYSICS™ GUI. It is divided into three columns. The left column shows the simulation tree, including the PDEs, the material properties, the geometry, the mesh, the solver and the solution. The content of the middle column depends on the element chosen in the left column. It gives further details to the currently chosen option. The right column shows the current geometry and gives the ability to select certain domains to apply properties to it. Here, a view of the simplified model of the THE-TRAP precision trap is shown.

equations, where it is directly obvious which physical boundary conditions have to be set. One of them is the AC/DC module, which covers the field of electrostatics and is the only one used for this work. The geometries of the simulated problems are directly modeled within the software, even though they can be imported as CAD files, too. In the next step the physics parameters as, e.g., charge, which is assumed to be point-like and position of the charge in the trap and the DIRICHLET boundary conditions of perfectly conducting electrode surfaces are set. Based on these pieces of information, the underlying differential equation, in this case the static MAXWELL equations, are solved as described above. For this, the geometry has to be meshed. A finer mesh improves the approximation and will give more reliable results before the numerical precision starts to be the limiting factor. A minimum and maximum size of the mesh element can be set for the algorithm which creates the mesh. COMSOL MULTIPHYSICS™ offers as mesh type tetrahedron, hexahedron, triangular prism, and pyramid. In all simulations the default option of the tetrahedron is chosen. The algorithm chooses automatically the minimum size for areas with detailed structures, as for example the edges of the electrodes. It increases continuously the size of the mesh towards areas with less structure. In the software package several mathematical tools are directly offered as surface integrals on the meshed geometry, so the result of the simulated surface charge densities can be treated directly further.
In addition, the simulation can be setup and executed completely without using the GUI. All simulations can first be created as a java file, which is then translated by a build-in compiler. The software is currently being further developed and a new version is released about every six months. More information can be found on the COMSOL MULTIPHYSICS™ homepage *www.comsol.com*.

3.1.3. SIMION

SIMION is also a tool that solves PDEs with the help of FEM. To be more precise, it solves the PDEs by the finite difference method (FDM) but both methods are equivalent for regular grids and SIMION uses only cubes of constant size for the complete geometry in the simulation to create the mesh. The size of the cubes is set manually by the user.
On the homepage *www.simion.com* [Sim] it states about its purpose:
„*SIMION Version 8.1 is a software package primarily used to calculate electric fields and the trajectories of charged particles in those fields when given a configuration of electrodes with voltages and particle initial conditions, including optional RF (quasistatic), magnetic field, and collisional effects. In this, SIMION provides extensive supporting functionality in geometry definition, user programming, data recording, and visualization.* “
The simulation of the electric field is carried out by using the already introduced FEM. The calculation of the trajectory of the ions is based on the simulated electric field and the use of the 4th order Runge-Kutta algorithm. The GUI is shown in Figure 3.6. The geometry has to be loaded ready meshed. In the GUI, the mentioned voltages and radio frequencies (RF) can be adjusted and the mass as well as the location and velocity distribution of the ions can be set. At the time of use, the last update was five years ago. Nevertheless, SIMION is widely used in the mass spectrometry community. Therefore, many research groups already have experience with this program, which makes it much easier to get started. In addition, other physical effects, such as cooling by residual gas (see Section 2.3.2), can be loaded by external modules written by the user. Also, SIMION offers the possibility to start simulations without the GUI.

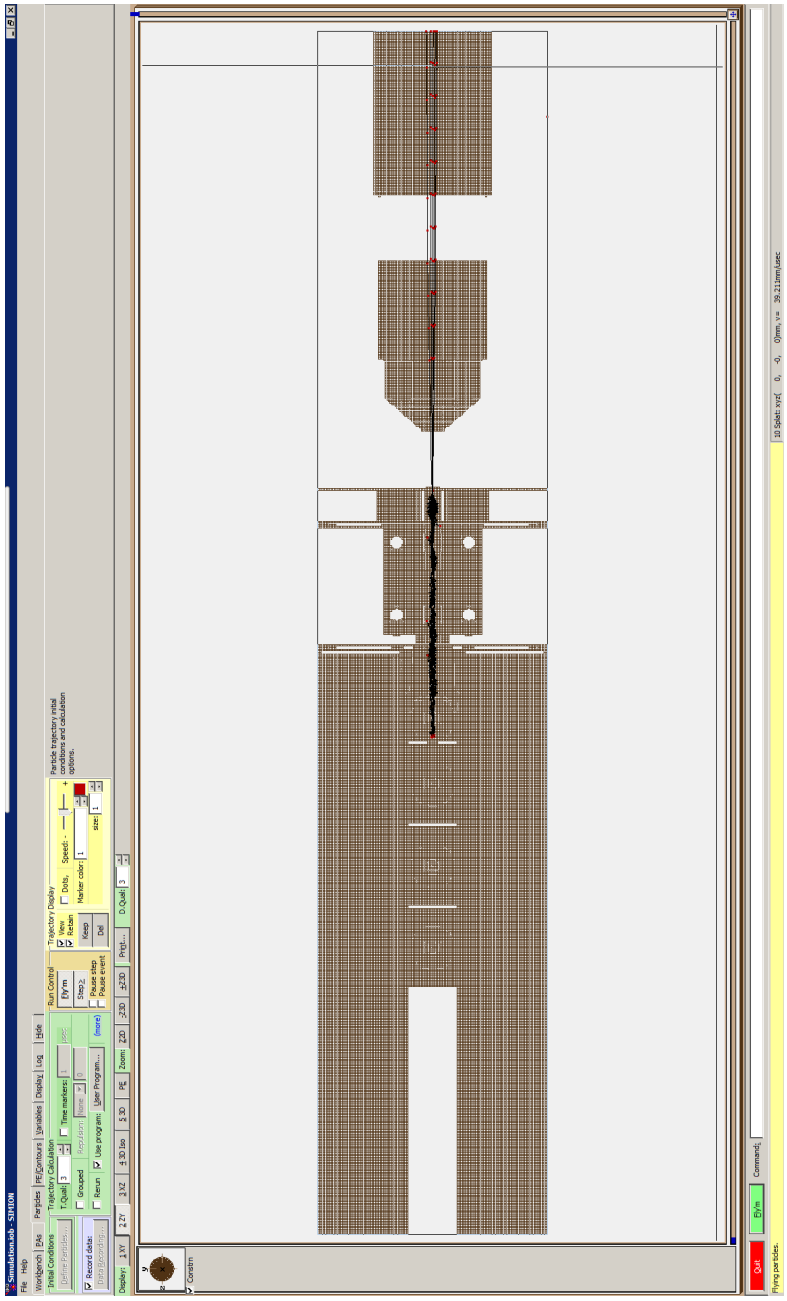

Figure 3.6.: SIMION GUI. It offers possibilities to set the start parameters, as voltages, RF and ion start properties. Here, singly charged ions with a nuclear mass of 100 are created in the last section of the RFQ cooler of the IGISOL experiment (see Section 4.1). After switching a few voltages with appropriate timing the ions get shot out of the ion buncher and fly to the right. The ions paths are indicated by black lines. Further information about these simulations is given in Section 7.1.

3.2. Python

For giving an introduction to Python it is worth it to have a look at its homepage *www.python.org*. There it is stated:
„*Python is an interpreted, object-oriented, high-level programming language with dynamic semantics. Its high-level built in data structures, combined with dynamic typing and dynamic binding, make it very attractive for Rapid Application Development, as well as for use as a scripting or glue language to connect existing components together. Python's simple, easy to learn syntax emphasizes readability and therefore reduces the cost of program maintenance. Python supports modules and packages, which encourages program modularity and code reuse.* "
All these properties are exploited in the control system for THe-Trap (see Chapter 5). In addition, Python benefits from a large number of extensions and external programs, as, for example, the development of the GUI for THe-Trap took place with the help of the Qt Designer [QtD]. For controlling external devices drivers are often needed. Many drivers are already provided by the companies in Python or existing drivers in the programming language C [C-S] can be directly addressed via interfaces in Python. Also, the number of well working development environments (e.g. PyCharm [PyC] or Microsoft Visual Studio [Vis]) has made the work much easier.

4. Experimental setups

The work for this thesis was carried out at two experimental facilities. One part was done during two one-month research stays in the accelerator laboratory of the University of Jyväskylä, Finland with the IGISOL setup (see Section 4.1). This facility is dedicated for studying the properties of short-lived nuclides. In the following there is a short introduction of the whole setup and a detailed description of the radio-frequency quadrupole (RFQ) ion beam cooler / buncher for ion beam manipulation (see Section 4.1.1), which was modified in the terms of this thesis.

The rest, the majority of the time, was spent at the tritium-helium-3 Penning-trap experiment (THe-Trap) at the Max-Planck-Institute for Nuclear Physics in Heidelberg, Germany (see Section 4.2). It is dedicated to determine the Q-value of tritium (see Equation (1.3)) to a relative precision of 10^{-6} in order to provide to the KATRIN experiment (see Section 1.2.3) a reference Q-value for the determination of the anti-electron neutrino mass [SEH+14]. A description of the experimental setup and the measurement procedure for determining the free cyclotron frequency is provided (see Sections 4.2.1 and 4.2.2, respectively). In the third part of this section the old control system is described (see Section 4.2.3), which at the same time provides the motivation for the newly developed control system (see Chapter 5).

4.1. IGISOL

The Ion Guide Isotope Separator On-Line (IGISOL) facility is located at the Accelerator Laboratory of the Jyväskylä University, Finland. The facility is in operation since three decades [MDA14] and has reached its current expansion stage in 2013 [MEG+13], when the move to the new experimental hall was finished. The facility layout is shown in Figure 4.1. It provides radioactive ion beams, which are produced by nuclear reactions to different experimental installations. IGISOL is served by two cyclotrons: MCC30, which can provide up to 30 MeV proton and 18 MeV deuteron beams and K130, which can provide higher energy protons and deuterons in addition to beams of heavier elements. The beam from the cyclotrons is impinged on a thin target, for example ^{238}U, to induce fission reaction (see (3) in Figure 4.1). The short-lived nuclides produced in the reaction are stopped in helium gas. The products exit the gas cell through a small nozzle to the high vacuum section, where they are accelerated with 30 kV voltage. Most of the ions are singly charged, a small fraction also survives as doubly charged and are transported further. The first mass selection is carried out with a 55° dipole magnet (see (7) in Figure 4.1). The mass selection of the reaction products is essential because many unwanted nuclides are generated during target bombardment. The resolving power of the dipole magnet is sufficient to select the mass number of the ions of interest. These ions are transported further to the radio-frequency quadrupole (RFQ) cooler / buncher (see (9) in Figure 4.1), which is placed at a 30 keV high-voltage platform to electrostatically slow down the ions. In the RFQ cooler /

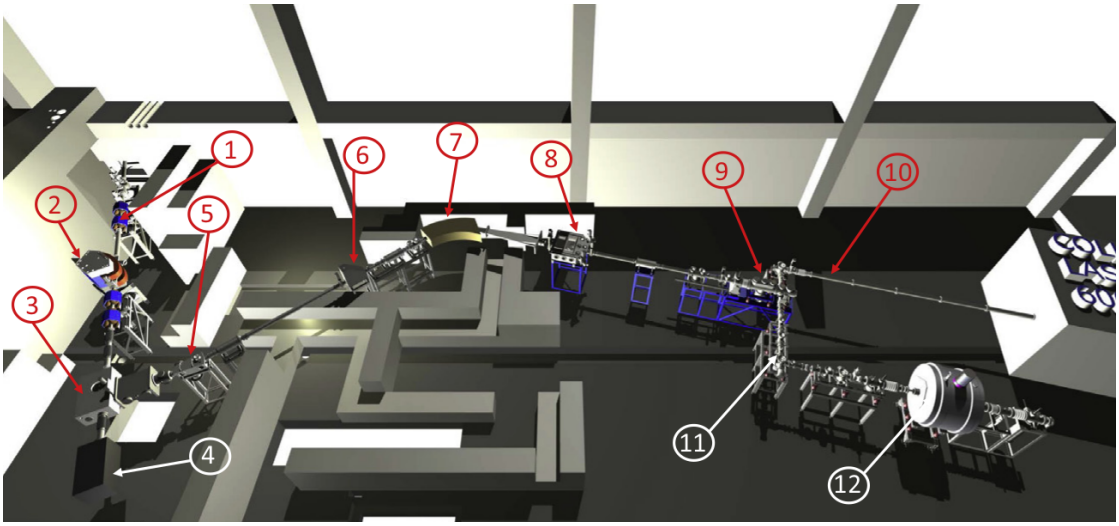

Figure 4.1.: Illustration of the IGISOL hall and the experimental area beam lines. The numbering is as follows: (1) K130 cyclotron beam line, (2) MCC30 cyclotron beam line, (3) IGISOL target chamber, (4) beam dump, (5) electrostatic 15° bender, (6) electrostatic 90° bender for joining beams from upstair's offline ion source, (7) 55° dipole magnet for mass number selection, (8) electrostatic switchyard, (9) RFQ cooler/buncher, (10) collinear laser spectroscopy line, (11) RFQ-to-Penning-traps low energy transfer beam line, (12) Penning traps. Figure taken from [KEG+13]

.

buncher the ions are cooled in a helium buffer-gas environment and possibly bunched in order to send them either to the collinear laser spectroscopy line or to the Jyfltrap Penning-trap setup (see (10) and (11) in Figure 4.1, respectively).
The Jyfltrap Penning and the collinear laser spectroscopy line have been and are still used to investigate the properties of short lived atoms. During the years of operation, atomic masses of more than 200 short lived nuclei [NCE+19, MDA14, JEH+06, HDJ+04] and many of their atomic transition lines [CTB+02, CBB+09, VVB+18] were measured. The Penning trap also provides isobarically and isomerically clean samples of ions to decay spectroscopy experiments [KEE+07, PEE+12, GAT+16, KPU+18]. For the direct mass measurement and the high-resolution beam-purification bunched beams are required. The collinear laser spectroscopy experiment at IGISOL also needs a cooled and bunched beam for background suppression. Since the RFQ cooler / buncher is modified in the scope of this thesis, it will be presented in detail in its original version.

4.1.1. RFQ cooler / buncher

The construction of the RFQ cooler / buncher was completed around the year 2000 [NHJ+01]. After its commissioning, no significant changes were made until the modification of the bunching section during the work of this thesis. The RFQ cooler / buncher is marked in Figure 4.1 with (9).

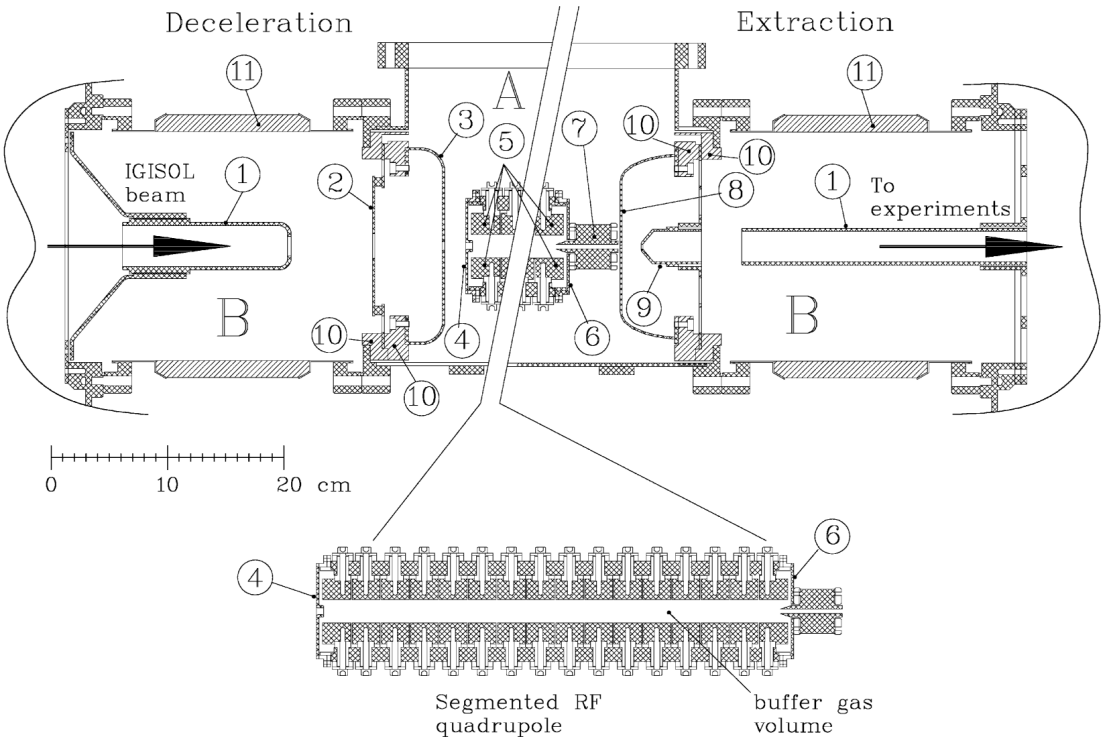

Figure 4.2.: Geometry and electrode configuration of the IGISOL RFQ cooler / buncher before the modifications. (1): ground electrode, (2): first deceleration electrode, (3): second deceleration electrode, (4): third deceleration electrode, (5): RF quadrupole rod segments, (6): end plate, (7): miniature quadrupole rods, (8): extraction plate, (9): extraction electrode, (10): isolator ring, (11): high-voltage isolator. Figure taken from [NHJ+01]. See text for more details.

Its internal structure is shown in Figure 4.2 (from [NHJ+01]). The ions enter the RFQ from the left as indicated by the arrow. They are slowed down to a few ten eV by the high-voltage platform floated to 30 keV until they reach the electrode marked with (4) (see Figure 4.2). Then the ions enter the main quadrupole structure, which works by the principles of a Paul trap (see Section 2.3). The quadrupole structure extends between electrodes marked (4) and (6). The quadrupole electrodes are cylindrical and each divided into 16 segments with 0.5 mm gaps between the segments. The total length of the quadrupole structure is 40 cm and the diameter of the electrodes is 2.3 cm. The distance between opposite electrodes is $2r_0 = 2$ cm (see Figure 2.4).

Typical voltage amplitudes are $V = 150$ V for the main RF quadrupole and $V = 3.4$ V for the miniature quadrupole, both at a frequency of $\Omega = 2\pi \cdot 550$ kHz (see Equation (2.20) for the definition of V and Ω). A small DC gradient is applied to guide the ions towards the exit side of the RFQ. After the main quadrupole structure follows the so-called mini RFQ marked with (7) in Figure 4.2. It has a length of 5 cm, out of which 6 mm extend inside the main quadrupole, and an inner radius of $r_0 = 1.5$ mm. The main quadrupole is enclosed inside a steel cylinder and the ends are closed by the third deceleration electrode ((4) in Figure 4.2) and the end plate

(⑥ in Figure 4.2) to keep the helium gas from escaping freely. The ions are stopped there by the end plate marked by ⑥. If its potential is changed from blocking (+50 V) to passing (-1.5 V), the ions can be extracted towards downstream experiments.

The RFQ cooler / buncher combines the concept of the linear Paul trap with the buffer gas cooling (see Section 2.3.2). Typically, helium is used as buffer gas and the optimal pressure is about 0.1 mbar for the main RFQ. It is tested experimentally that the transmission efficiency of the RFQ does not change significantly if the pressure is doubled or even tripled from this value [NHJ+01]. Helium in other parts of the system originates from the main RFQ through any gaps in the enclosure, mainly towards injection side and through the end plate towards the mini RFQ. The apparatus is pumped continuously and due to the different geometries within the RFQ cooler / buncher different pumping speeds are achieved. Therefore, there are different pressures in different parts of the setup, but the exact pressure distribution is not known, because vacuum sensors are not present in all parts of the RFQ cooler / buncher and flow simulations have not been carried out yet.

Extensive studies have shown that this device has a transmission efficiency of about 60 % [NHJ+01]. The ions can be ejected as a bunch or continuously. The energy spread of the extracted ions is less than 1 eV with a temporal spread of about 11 µs. The energy spread is excellent but the temporal spread is too much for the planned MR-ToF MS (see Section 2.4) as the temporal width is crucial for its mass resolving power. The new buncher should create bunches with a FWHM of about 100 ns. An even shorter width would be preferred but usually comes with the trade-off of a higher energy spread, which also limits the resolving power. Based on experience the energy spread should stay below 40 eV. Chapter 7 describes modifications applied to the mini RFQ in order to produce ion bunches with a FWHM of less than 100 ns and 40 eV.

4.2. THe-Trap

THe-Trap is an abbreviation for tritium-helium-trap. It is a Penning-trap setup dedicated for measuring the β-decay Q-value of tritium (see Equation (1.3)). The aim is to determine the tritium-helium-3 mass ratio with an uncertainty of 10^{-11}, which yields the tritium β-decay Q-value with a relative precision of 10^{-6}. An independent Q-value with this uncertainty can be used by the KATRIN experiment as an independent check for their systematic uncertainties (see Section 1.2.3). THe-Trap was originally built at the University of Washington, USA, from where it was shipped to Heidelberg in 2008. This section first introduces the setup (see Section 4.2.1), including the ion detection system and the feedback system to keep the axial oscillation constant. This is followed by an outline of the measurement procedure (see Section 4.2.2). In the last section, the old computer control system is described to motivate the renewal of this system (see Section 4.2.3). The new control system is then described in Chapter 5.

4.2.1. Setup

In the following the setup of THe-Trap is presented. First the traps itself are described, followed by the ion detection system and the magnet.

Trap geometry

THe-Trap consists of two Penning traps. They can be seen in Figure 4.3. The lower trap, called

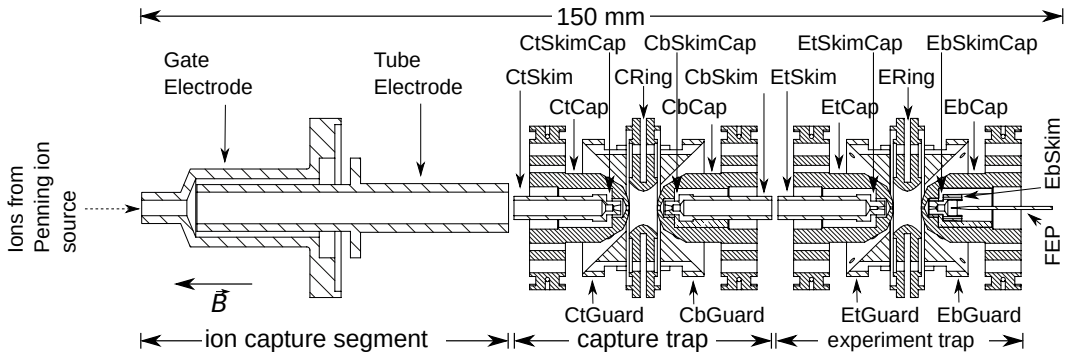

Figure 4.3.: THe-Trap electrode configuration. The location of the traps within the experiment can be seen in Figure 4.4. The abbreviations C and E stand for capture trap and experiment trap, respectively, and t and b for top and bottom. The field emission point is abbreviated by FEP. Figure modified from [Str14].

experimental trap is the main trap where all mass-ratio measurements are performed. The characteristic trap dimensions z_0 and ρ_0 (see Figure 2.1a) are 2.29 mm and 2.77 mm, respectively. The upper trap, called capture trap is intended to store one ion species while the other one is in the experimental trap. The capture trap should also catch ions, which are sent from the external Penning ion source located roughly one meter above (see Figure 4.4). In between there is the ion capture segment, which guides the ions from the Penning ion source to the capture trap. This ion source was characterized and commissioned (see Reference [Sch14]), but the ion transfer between the capture and the experimental trap never worked reliably.
For testing, a field-emission-point (FEP) located in the lower endcap of the experimental trap was used to create ions directly in the trap. The feedthrough flange below the experimental trap allows to send electrical signals into and from the trap. Both is important, e.g. to set the voltages to the electrodes but also to read out the ion signal.

Ion detection and frequency determination

All three eigenfrequencies (see Equations (2.6) and (2.7)) need to be measured to determine the free-space cyclotron frequency through Equation (2.8). To do this, one of the endcap electrodes is connected to a resonator circuit (see Figure 4.5). The axial oscillation of the ion induces an image current to this electrode. The induced oscillating current between the endcaps is only a few fA and not measurable with room temperature electronics. To detect the induced image current, the endcap electrode is connected to an LCR circuit and an amplifier that both are kept at liquid helium temperature (see Figure 4.4 and 4.5). The amplified signal is fed to room temperature electronics, where the oscillation is detected as a few mV signal. This, however, only gives access to the axial frequency. In order to measure the magnetron as well as the reduced cyclotron frequency, additional steps are needed. An overview of the detection setup

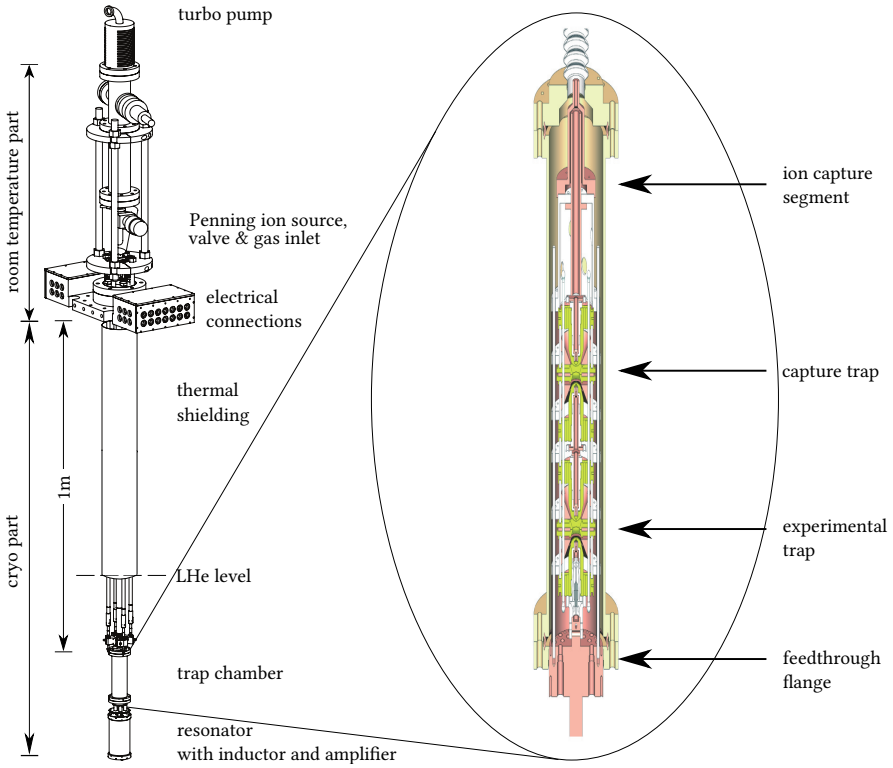

Figure 4.4.: THe-Trap setup [Pin07]. On the left the full setup is shown. It can be separated into two parts. The part which is at room temperature is at the top. It consists of the turbo molecular pump, the external Penning ion source, valves and gas inlet for external gas supply followed by the header for electrical connections. The rest of the setup is inserted through the bore stand off (see Figure 4.9) into the vessel of the magnet. The trap vacuum chamber is then placed at the level of the magnet coils. The content of the trap chamber is enlarged on the right. The ion capture segment to catch ions from the Penning ion source is located on top. Followed by the capture trap and the experiment trap. The feedthrough flange for electrical connections is at the bottom of the trap chamber.

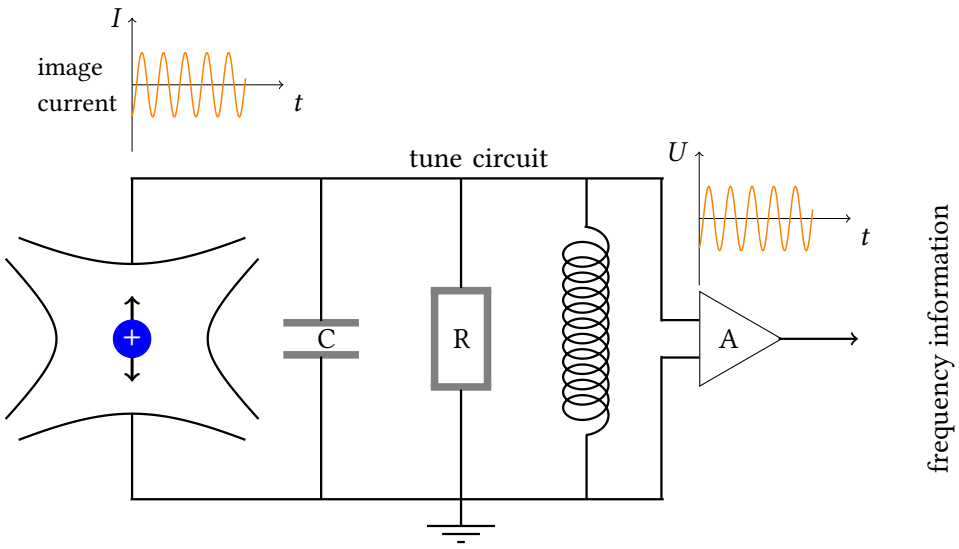

Figure 4.5.: Axial frequency detection scheme at THE-TRAP. The motion of the ion indicated by a blue dot with a plus induces an image current between the endcap electrodes. This image current is detected and converted by an LCR circuit and an amplifier to an oscillating voltage with a few mV amplitude. At THE-TRAP, the resonance frequency for the circuit is chosen to be 4 MHz.

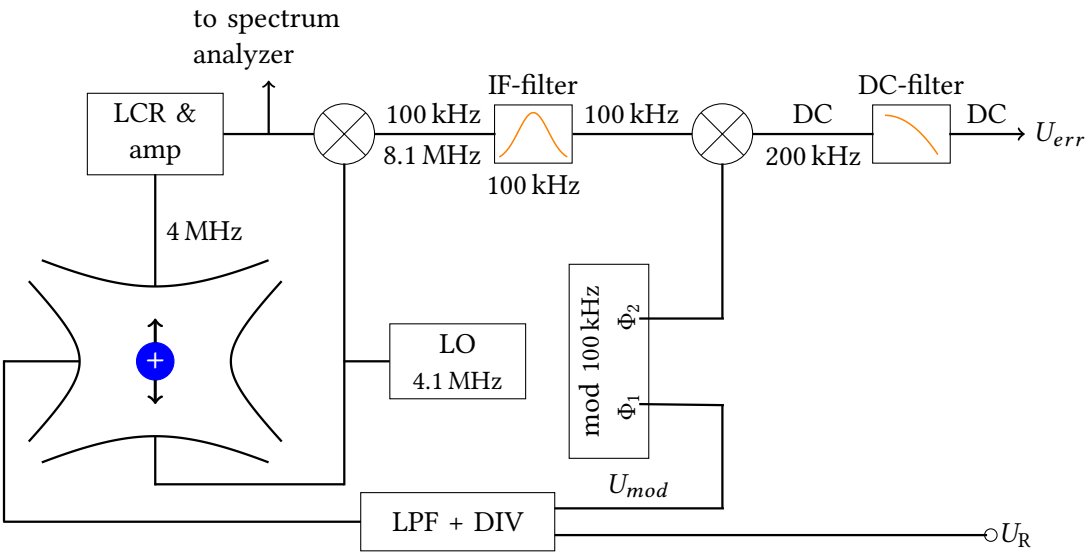

Figure 4.6.: Continuous axial drive at THE-TRAP. The ion is driven via a sideband at 4.1 MHz. The ion frequency is compared with the excitation and any deviation results in a correction signal. The box labeled with LCR & Amp is enlarged in Figure 4.5. More information in the text.

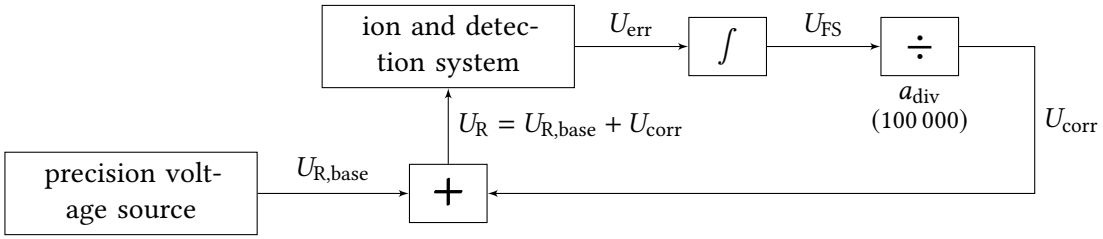

Figure 4.7.: THe-Trap feedback system. It takes the feedback U_{err} generated by the circuit in Figure 4.6 and uses a PID to create a feedback voltage U_{FS}. This feedback voltage is divided down by 100,000 and applied to the ring electrode voltage to keep the ion oscillating at 4 MHz. More information is given in the text.

is shown in Figure 4.6. First of all, the ring electrode voltage U_R is chosen so that the ion's axial frequency is the same 4 MHz as the resonant circuit's resonance frequency. Additionally, the ring electrode voltage is modulated with a 100 kHz RF-voltage. This produces ±100 kHz sidebands in the axial mode, allowing the axial mode to be driven on the 4.1 MHz sideband. This is called "drive". The choice of 4.1 MHz prevents the 4 MHz resonant circuit (see Figure 4.5) from being excited directly. Direct use of 4 MHz drive would mask the ion signal and also, in the worst case, would destroy the cryogenic amplifier circuit.

The amplified ion signal of 4 MHz is finally mixed down to a DC signal. Therefore, first the amplified signal is mixed with a signal originating from a 4.1 MHz frequency generator called the local oscillator (marked LO in Figure 4.6). The mixer produces two signals: One at 8.1 MHz and one at 100 kHz. The 8.1 MHz signal is filtered away with a band-pass filter marked as intermediate filter (IF) in Figure 4.6. The passed 100 kHz signal is mixed with the same frequency but different phase (see Φ_1 and Φ_2 in Figure 4.6) than the ring electrode modulation signal. Again two signals occur, where one is at 200 kHz and the other one is a signal at DC or at least very close to DC with a frequency below 1 Hz. The 200 kHz component is again filtered out. When setting the phase difference of Φ_1 and Φ_2 of the modulation signal to 90°, the resulting signal U_{err} is proportional to the deviation between the excitation and the actual axial frequency, in a small frequency band near the ion's axial frequency (4 MHz). The feedback depends also on the drive strength, ion's mass and the charge state. If the actual axial frequency is lower than the ion's axial frequency, U_{err} is positive and vice versa. A good description of the feedback shape can be found in Reference [Hö16].
The correction signal is integrated, then scaled and finally fed into the feedback system (see Figure 4.7). This feedback system continuously analyzes the correction signal. A PID controller [Ath71] is used to adjust the small correction voltage U_{corr}, which is applied on top of the ring electrode voltage U_{R} so that the axial oscillation frequency stays at 4 MHz. This is called axial frequency lock.

So far only the axial frequency is known (fixed by choice to 4 MHz as described above). To determine the magnetron or cyclotron frequency, radial dipolar excitation is applied while observing the axial frequency. The dipolar excitation is applied by sweeping the frequency slowly (over several seconds or even minutes) over the expected ion's resonance frequency. The frequency sweep is started either below or above the expected resonance frequency. At

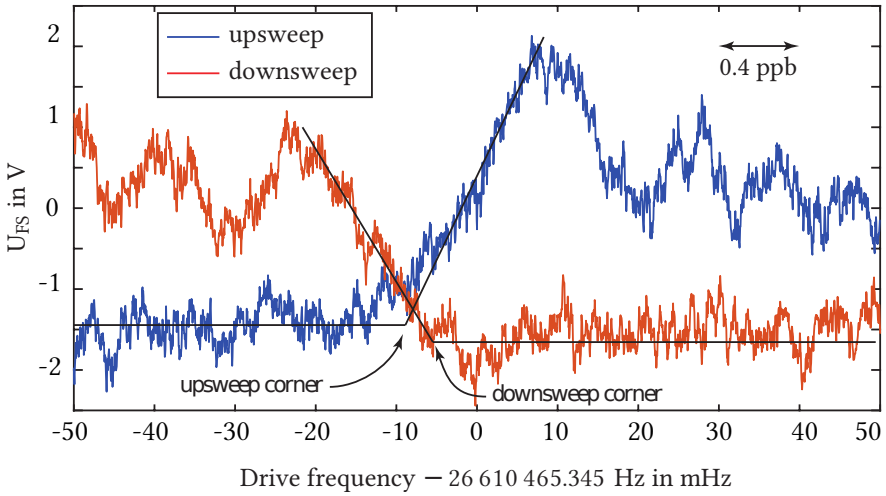

Figure 4.8.: Observation of U_{FS} (see Figure 4.7) while shining in a continuous dipole excitation. For the blue line the excitation is started below the expected resonance frequency and then increased. For the red line it is the opposite. The base line and the slope of both is approximated by a fit, which is indicated as a black line. The crossing of the black lines indicate the resonance frequency. Figure modified from [Hö16].

the same time, the correction signal U_{corr} is monitored for axial frequency changes. When the resonance is hit, the increased amplitude in radial mode also change the axial frequency, due to anharmonicities [KEH+14b]. The feedback system changes the ring electrode voltage in order to keep the ion in lock. A record of U_{corr} during such a sweep is shown in Figure 4.8. The base line and the slope of both scans are fitted. The crossing of the fits is assumed to indicate the resonance frequency. However, it should be noted that there are major concerns that there might be systematic shifts in this measurement procedure, which are not yet known [Hö16].

Magnet and stabilization system

The trap electrodes shown in Figure 4.3 and the tune circuit shown in Figure 4.5 are constituents of the cryo part of the experiment (see Figure 4.4). This means that these parts are operated at a temperature of 4 K. This low temperature has the advantage of noise reduction for the detection system and a cryo pumped vacuum in the trap. The cryo part of the experiment is inserted through the top flange with a diameter of 100 mm into the cold bore of the 5.9 T superconducting magnet (see Figure 4.9), which was built by Nalorac Cryogenic Corporation. As mentioned in Section 1.3.1 the magnetic field stability is crucial to reach a measurement precision of 10^{-11}. Therefore, several measures are taken to reduce the impact of changes in the environment on the magnet. The magnet is located at the 1st floor of the Gentner building at the Max-Planck-Institute for Nuclear Physics in a dedicated temperature-controlled room. The experiment is controlled from a separate room located on top of the magnet room, where almost all electronic devices are located.
The only device which is located in the magnet room is the precision voltage source to reduce

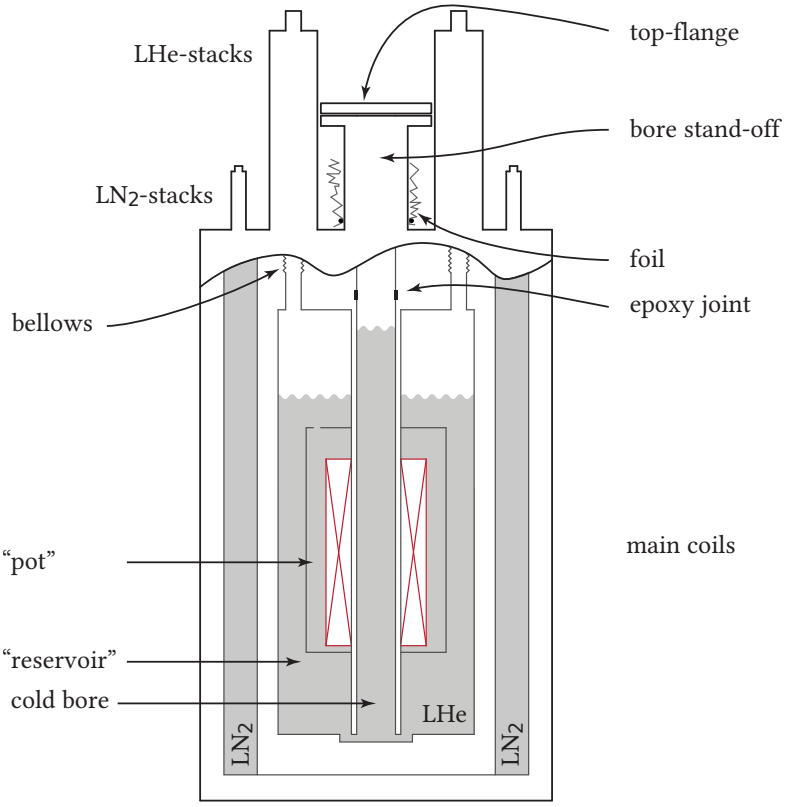

Figure 4.9.: Schematic cross section of the THe-Trap superconducting magnet. It consists of the cylindrical housing, which contains the tank for liquid nitrogen and the tank for liquid helium. On top are the stacks for filling the cryogenic liquids. Between the stacks, the Penning traps are lowered after removing the top flange into the liquid helium reservoir until they hang at the level of the center of the main coils. Figure taken from [Hö16].

its temperature dependent voltage fluctuations, which is a current limitation in high-precision Penning-trap experiments. In addition, the helium gas volume of the magnet is pressure stabilized, as this can have a massive influence on the cyclotron frequency [SEH+14]. Further measures, e.g. the compensation for external magnetic fluctuations, have been taken. The environmental stabilization is described in detail in Reference [Str14].

4.2.2. Typical measurement run

In order to understand the necessity of a new computer control system, a rough sequence of a measurement is outlined below. It is assumed that the Penning trap is placed in the charged magnet and that all cryogenic liquids are filled, so that there is a good vacuum of better than 10^{-12} mbar and that all other devices are connected and work within their specifications. It is also assumed that an ion is already in the trap and in lock. The following steps are necessary to record the data shown in Figure 4.8:

1. Prepare the frequency synthesizer for the sweep by setting the start and stop frequency as well as the amplitude and the sweep time.
2. Start the frequency sweep and the recording of U_{corr} at the same time [1].
3. Wait up to 250 seconds until the sweep has finished.
4. Save the data and store the settings of this run.
5. Switch off the constant axial drive of the ion and the ring modulation.
6. Perform a dipole excitation to couple the cyclotron mode with the axial mode in order to cool the cyclotron mode.
7. Switch on the drive and the ring modulation.
8. Bring the ion back to lock by adjusting the PID regulation (see Figure 4.7). The ion is back in lock, when U_{corr} does not change and is not equal to one of its extreme values.
9. Repeat 1 - 8 with inverted start and stop frequencies.

This process determines the cyclotron frequency of the trapped ion. In addition, the trap must be characterized after every reload of an ion to determine anharmonicities and deviations from the ideal Penning trap. These processes are well described in Reference [Hö16]. They are extensive and time consuming. It is repetitive, but must be well documented, because for the analysis later the exact time, settings and data must be known.

[1] The internal timing of a Microsoft Windows 7 operating system is sufficient for this purpose.

4.2.3. Old control system

The THe-Trap control system, called THe-Controller, is based on the C programming language in the NI LabWindows™/CVI development environment. The main control is the graphical user interface (GUI), from which all functions of the experiment (voltages, attenuators, frequency generators, etc.) can be controlled. The basic functionality of this program is described in the following References [Die11, SEH+14]. As already mentioned above, the measurement processes are complex, time-consuming and repetitive. To transfer this task to a computer the script language called THe-Script was developed [Str14]. This scripting language made the work on the experiment much easier. It makes it possible to program the repetitive pressing of buttons in the GUI and the setting of values as a fixed sequence. However, the functionality was limited as only 23 commands were implemented. This limitation is based on the separate interpreter that had to be written for the script language THe-Script. Mathematical instructions cannot be written directly via "a = 3 + 5", which would assign the variable a the value "3 + 5", but must be described via "Add(a, 3, 5)". Calculating more mathematical complex functions as exponential function, roots or logarithms is not possible unless each of them would be (manually) added as separate commands. The most needed and missed function was to start scripts with several parameters. This was solved by variables, which were stored in the main frame of the control program but leading to further problems if the variable name is used twice or not initialized. After the main developer of the control system left in 2016, it became apparent that the maintenance and expansion of the code is difficult. The code has grown continuously since 2007, without having been cleaned up in the meantime. This made it also difficult to implement new devices which replaced broken ones. Since the script functionality took over the work on the experiment more and more and the programming language Python spread within the group, it was decided to migrate the controller to a Python based version. The new controller is described in the following chapter.

5. Python based control system for THe-Trap

The experiment THe-Trap needs a control system in order to show the current status of the experiment, the status of the tasks that are currently being performed and to control the measurements as discussed in Section 4.2. It was decided to develop a new control system in 2016 based on a proposal in the PhD thesis of Martin Höcker (see Reference [Hö16]), to move from the sweep method (see also Section 4.2) to a pulse-and-phase (PnP) measurement technique [SWSB11]. The main motivation was to improve the experiment's performance and remove systematic uncertainties due to the sweep method. However, this required fundamental changes in the control system. The previous system was designed such that the experiment was controlled by one computer only, because most of the devices were controlled via GPIB and USB and located in the same room as the computer. This control system had the possibility to write measurement scripts in a custom developed language called THe-Script.
In the past, THe-Script was almost used exclusively to perform measurements and the GUI was only used when problems occurred. The script language helped to take over repetitive tasks, but functionality as well as the user-friendliness of the syntax were limited (see Section 4.2.3). The following sections first define the requirements (see Section 5.1.1) for the new control system and then those for the programming language (see Section 5.1.2). Then the selected structure in the control system is explained. Afterwards, in Section 5.3, the GUI is presented and as an example one experimental application is discussed.

5.1. General requirements

This section defines the specifications for the new THe-Trap control system. A distinction is made between the requirements for the programming language and for the control system itself. First, the requirements for the control system are defined, as these also influence the choice of the programming language.

5.1.1. Control system requirements

The new control system has to offer an easy way to write measurement scripts and to change or even create them while it is running. The control system should be as modular as possible. One problem of the old control system was that the same functions were written several times for different devices. In case of errors, troubleshooting was difficult because the entire source code had to be searched for the specific kind of task and had to be fixed in multiple parts in the source code.

A graphical user interface (GUI) is also mandatory. On the one hand it simplifies the manual control of the experiment, which is often used independently of the measurement scripts, on the other hand the GUI should show which script is currently running and which task this script is performing. A GUI helps to find experimental problems, because different parameters such as network analyzer, voltages of the high-voltage supply or voltage of the correction signal (see Figure 4.7) are read out and displayed simultaneously to the currently performed task. This decreases the effort to link problems in the experiment to the executed procedures. Thus, the GUI works as a "State Display" in order to immediately visualize the state of the experiment. The control system should also do the tasks of the documentation by itself as much as possible. This includes saving the current settings and data for each measurement, as well as documenting and reporting problems.

5.1.2. Computer language requirements

The most important criterion for the programming language is that it must be a text-based programming language to keep the readability of the source code in a large project like a control system. The widely used "Laboratory Virtual Instrument Engineering Workbench" (LabVIEW) offers the advantage that almost all hardware suppliers offer drivers for their devices. Also, the quick creation of small applications is easy to perform. However, due to its graphical programming, LabVIEW quickly becomes confusing when many devices have to be controlled and arranged in one program.

The next important criterion is that the language should allow for object-oriented programming. This functionality is essential because only classes have the concept of inheritance which significantly simplifies the required modular structure (see previous section). The concept of decorators is also wanted. Decorators in programming make it possible to nest one function into another by simple syntax. For example, before executing some functions A, B and C, it should always be checked whether a certain file exists on the computer. This can be done by an "if" request in the code of A, B and C itself or by a decorator at the declaration of the functions, which calls this "if" request. The advantage of the decorator is that if the request has to be modified, only the source code of the decorator has to be changed and not the code in every function that has to perform the request. This allows to implement the Single Responsibility Concept [Mar02], which states that only one function is responsible for one kind of task, even though it is needed many times in the source code.

To prevent the GUI from freezing during a measurement, the measurement must run in a different thread than the GUI. Therefore, a rudimentary possibility of parallelization is necessary. These criteria reduce the number of available languages to three popular ones:

1. PHP
2. Python
3. C/C++/C#

In addition, a language with a wide distribution in the scientific community and a large community among developers is preferred. This makes it easier to search for literature and look up frequently asked questions in online forums. Since Python is becoming more and more

popular and especially the module PyVisa offers the possibility to integrate LabVIEW drivers directly, the choice was made in favor of Python.
The THe-Trap setup is compact and spreads over two rooms only (see Section 4.2.1), where most of the devices to be controlled are in one room. Therefore, only one computer is needed and instead of using EPICS[1], which is becoming more and more popular at the moment, an own control system concept is designed.

5.2. Concept

During the development, attention was paid to a strict hierarchy as well as to the single-responsibility concept. The structure of the control system is shown schematically in Figure 5.1. The goal of the design of the control system is to build a GUI which shows the current status of the experiment at a glance. This is marked with "State Display" (see Figure 5.1). Scripts will perform most of the measurement sequences automatically, as the tasks at the experiment are very repetitive. Therefore, the scripts are closer to the measurements than the GUI (see arrow in the Figure), but the scripts always report the current performed task to the GUI. Below the GUI there has to be a structure, which handles all tasks, the GUI and the scripts initiate. Despite running the control system in general, this structure should take care that all problems, which may occur during execution, are logged and reported, but do not lead to a crash of the control system. The way to achieve all this is described in detail in the following.

5.2.1. Internal process handling

The *Basic classes* are made for processes within the code and do not communicate to the outside of the computer. The class `GuiInteraction` controls via a signal and slot concept[2] that the GUI can be accessed from parallel running threads. It is possible to access directly the memory space of GUI elements from another thread without the signal and slot concept. If this is not controlled by a signal and slot concept, multiple accesses can occur simultaneously, which will lead to random crashes. The multiple threads are necessary to readout data and update the GUI, while a measurement is running. The class `ThreadManagement` takes care of the individual threads. It prevents that one thread is used twice at the same time and takes care of the process of killing a thread, if necessary.
`DeviceManagement` takes care of a similar situation. Most devices should not execute two tasks at the same time. To prevent an unintentional misuse, a device manager takes care of the administration of the tasks for the individual devices.

[1] From its homepage https://epics.anl.gov: "EPICS is a set of Open Source software tools, libraries and applications developed collaboratively and used worldwide to create distributed soft real-time control systems for scientific instruments such as a particle accelerators, telescopes and other large scientific experiments."

[2] Signal and slots are used for the communication between two objects within the code. The communication is based on turns. E.g. object A wants to change the value in object B, but they are in different threads. A direct access from A to B could lead to a crash. To avoid this kind of crashes, A emits a signal to the slot of B to change its value. The signal and slot manager, which is implemented in PyQt takes this signal at the next turn and then changes the value of B safely.

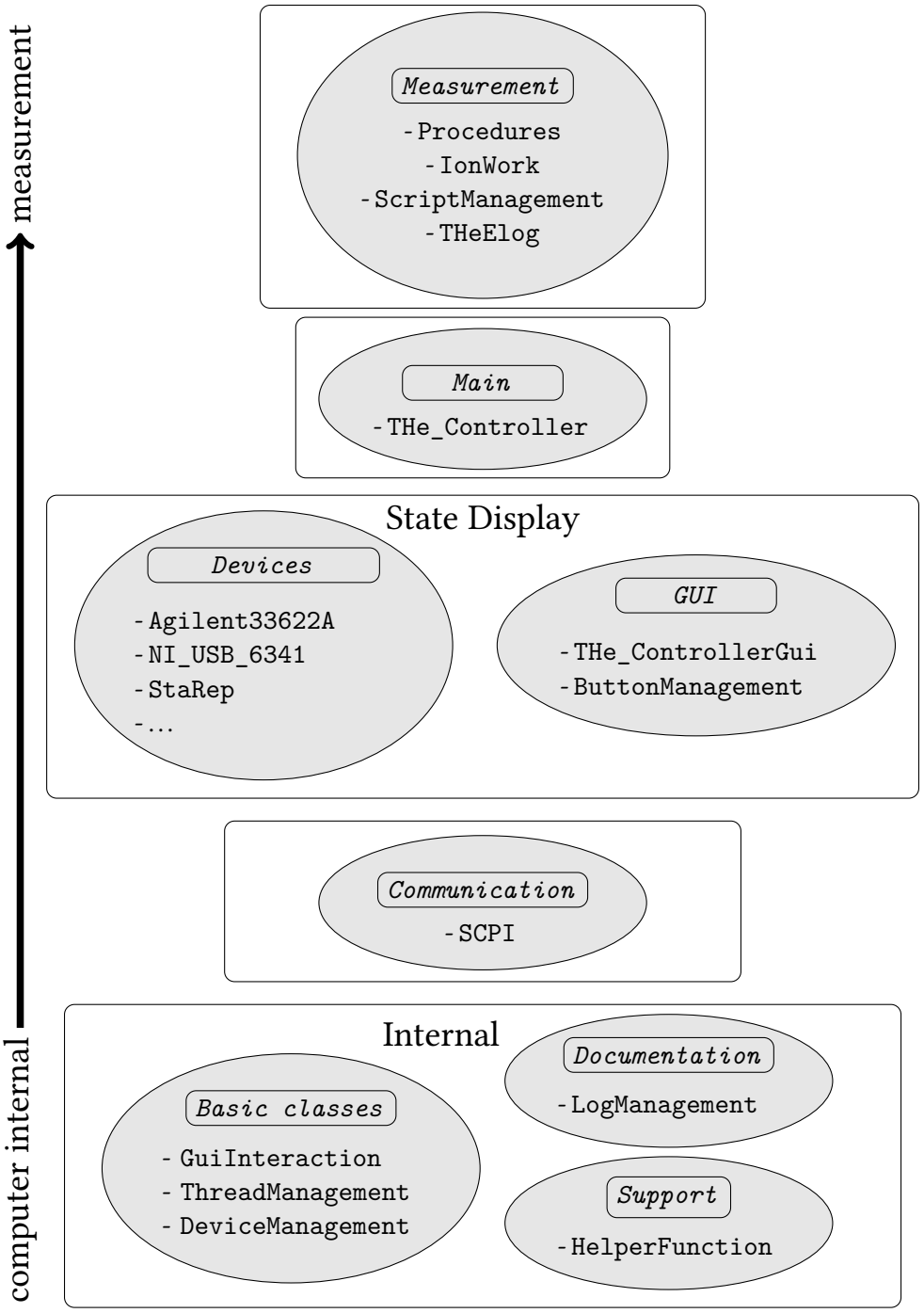

Figure 5.1.: Schematic representation of the hierarchical structure of the new THe-Trap control system. The names marked with hyphens represent class names. The names in the boxes are a rough description of their functionality. The further up in this diagram a class is drawn, the closer the programming is on the side of the measurement. All program parts can be inherited upwards. The other way round it is excluded. More information in the text.

The *Support* area contains functions that return the current directory for storing the data as well as the time and date in the previously used format. This has the advantage that already existing analysis scripts can be re-used.
The *Documentation* area consists of the LogManagement. All commands leaving the computer will be stored as well as any returned value. All errors occurring in the code are caught by the LogManagement, displayed in the GUI and stored in a log file. If the GUI crashes, the reasons can be traced here later. In addition, the LogManagement is responsible for saving the current settings in the program and contains the basic routine of reading these settings from a file and feeding them into the program. This helped the development of the control system especially in the early days, as the control system had to be restarted frequently.

5.2.2. Communication

The *Communication* section, including the class SCPI (abbreviation for Standard Commands for Programmable Instruments), controls all communication that leaves the control system. In the process of the development of the new control system a lot was changed to ethernet based TCP/IP. Previously, mostly serial communication protocols were used like GPIB and USB. GPIB has the problem that the order of the connected devices matters. Communication via USB is also not ideal due the limitation of USB cables to 5 m. These problems are overcome with Ethernet and TCP/IP. Communication via TCP/IP, however, has no guaranteed runtime and is more error-prone than GPIB or USB. The TCP/IP protocol raises an error, if the communication is not successful. When the error is raised depends on the settings for the individual TCP/IP protocol, as e.g. the waiting time for a response in TPC/IP can be set individually. It is important that failed transmission attempts are recognized by the program and the user is informed, but it does not crash the whole control system. The user will be informed by a message in a debug area of the GUI. The control system will try to resend the command three times. Only if the command could not be transmitted despite multiple retransmissions, another error message is issued and the process is aborted. This procedure is regulated for all devices in this class. USB cannot be completely avoided, so that communication via USB is also controlled in this class. The same applies to internal timing and general input output cards controlled via PCI and PCI-Express, since possible malfunctions must also be detected and handled.

5.2.3. State Display

The next hierarchical level moves clearly away from direct coding concepts and turns to the application or the user. The *Devices* section contains all devices and their tasks. If, for example, a frequency sweep (see Section 4.2) should be performed, a function for this is available in the class of the frequency generator. These functions require the sweep width, duration, excitation amplitude and direction as input parameters. The function sends the necessary commands to the frequency generator by using the inherited class SCPI.
In the *GUI* area, the concept of the "State Display Machine" is implemented. The class THe_ControllerGui contains the source code of the GUI, which is shown in Figure 5.2. All experiment related values are stored in the GUI, so the user always has the same knowledge on the processes in the experiment as the control system. ButtonManagement connects the buttons of the GUI

with the underlying functions. In addition, `ButtonManagement` ensures that buttons containing a certain task change color from green to red when pressed. As soon as the task is completed, the button is reset to green to show the user that the task is finished. This color change shows the current status to the user. In the software implementation of this color change the concept of the decorator is very useful. Instead of needing an individual line of code within the declaration of the button, the same decorator is always placed at the declaration. If the behavior of the `ButtonManagement` has to be changed, it is done only in the source code of the decorator.

5.2.4. Main

The class `THe_Controller` is the main interface. All preparations made to control the experiment converge here. In addition, global variables are defined, for example to put the entire program into debug mode. This mode is useful to test the program without actually sending commands.

5.2.5. Measurement

The next and last area leaves the basic concepts of coding and turns to experimental daily routines. In the `ScriptManagement` all essential commands for the external scripts are defined. `ScirptManagement` is therefore imported in every external script. These new external scripts are written with Python and the full capabilities of Python are available to them, while the old scripts were written in the custom-made language THe-Script. This is a significant advantage over the old concept as only certain commands were available then. Nevertheless, also the class `ScriptManagement` contains functions to handle repetitive tasks consistently. For example, it consistently defines the way buttons can be pressed from the script in the GUI, values can be set in numeric fields, or other scripts can be loaded into a new script.
`IonWork` is the next level of abstraction and therefore placed one entry above `ScriptManagement` in Figure 5.1. As already shown in Section 4.2, the tasks at the experiment are very repetitive. In `IonWork`, common tasks are defined, for example a frequency sweep. To perform a frequency sweep, the control system has to read the corresponding frequencies, frequency steps, duration and amplitude from the GUI. These parameters have to be passed to the corresponding function of the function generator class and the function generator has to be started. The next abstraction takes place in the Procedure class. While `IonWork` mainly contains functions that only access one device, the class `Procedures` defines processes with several devices. One of them is e.g. loading ions, where the routine of setting the correct electrode voltages, switching off the drive (see Section 4.2.1) and many more are defined in the code based on experience and do not need to be changed regularly. The function in `Procedures` to load ions takes only four parameters concerning the control of the high-voltage source which need to varied often. The process of loading ions is fully automatic and highly reliable. This function enables scripts like "12C4" to be written, which then removes an old ion, loads new ones and cleans the trap until only one ion is left.
In November 2015 THe-Trap moved from analog log books to the electronic laboratory book ELog[3]. All events of the experiment are manually but digitally recorded. There is also an

[3] https://elog.psi.ch/elog/

interface from the control system to this documentation tool, so that scripts can write ELog entries. In addition, unusual events can also be entered there from the control system.

Overall, the migration to the new control system has been successful. All functionalities of the old control system have been implemented in the new one including the devices that had to be replaced. In addition, the possibility to use Python directly as a script language to control the experiment is a considerable simplification in daily experimental routines. The change of the measurement concept to PnP was tested successfully from control system side. Unfortunately, experimental problems prevented a complete change to this method.

5.3. Realization and examples of application

In this section, first a brief introduction of the structure of the GUI is given. This includes important parameters, which are displayed in the main tab of the GUI, and how the status of the experiment can be seen at a glance. Afterwards, an example measurement script is presented.

5.3.1. Graphical user interface

The GUI shown in Figure 5.2, consists of several tabs. The Main tab, the only one shown here, contains all essential functions and parameters that are frequently used and changed. The other tabs can be found in Appendix A.
The Main tab is segmented into several sectors. The sector "Frequencies" contains the current estimations of the three eigenfrequencies (see Equations (2.6) and (2.7)) for the ion in the trap. These values are needed for various processes, e.g. quadrupolar excitations to couple the modes of the ion for cooling. The subsector "Sweep" contains the parameters for the frequency determination (see Section 4.2.1). At the right side of this area, it can be toggled between the "Mag" and "Cyc", which stands for the determination of the magnetron and cyclotron frequency mode, respectively. It can also be chosen, if an up- or down-sweep shall be performed. The center frequency of the sweep is taken from the values above. The reasons for the red color of one the buttons and the greyed-out elements is given later. Further left the GUI area for "Pulse and Phase" and "Axial Pulse" can be found. The "Pulse and Phase" was written for a change to a PnP measurement and "Axial Pulse" can be used to detect the ion in the case it is not in lock (see Section 4.2.1). On the very right of the GUI the area for the "Scripts" can be found. A few buttons in the area of "Scripts" still have the name "Script + Number", because no measurement script is linked to this button. The scripts are written in individual Python files and do not need to be defined and present when the GUI is started. They can be created and changed during the run time of the control system. To link a script button to a script, the button has to be right clicked first. This right click opens a file dialog, where the user can choose the desired measurement script. The control system will automatically change the label of the button from "Script + Number" to the file name of the measurement script. The next time the user left clicks on the button where the script is linked to, it is imported into the running control system and executed. This import is performed at every left click to ensure that an update in the measurement script is always taken into account. Below the "Scripts" sector is a table containing variables, which can be accessed by all scripts. Additionally, the variables can be created, deleted, and changed manually at any time by the user. This has the advantage that

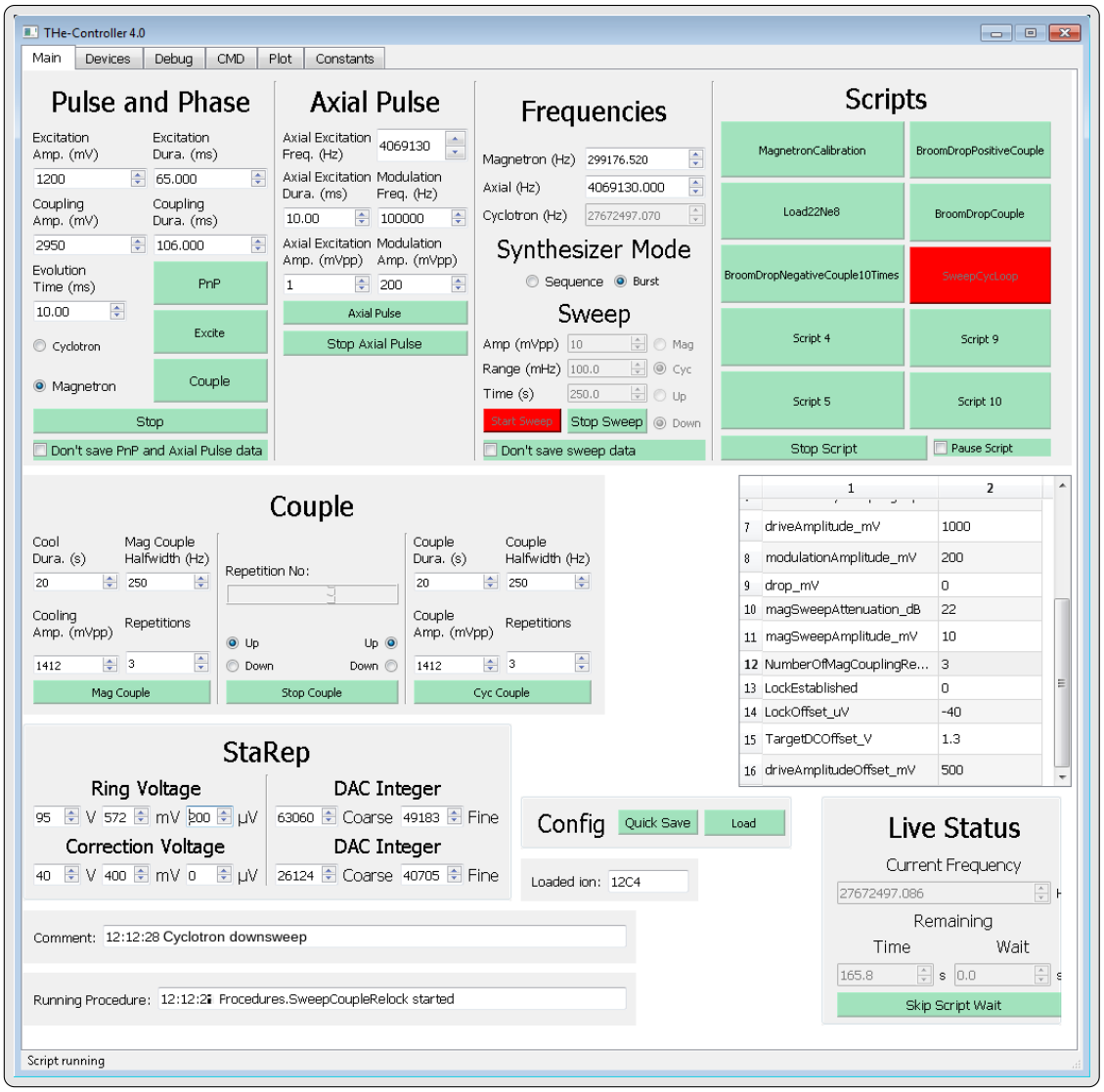

Figure 5.2.: GUI of the control system called THE-CONTROLLER. For better overview there are several tabs (Main, Devices, Debug, CMD, Plot, Constants). The other tabs are shown in Appendix A. Currently the script "SweepCycLoop" is running and it is performing a sweep. Both can be recognized by the red buttons. In the lower right corner of the Live Status it can be seen that the sweep will last 165.8 seconds. On the left side "Running Procedure" indicates that SweepCoupleRelock is running. More information in the text.

if these variables are used in the scripts, they can be changed during the run-time of the script without the need to restart it. Below of this table the live status can be seen. It shows which frequency is currently being applied to the trap and the remaining time until a sweep, if it is running, is finished. Left of "Live Status" two lines can be found:

The "Comment" field can be set with individual text from the scripts, giving the opportunity to set user comments. The field of "Running Procedure" is automatically updated every time a "Procedure" (see Figure 5.1) is executed. The time stamps in front of the strings in both fields are created automatically, in order to prevent confusion from outdated messages.

As mentioned before, the main purpose of the GUI is to display the current status of the experiment. This is done by the color of the buttons and greying out numeric fields. All green buttons can be pressed and all non greyed out numbers can be changed. All red buttons are currently pressed and indicate a running process. Thus, it is directly obvious that the script "SweepCycLoop" is executed. This script is explained in more detail in the next section, but without knowing the script exactly, it can be seen that it performs a 250 s long, 100 mHz wide cyclotron down sweep, because of the red "Start Sweep" button, the content and the position of the greyed-out elements in the "Sweep" section. The "Live Status" indicates that 165.8 s of the 250 s are left and the timestamp of "Comments" indicates that it started at "12:12:29". When the sweep finishes, sweep button will turn green again and all sweep fields will be available again.

5.3.2. Measurement script

In Figure 5.2 it is indicated that the external script "SweepCycLoop" is executed. The source code is shown in Figure 5.3. This script executes an endless loop of cyclotron sweeps (see Section 4.2.1) to determine the cyclotron frequency (see Equation (2.7)) and it serves mainly as a framework for the function "Proc.SweepCoupleRelock". The variable *Proc* is an object of the class `Procedures` explained before (see Section 5.2.5). This process performs a sweep based on the parameters set in the GUI, cools the ion after the sweep and brings it back to lock (for the explanation of "in lock" see Section 4.2.1) after the cooling. It returns true, when it was successful in bringing the ion to lock. The task of the script is to perform this loop until the ion is not in lock after "SweepCoupleRelock" has finished, so the variable *ionInLock* is false or the user set the variable *sweepOn* in the table in the GUI to zero. In these cases, the loop will stop safely at the next turn. Additionally, the script changes the direction of the sweep every turn, sets the comments by the function *Proc.SetComment* and reads out the variables for the table through the function *Proc.GetVariable*, so that the sweeps can be adjusted, when the script is running. The *Elog* variable can be used to write to the electronic lab book. The variable *MainController* in Figure 5.3 gives access to all variables of the control system. This feature must be handled carefully, as this option allows manipulation of all variables. Careless manipulation of the main variables can lead to program crashes.

```python
import time
from Procedures import Procedures
from THeElog import THeELOG
from THe_Controller import Main as THeController

def main(MainController: THeController, ScriptPath):
        time.sleep(0.5)
        Proc = Procedures(MainController)
        Elog = THeELOG(MainController)
        Elog.WriteMessage('SweepCycLoop',
                'Started Cyclotron sweep loop', ScriptPath)
        Proc.SetVariable("sweepOn", 1)
        Proc.SetComment("Cyclotron sweep loop started")
        SweepDirection = 1
        ionInLock = True
        BaseLockVoltage_V = 0

        while Proc.GetVariable("sweepOn") and ionInLock:

                if SweepDirection == 1:
                        Proc.SetComment("Cyclotron upsweep")
                else:
                        Proc.SetComment("Cyclotron downsweep")

                ionInLock = Proc.SweepCoupleRelock(
                        'Cyclotron', SweepDirection = SweepDirection,
                        SweepRange_mHz = Proc.GetVariable(
                        "cycSweepWidth_mHz"),
                        SweepAmplitude_mV = Proc.GetVariable(
                        "cycSweepAmplitude_mV"),
                        NumberOfCouplingRepetitions = Proc.GetVariable(
                        "NumberOfCycCouplingRepetitions"),
                        PulseAttenuation_dB = Proc.GetVariable(
                        "cycSweepAttenuation_dB"),
                        BaseLockVoltage_V = BaseLockVoltage_V)
                Proc.SetComment("Cyclotron sweep finished")

                if SweepDirection == 1:
                        SweepDirection = -1
                else:
                        SweepDirection = 1
```

Figure 5.3.: Shown is the measurement script "SweepCycLoop", which performs a cyclotron sweep, cools the ion, puts it back into the lock, changes the sweep direction and performs a new sweep. More information in the text.

6. Image charge shift simulation

The following chapter is similar to and contains parts of the publication "Image charge shift in high-precision Penning traps" by Schuh *et al.*, which is to be published in 2019 [SHE+18]. As already mentioned in Section 2.2.1, an ion in a PENNING trap induces image charges on the surface of the trap electrodes. They cause a systematic shift of the ion's free-space cyclotron frequency, typically at a relative level of several 10^{-11}, by slightly distorting the electric trapping potential. In contrast to other systematics, the image charge shift (ICS) cannot be reduced by a lower temperature of the ion or an improved detection method. As the ICS scales inversely with the cubic trap radius (see Equation (2.18)), the only way to reduce this shift is to increase the size of the PENNING-trap electrodes. But the induced image charges are needed to detect the ion's motion (see Section 4.2.1) and a possible increase of the trap electrodes is limited by the simultaneous linear decrease of the detection signal. An alternative to the increase of the trap size is a precise measurement or calculation of the ICS.
A measurement of the ICS is experimentally difficult as it requires two axial detection systems tuned to the axial frequencies of the two different ions for the same voltage [SHE+18]. Therefore, providing a possibility to directly simulate the magnitude of this effect and correct for the shift is very helpful for PENNING-trap experiments aiming for the highest precision. The ICS was measured for the first time by observing the magnetron frequency shift as a number of the stored ions by Van Dyck *et al.* in 1989 [vDMFS89]. The measurement confirmed an extremely simple analytical model on a 17% uncertainty level. There, the hyperbolic geometry of the trap electrodes has been approximated by a sphere. Subsequently, Häffner derived an analytical first order calculation for cylindrical PENNING traps in 2000 [Häf00] by approximating the segmented electrodes as infinitely long cylinders (see Equation (2.18)). Soon afterwards, an elaborate semi-analytical model was developed in 2001 by J. V. Porto, which was applied on hyperbolic traps [Por01]. Its prediction got confirmed on a 4 % level by Van Dyck *et al.* in 2006 [vDPVLZ06] by using the same method as before. Proto's method has been reanalyzed in detail in our work and a short summary is given here, as it serves as a systematic check for a new approach discussed below. A further refined analysis has been modeled by Kretzschmar and others considering also vertical and horizontal slits of cylindrical traps [SWK+13]. Also here the ICS was corrected with an uncertainty at a 5 % level. All these methods above are limited by the fact that complicated shapes of the electrodes have to be simplified in order to evaluate the ICS theoretically. Especially slits and edges are challenging to be modeled in semi-analytical treatments. Simulations based on the finite element method (FEM) (see Section 3.1), as discussed, below can overcome these problems with the trade-off of high demand in computational power. A cluster node with 32 cores and 256 GB of RAM was used to carry out the simulations.
In this chapter, first, the general concept of the simulation of the ICS is introduced (see Section 6.1), followed by the trap geometries which are taken into considerations (see Section 6.2). In Section 6.3 the uncertainty estimation within the FEM is introduced. In the subsequent

section (Section 6.4) the independent semi-analytical treatment on numerically calculating the ICS is presented. In order to apply this method, the complexity of the considered PENNING-trap geometry has to be reduced, which limits its applicability to real PENNING-trap setups. Nevertheless, its different ansatz helps to analyse the simulation for systematic problems when also the FEM simulation is applied on the simplified geometries. In the Section 6.5, the results of the simulation, semi-analytical treatment and recently performed measurements are compared.

6.1. General concept

In this section, the process to simulate the Linear Field Gradient (LFG) $\mathcal{E}_\rho$ and $\mathcal{E}_z$ according to Equation (2.16) is presented. For the FEM simulations the program COMSOL MULTIPHYSICS™ is chosen (see Section 3.1.2). The desired trap geometry is reconstructed in the software and simplified by removing all structures not essential for the simulation, e.g. grooves on the outside of the electrodes. It is enough to simulate the essential shaping components of the electrodes. The ion, which is assumed to be a point like charge (PLC) with one elementary charge is placed inside the trap. In the next step all boundary conditions are set, e.g. all electrode surfaces are perfect conductors and at ground potential. Vacuum is assumed in the space between the electrodes and the PLC. The geometry is meshed (see Section 3.1) and the LAPLACE equation is solved as described in Section 3.1.1. One part of the solution to the differential equations, which COMSOL MULTIPHYSICS™ returns, is among other parameters such as the potential or the electric field, also the induced surface charge density σ of the surrounding electrodes (see Figure 6.1). The electric field, which is generated by the induced image charges on the electrode surfaces can be calculated at the position of the ion by

$$\vec{E}_{\text{image}} = -\int \frac{\sigma(x,y,z)}{4\pi\epsilon_0} \frac{\vec{x}-\vec{x}'}{|\vec{x}-\vec{x}'|^3} \mathrm{d}A \quad . \tag{6.1}$$

This integral is directly carried out within COMSOL MULTIPHYSICS™. The variable $\vec{x}'$ corresponds to the coordinate of the PLC, the unprimed letters (x, y, z) are the integration variables. In the simulation the position of the PLC is changed $-0.5\,\text{mm}$ to $+0.5\,\text{mm}$ in $0.05\,\text{mm}$ steps along the x axis and for each step the electric field generated from the induced image charges on the electrode surfaces is calculated at the position of the PLC. The resulting electric field strengths at the 21 different PLC positions are fitted by an odd polynomial function because of the symmetry with respect to the trap center. The linear coefficient of these fit polynomials is the sought after $\mathcal{E}$ (see Equation (2.16)). The higher orders are needed due to the small presence of higher order terms in the image charge field. Even though it is shown in Section 6.3 that the higher order coefficients do not need to be taken into account for the frequency shift, they change the first order coefficient significantly (see Figure 6.2) when they are added to the fit.
Four systematic uncertainties must be taken into account for the final ICS:

1. Numerical uncertainty:
   The mesh is an approximation of the real geometry. The size of the smallest mesh element represents the accuracy of the trap geometry in the simulation. The smaller the size, the better the geometry is described by the system of equations (see Section 3.1). Unfortu-

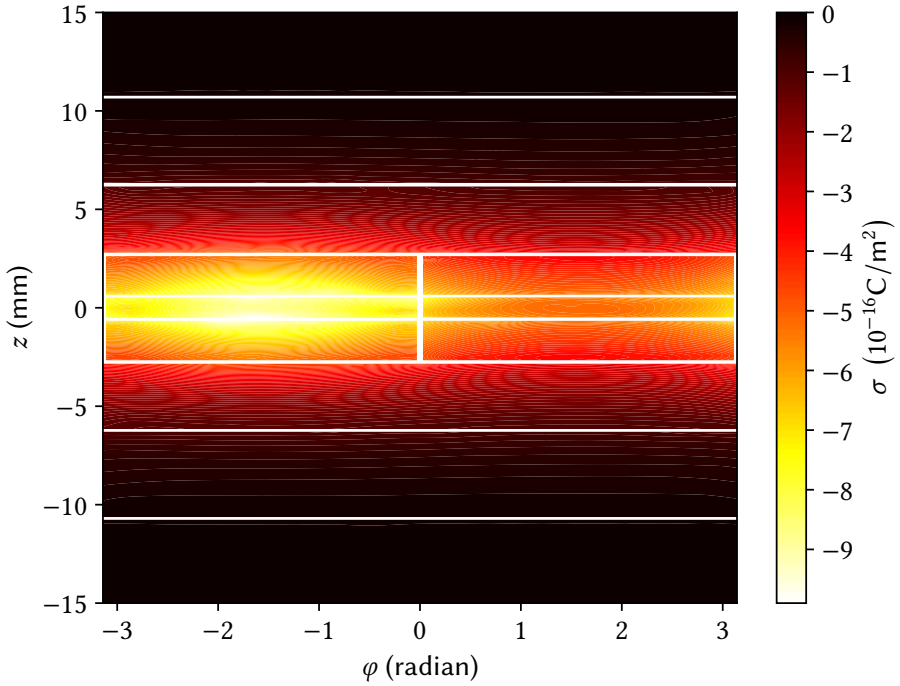

Figure 6.1.: Illustration of the numerical calculation of the surface charge density σ (see Equation (6.1)) on the electrodes of a cylindrical PENNING trap induced by a single charged particle. A projection of the surfaces of the trap electrodes of the cylindrical LIONTRAP (see Section 6.2.2) into the plane is shown. The trap displayed here has nine electrodes instead of the three shown in Figure 2.1b, which are needed experimentally to apply harmonic potentials. The three inner electrodes are split in two at $\phi = 0$. The charge is radially displaced by 0.5 mm from the center at $\varphi = -\frac{\pi}{2}$.

nately, if the result of the simulation does not change when the mesh size is decreased it does not mean that the simulation returns an error-free result. From comparison of simulations, where the analytic solution is known it can be seen, that the simulation mostly converges to a result, which is slight off of the unknown correct result. In order to test the simulation for a systematic deviation stemming from the chosen mesh size, a case with an analytic solution, which is close to the investigated case, should be simulated.

2. Fit uncertainty:
   The electric field created by the image charges at the different ion position has to be described by a polynomial to retrieve $\mathcal{E}$. The used fit functions gives an uncertainty of the result, as well. This cannot be disentangled from the uncertainty introduced above, even though their origins are different. Both 1. and 2. are therefore, summed up in the uncertainty denoted with $()_{\text{num}}$.

3. Geometric uncertainty:
   The geometric uncertainty caused by tolerances in the manufacturing process. The real electrodes can deviate from the design value by approximately up to ±10 µm. The uncertainty stemming from this is denoted by $()_{\text{geo}}$.

4. Higher order terms:
   The effect of higher order terms in the image charge field can become seizable in the case of large motional radii or if the electrostatic center of the trap is shifted with respect to the geometrical center. Reasons for this shift can be for example, alignment imperfections or patch potentials. The higher order terms contribute to the ICS typically less than 0.1 % and are thus, as shown in Section 6.3, negligible compared to manufacturing tolerances.

Further details can be found in Section 6.3.

6.2. Trap setups

In the following, three real and one purely theoretical trap setups are introduced for which the ICS is investigated. An overview of the characteristic parameters z_0 and ρ_0 is given in Table 6.1.

Table 6.1.: Overview of the characteristic trap dimensions. All values are given at a temperature of 4 K. A manufacturing tolerance of ±10 µm is assumed for all trap dimensions. More information is given in the text.

properties	FSU-Trap/Porto-Trap	THe-Trap	Liontrap
type	hyperb.	hyperb.	cylind.
ρ_0 (z_0) (mm)	6.96 (6.00)	2.77 (2.29)	5
d (mm)	5.501	2.124	5.107
B_0 (T)	8.529	5.915	3.764

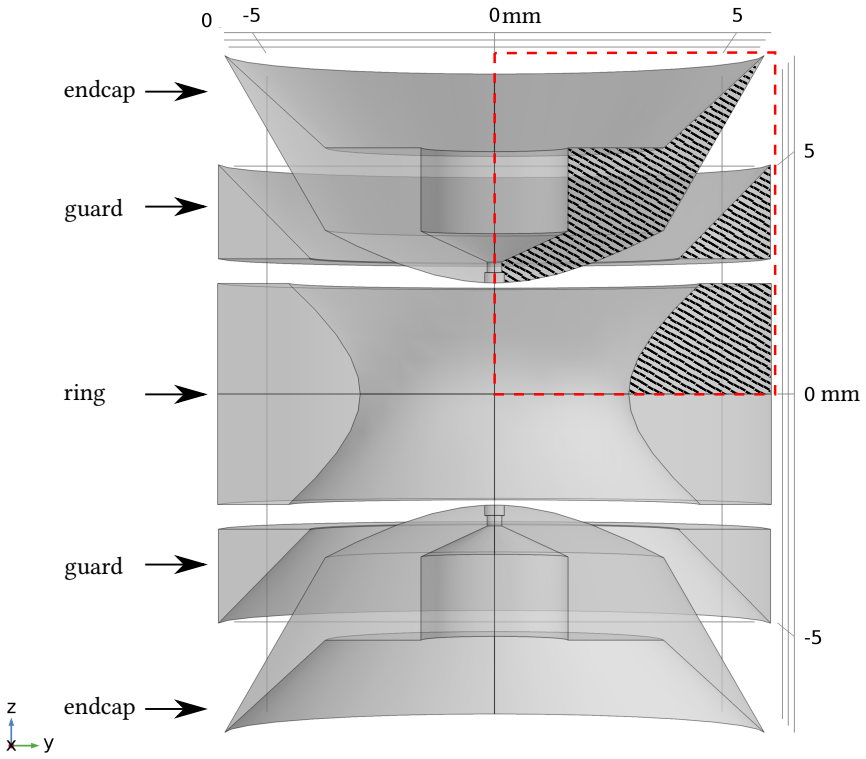

Figure 6.2.: A semitransparent cut-view of the electrode geometry of THe-Trap. The hatched area enclosed by the red dashed line is shown enlarged in Figure 6.3 (a). See text for more details.

6.2.1. THe-Trap

The mass-measurement trap of the THe-Trap experiment, presented in Section 4.2, consists of a hyperbolically shaped ring electrode, two endcap electrodes and two guard electrodes, see Figure 6.2. In general, due to the rotational symmetry along the z-axis and the mirror symmetry along $z = 0$, the full information of the trap geometry can be obtained from looking at one quarter of a cut (see hatched area surrounded by the red dashed line in Figure 6.2) of the whole trap. For the other two traps, therefore, only this quadrant is shown (see Figure 6.3).

6.2.2. Liontrap

The measurement trap (MT) of the Liontrap [Kö15] experiment is a cylindrical Penning trap and consists of eleven electrodes, see Figure 6.3 (b). The characteristic parameter z_0 is given in Table 6.1. The inner three electrodes (the ring and C_1) are all azimuthally split into two pieces, which allows applying different radio-frequency multipoles. The gap between the segments is also 140 µm.

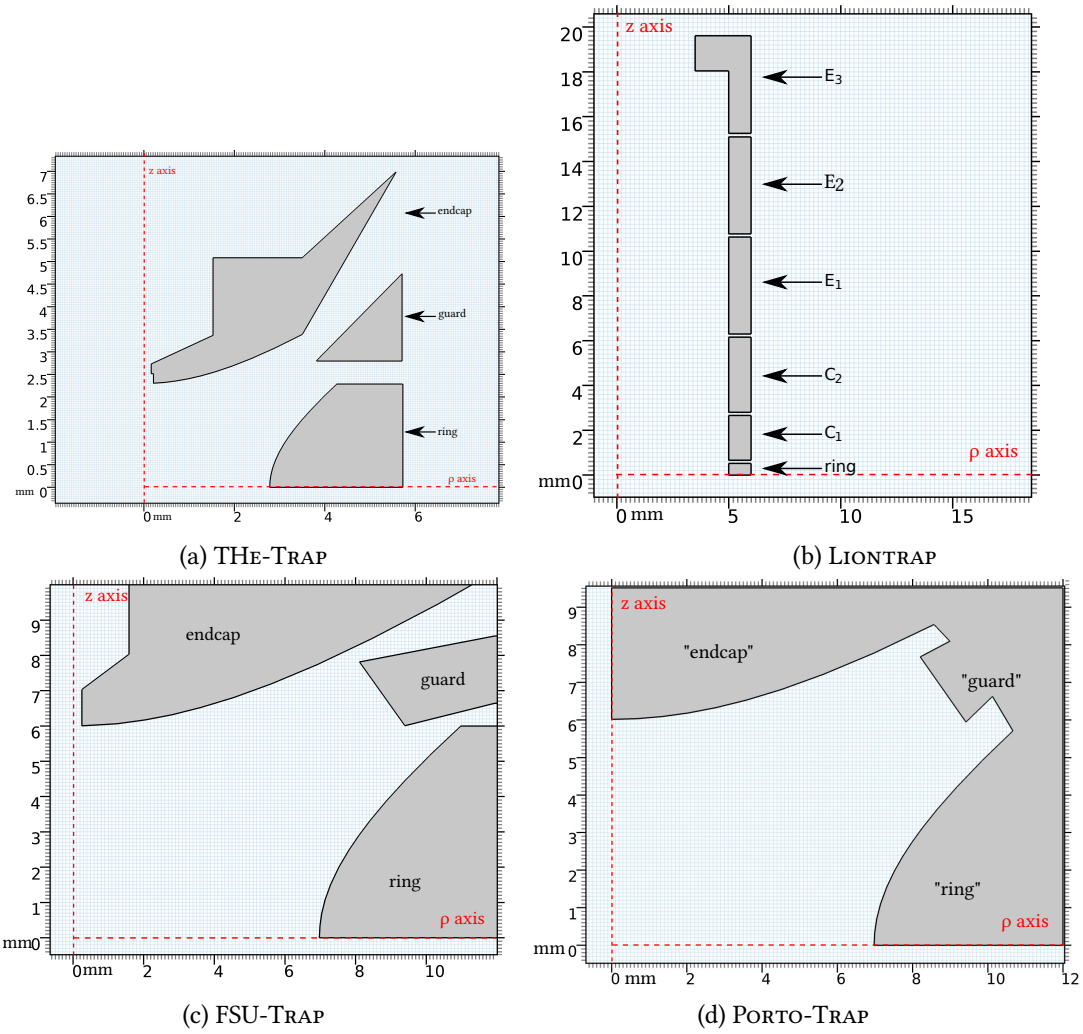

(a) THe-Trap (b) Liontrap

(c) FSU-Trap (d) Porto-Trap

Figure 6.3.: Electrode geometries of the four investigated trap geometries. The full geometry is obtained by revolving the shown geometry around the z-axis and mirroring along the $z = 0$ plane. In (b) vertical slits have to be considered partly in the ring and correction electrodes.

6.2.3. FSU-Trap

The FSU-Trap is a hyperbolic Penning-trap mass spectrometer. Similar to THe-Trap, it consists of a ring, two endcap and two guard electrodes, see Figure 6.3 (c). The characteristic parameters z_0 and ρ_0 are given in Table 6.1.

6.2.4. Porto-Trap

The (theoretical) Porto-Trap is identical to the FSU-Trap concerning the characteristic dimensions z_0 and ρ_0 but simplified in respect to the guard electrode (see Figure 6.3 (d)). This geometry is used by J. V. Porto for his semi-analytical treatment in [Por01] to predict the ICS for the FSU-Trap. The Porto-Trap is analyzed here again by the semi-analytical approach and by a COMSOL multiphysics™ simulation. This offers the chance to compare the new semi-analytical result with the result achieved by Porto in 2001 and to perform the already mentioned systematic test of COMSOL multiphysics™. In the geometry, there are no holes in the endcap electrodes, no slits and the correction guard electrode geometry is simplified by slightly changing the orientation of the guard electrode and the space between the electrodes is closed. These modifications are necessary to make the semi-analytical treatment possible (see Section 6.3). Note, this trap has never existed in reality, because the connection between the electrodes makes it impossible to apply different potentials, which are needed to create a trapping potential.

6.3. Uncertainty approximation

In Section 6.1 the estimation of the uncertainties of the simulations is roughly described. A detailed explanation of the four sources of uncertainty is given below.

6.3.1. Numerical uncertainty

For the determination of the numerical uncertainty an electrode geometry should be simulated where the analytic solution is known. The relative deviation of the simulation result from the analytic solution can then be taken as an approximate numerical uncertainty for other Penning traps. The easiest geometry for this purpose is a PLC in a hollow sphere, where simulation and analytic solution agree perfectly. Thus, this case cannot be used to estimate the numerical error because it is too simple and deviates too much from the geometry of a Penning trap. A more applicable case is that of an infinite cylinder. The representation of an infinite cylinder is of course, impossible, but a ratio of length to radius of bigger than ten allows to suppress sufficiently the effects at the end of the cylinder in the center. The cylinder is closed at both ends with a flat plate to set the necessary boundary conditions for the simulation. The image charge electric field E_{image} at the position of the PLC is predicted by the analytic solution [TB01, Bar03, SWK+13] to be

$$E_{\text{image}}(\rho) = n \cdot 1.0027 \frac{e}{4\pi\epsilon_0 \rho_0^3} \cdot \rho = n \cdot \tilde{\mathcal{E}}_\rho \cdot \rho \quad , \tag{6.2}$$

Table 6.2.: The relative deviation $\Delta\mathcal{E}$ of the simulated linear field gradient $\mathcal{E}_\rho$ from the analytical prediction $\tilde{\mathcal{E}}_\rho$ (see Equation (6.2)) in a hollow cylinder with various radii. The optimal fit order gives the order of the point symmetric polynomial that has to be chosen to minimize $\Delta\mathcal{E}$.

experiment	cylinder radius ρ_0 (mm)	optimal fit order	$\Delta\mathcal{E}$ (10^{-4})
THe-Trap	2.78	5	8.1(2.4)
Liontrap	5	5	7.3(1.2)
FSU-Trap	6.96	3	5.7(5)

where $\rho = |\vec{\rho}|$ is the distance of the PLC from the center of the cylinder, e the elementary charge, n the charge state of the PLC and ϵ_0 the vacuum permittivity. A new LFG is introduced as $\tilde{\mathcal{E}}_\rho = 1.0027\frac{e}{4\pi\epsilon_0\rho_0^3}$. The searched for $\mathcal{E}_\rho$ is simulated as described in Section 6.2. To represent the geometry sufficiently well an average mesh density of 30 – 100 mesh elements per mm^2 has to be chosen. At this mesh density the result of the simulation does not change, when the mesh size is decreased further. The mesh algorithm in COMSOL Multiphysics™ ensures that areas with small structures, such as the slits in the electrodes, are meshed with the smallest element size. Then, the mesh size is increased gradually towards areas with less details, e.g the vacuum between the electrodes. Hence, the size of the smallest mesh is about 1 µm and the largest about 500 µm. The smallest mesh is ten times smaller than the manufacturing tolerances. All simulations in the following section have a mesh density in this range.
As a consistency check the LFG in z-direction is simulated, too. Due to the translation invariance of an infinite cylinder, no significant LFG in this direction is expected. The resulting $\mathcal{E}_z = 1.5(3.1)\,\mu\text{V/mm}^2$ is consistent with zero within the fit error bars.
The ICS and $\mathcal{E}_\rho$ are investigated for three different cylinder radii (see Table 6.2), corresponding to the three different ρ_0 of the investigated Penning-trap geometries (see Section 6.2). The same mesh settings are taken for the respective trap geometries. The relative deviation of the simulated results from the analytical prediction $\tilde{\mathcal{E}}$ is calculated as $\Delta\mathcal{E} = \left|(\mathcal{E}_\rho - \tilde{\mathcal{E}}_\rho)/\mathcal{E}_\rho\right|$. An example analysis can be found in Figure 6.4. In the analysis of the cylindrical simulations it turns out that higher than first orders of point symmetric polynomials are needed to minimize $\Delta\mathcal{E}$. This is caused by the non-orthogonality of the coefficients of the polynomials. Even though only the linear order is of interest, the linear order coefficient changes, if higher orders are included. The mesh density in this figure is on the lower side of the range mentioned in the text, because COMSOL Multiphysics™ does not choose the minimal mesh size for a cylinder without any slits or edges. Forcing it to do so for the complete cylinder would lead to a memory lack. The systematic uncertainty $()_{\text{sys}}$ is estimated from the cylindrical test case

$$()_{\text{sys}} = \mathcal{E}_{\rho,z} \cdot \Delta\mathcal{E} \quad , \tag{6.3}$$

where $\mathcal{E}_{\rho,z}$ are the LFG of the simulated trap geometries and $\Delta\mathcal{E}$ is taken from Table 6.2.

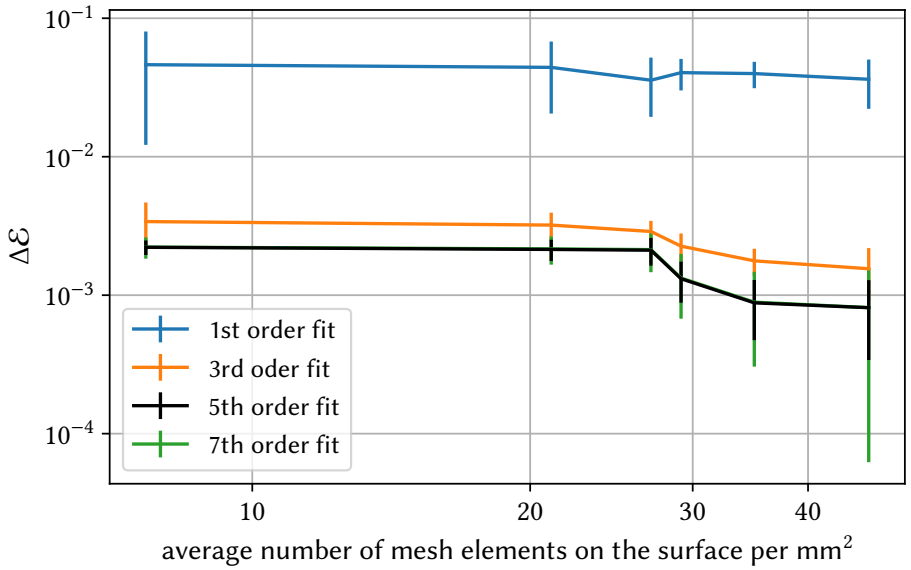

Figure 6.4.: Relative deviation of the simulated ICS of a PLC inside a hollow cylinder with radius 2.78 mm and a total length of 30 mm compared to the analytical calculation as a function of the mesh size. While the linear fit does not show any significant decrease of $\Delta\mathcal{E}$ for a finer mesh, higher order polynomials do. Finally, the 5th order polynomial is sufficient to minimize $\Delta\mathcal{E}$. Higher order polynomials than the 5th order describe the data as well as the 5th degree polynomial but with a larger uncertainty.

6.3.2. Fit uncertainty

The LFG $\mathcal{E}$ is determined by a fit. This fit has an uncertainty, too. In the simulations of all trap geometries the PLC is moved along all three axes even though the simulated geometry is rotational symmetric. This offers the possibility to compare $\mathcal{E}_x$ and $\mathcal{E}_y$ as the meshing algorithm in COMSOL MULTIPHYSICS™ breaks the rotational symmetry. $\mathcal{E}_x$ and $\mathcal{E}_y$ are averaged to $\mathcal{E}_\rho$ and their deviation from each other is added in quadrature as an additional uncertainty to the existing $1\,\sigma$ fit uncertainty $()_{\text{fit}}$. Their deviation is on a relative 10^{-5} level. Finally, $()_{\text{sys}}$ and $()_{\text{fit}}$ are joined by GAUSSIAN error propagation into $()_{\text{sim}}$, which is given in Table 6.3. This is maybe an overestimation, because the systematic uncertainty is determined by a fit and therefore includes already part of the fit uncertainty.

6.3.3. Geometry uncertainty

The manufacturing parameters do not necessarily represent the actual geometry. There are manufacturing tolerances, which have to be taken into account. To approximate the influence of the geometry on the result, the worst case scenario is considered. The characteristic trap parameters ρ_0 and z_0 are enlarged by 10 µm. The guard electrodes are shifted up- and outwards by 10 µm, too. The difference in $\mathcal{E}$ between the two geometries is taken as the geometrical uncertainty $()_{\text{geo}}$.

6.3.4. Higher order terms

The higher order terms of the image charge field can be parameterized by

$$\vec{E}_{\text{image, h.o.}} = n \cdot \mathcal{E}_{\text{h.o.}} \cdot \rho^3 \cdot \vec{e}_\rho \quad . \tag{6.4}$$

The prefactor $\mathcal{E}_{\text{h.o.}}$ is the scaling of the higher order (h.o.) effect. Effects in the z-direction are neglected as they are typically strongly suppressed by the usage of the invariance theorem and in the case of cylindrical traps additionally by the inherent symmetry.
If, without loss of generality, a parasitic shift $\hat{\rho}_0$ of the trap center in the ρ-direction is assumed, this leads to the leading order of an effective, additional image charge field of

$$\vec{E}_{\text{image, h.o. eff.}} = 2n \cdot \mathcal{E}_{\text{h.o.}} \cdot \hat{\rho}_0^2 \cdot \rho \cdot \vec{e}_\rho \quad . \tag{6.5}$$

Independent measurements show that it is reasonable to assume $\hat{\rho}_0 < 50\,\mu\text{m}$ [SWSB11]. The higher order terms contribute to the ICS, therefore, by less than relative 10^{-2} and are thus negligible compared to manufacturing tolerances.

6.4. Semi-analytical treatment

The finite element method has become so powerful due to the increase in computer processing power in recent years that even geometries with many details can be simulated well. Before, specialized approaches were chosen, which required considerably more manual work in setting the right boundary conditions and simplifications of the simulated geometry, but, nevertheless

did achieve reliable results with less computing power. J. V. Porto developed such a concept for the ICS in 2001 [Por01] and it was reanalyzed by J. Ketter in the scope of [SHE+18]. Since the simplified geometry required for semi-analytical treatment can also be simulated in COMSOL MULTIPHYSICS™, a comparison between the two is very useful as a cross check.
In the following a short introduction is presented to the semi-analytical treatment. It is a pointlike ion with charge q at position $\vec{r}'$ in the trap with all electrodes grounded considered. The total potential at the position $\vec{r}$ is then given by

$$\Phi_{\text{ion}}(\vec{r},\vec{r}') = \frac{q}{4\pi\epsilon_0} G(\vec{r},\vec{r}') \tag{6.6}$$

$$= \frac{q}{4\pi\epsilon_0}\left[\frac{1}{|\vec{r}-\vec{r}'|} + F(\vec{r},\vec{r}')\right] \quad , \tag{6.7}$$

where the first term describes the ion's COULOMB potential and the second term is due to the image charges. The resulting electric field at the position of the ion is then calculated as

$$\vec{E}_{\text{image}}(\vec{r}') = -\frac{q}{4\pi\epsilon_0} \boldsymbol{\nabla}_{\boldsymbol{r}}\ F(\boldsymbol{r},\boldsymbol{r}')|_{\boldsymbol{r}=\boldsymbol{r}'} \quad . \tag{6.8}$$

In the next step the condition that determines the contribution $F(\vec{r},\vec{r}')$ of the image charges to the total potential is used. Let Ω denote the conducting trap surfaces. Since these conducting surfaces remain equipotential surfaces even in the presence of the ion, the total potential on the trap surfaces must vanish: $\Phi_{\text{ion}}(\Omega,\vec{r}') = 0$. The contribution by the image charges must therefore compensate for the ion's COULOMB potential. Like any source-free electrostatic potential, the potential produced by the image charges fulfills the LAPLACE equation $\Delta_{\boldsymbol{r}} F(\vec{r},\vec{r}') = 0$ inside the trap electrodes, where there are no image charges. The most general solution without singularities is given in terms of associated Legendre polynomials P_l^m by

$$F(\vec{r},\vec{r}') = \frac{1}{d}\sum_{l=0}^{\infty}\left(\frac{r}{d}\right)^l \sum_{m=0}^{l} P_l^m(\cos\theta)\cdot\left[C_l^m(\vec{r}')\cos(m\phi) + S_l^m(\vec{r}')\sin(m\phi)\right] \quad , \tag{6.9}$$

where $C_l^m(\vec{r}')$ and $S_l^m(\vec{r}')$ are dimensionless coefficients. These depend on the position $\vec{r}'$ of the ion. The goal is to choose the coefficients $C_l^m(\vec{r}')$ and $S_l^m(\vec{r}')$ such that the expression

$$\int_{\Omega} [G(\vec{r},\vec{r}')]^2 \, \mathrm{d}\Omega \tag{6.10}$$

is minimized. This concept is similar to the well-known least-square fit algorithm and to the FEM (see Section 3.1.1). For most geometries this integral needs to be calculated numerically. Therefore, this method is referred as semi-analytical. The ICS is calculated afterwards based on the coefficient $C_l^m(\vec{r}')$ and $S_l^m(\vec{r}')$ (see Equations (6.8) and (6.9)), which minimize the integral (see Equation (6.10)). A more detailed explanation can be found in [SHE+18].

Table 6.3.: Comparison of the numerical simulations, semi-analytical calculations and measurements of the ICS for three different high-precision PENNING-trap experiments and three different approaches: (1) Semi-analytical calculation with simplified geometry, denoted as (Porto); (2) Numerical calculation with simplified geometry, denoted as (COMSOL-Porto). (3) Numerical calculation with full geometry, denoted as (COMSOL-full). Uncertainties for the LFGs and the free space cyclotron frequency shift in the scenario (COMSOL-full) are separately listed: $()_{\text{sim}}$ and $()_{\text{geo}}$. The LFG $\mathcal{E}$ is given in $\mu V/m^2$ and $\Delta\nu_c$ is given in $\mu Hz/n$.

properties	FSU-TRAP	THE-TRAP	LIONTRAP
$\mathcal{E}_\rho$(Porto)	2 818.69(15)	42 458(13)	11 551(2)
$\mathcal{E}_\rho$(COMSOL-Porto)	2 816.8(1.6)	42 405(37)	11 545(49)
$\mathcal{E}_\rho$(COMSOL-full)	2 839.7(1.6)(11.5)	42 604(37)(366)	11 230.0(48.5)(84.0)
$\mathcal{E}_z$(Porto)	4 200.14(2.0)	80 793(25)	0.00(1.53)
$\mathcal{E}_z$(COMSOL-Porto)	4 198.8(2.1)	80 719(69)	0(2)
$\mathcal{E}_z$(COMSOL-full)	4 225.7(2.5)(21.3)	79 726(69)(1322)	8.1(3.1)(2.2)
$\Delta\nu_c$(Porto)	91.7850(34)	2 229.37(49)	488.416(58)
$\Delta\nu_c$(COMSOL-Porto)	91.738(36)	2 225.1(1.4)	488.7(2.1)
$\Delta\nu_c$(COMSOL-full)	92.416(37)(292)	2 218.8(1.4)(20.3)	475.4(2.1)(3.6)
$\Delta\nu_c$(measurements)	–	2 230(90) [vDPVLZ06]	471.9(23.9) [SHE+18]

6.5. Results

In this section the results of the finite element simulation of the ICS are compared with the semi-analytical treatment and the most precise measurement of the ICS so far. All results are listed in Table 6.3. For the three geometries the LFGs $\mathcal{E}_\rho$, $\mathcal{E}_z$ and the final shift in the free space cyclotron frequency (see Equation (2.8)) have been calculated in three different ways:

1. Semi-analytical calculations based on the approach by J. V. Porto and therefore denoted as "Porto". This approach requires some geometric simplifications, which by way of example, are shown at the FSU-TRAP. It is called PORTO-TRAP (see Figure 6.3) after simplification. The other two traps are changed in a similar way but not shown explicitly.

2. In order to compare the numerical simulations with the semi-analytical predictions also ICS of the simplified geometries has been calculated in COMSOL MULTIPHYSICS™ denoted as "COMSOL-Porto". This serves as a cross check.

3. The complete geometries without simplifications have been simulated in COMSOL MULTIPHYSICS™ for the final determination of the ICS, entitled as "COMSOL-full".

The relative deviation of less than 0.2% between the semi-analytical and numerical simulations using FEM prove that both methods work very well. The difference of 2.7(4)% between the simplified "COMSOL-Porto" and the real model "COMSOL-full" in the LIONTRAP case illustrates the importance of taking geometric subtleties into account. In additional tests it could be shown that inserting horizontal slits into the trap electrodes shifts the result down by 2.2(4)%. The

consideration of azimuthal slits in the C_1 electrodes and the ring electrode shifts it downwards again by 0.5(4)%.
Further improvements are not limited by the available computational power. The largest uncertainty in the finite element approach comes from the manufacturing tolerances. The FEM simulation has a total uncertainty of 1 %, which is a factor of four better than the best measurement so far.
A more elaborate measurement than the multiple ion approach could determine the ICS better. Until now, Robert van Dyck Jr.'s measurement of the ICS is the most accurate [vDPVLZ06]. The finite element simulation can confirm Robert van Dyck Jr.'s measured value for the ICS (see Table 6.3). As already mentioned in the introduction, the measurement is based on the observation of the frequency shift as a function of the number of ions in the trap. This measurement has the problem that the ion-ion interaction is difficult to compensate which results in a systematic uncertainty and limits its precision. Recently a new measurement method developed by Sven Sturm was published in Schuh *et al.* [SHE+18] and gave the experimental ICS value for the LIONTRAP shown in Table 6.3. It reaches the same precision as the measurement by Robert Van Dyck Jr. The ICS measurement for the LIONTRAP experiment confirms the prediction by the simulation. As it agrees with both the old method by Robert van Dyck Jr. and by Sven Sturm, the simulation serves as an excellent cross check and proves its predictive power.

7. Ion buncher at IGISOL

The original IGISOL RFQ cooler / buncher provides ion bunches with a time spread of about 10 µs (see Section 4.1.1) since the year 2000. The need for shorter ion pulses became apparent with the development of the MR-ToF MS concept 10 years later. The MR-ToF MS has proven itself in many experiments (see references in Section 2.4) and for IGISOL it is planned to install one, too. For the Jyväskylä MR-ToF MS, the design goal for the full width at half maximum (FWHM) of the ion pulses was set to 100 ns or less, while the energy spread should remain below 40 eV in order to be able to use the full capability of an MR-ToF MS. In general the MR-ToF MS works better the shorter the pulses are, but decreasing the temporal width usually increases the energy spread. The values of 100 ns and 40 eV are based on experience.
The following Section 7.1 shows the development of a new ion buncher using the simulation tool SIMION, which got briefly introduced in Section 3.1.3. In the next section the first results of the experimental implementation of the new design are presented.

7.1. Simulations

This section presents the development of the new ion bunching section of the JYFL RFQ using the simulation tool SIMION. First, the RFQ cooler / buncher is simulated as it was originally installed (see Section 4.1.1). This is done in order to calibrate the simulations, especially for the buffer gas pressure in the different sections since it strongly affects the ion cooling. The results can be found in Section 7.1.1 As soon as the simulated distribution of the time of flight and the ion energy, as well as the transmission efficiency matches the experimental data, the process of finding a new design was started. The final result of this development process is presented in Section 7.1.2.

7.1.1. Characterization of the existing setup

The existing setup is simulated first as the starting point for the SIMION simulations. This is to ensure that the simulation works reliably and is in agreement with experimental data. The original RFQ cooler / buncher is already available as a CAD-model that matches Figure 4.2. This model can be imported directly into SIMION and the geometry is meshed with a mesh size (see Section 3.1) of 0.2 mm. As mentioned in Section 3.1.3, SIMION uses only cubes with constant size to build the mesh. A smaller mesh would have lead to a memory overflow of the computing cluster. A screenshot of the imported geometry can be found in Figure 7.1a. The setup is reduced to the parts essential for the simulation. The last four elements of the RF quadrupole segments, the end plate, the miniature quadrupole rods, the extraction plate and the extraction electrode are included in the simulation geometry (see Figure 7.1a). This figure shows the geometry that was used in the simulation of the original RFQ. The used voltage configuration can be

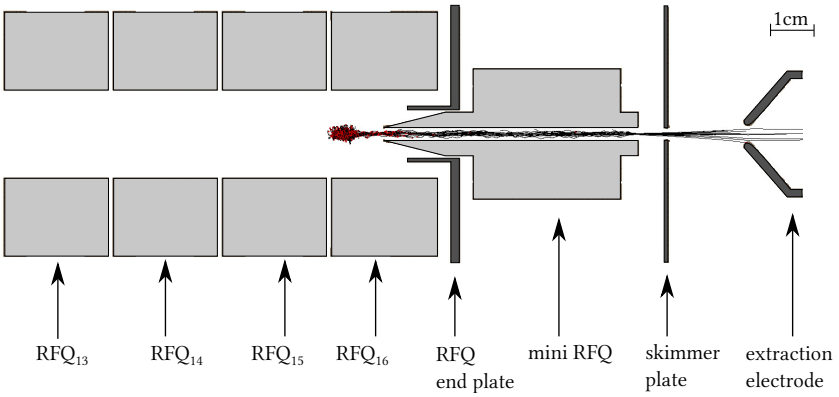

(a) Simulation of the original IGISOL RFQ cooler buncher. The original image can be seen in Figure 4.2 and is also available as a CAD model. The CAD model was simplified to contain only the parts that are relevant for the simulation.

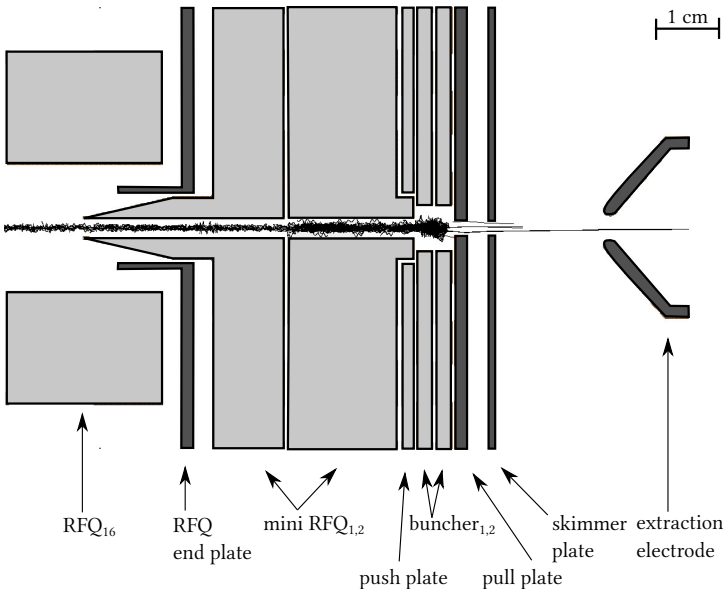

(b) Modified RFQ with bunching section. Compared to figure (a), the mini RFQ was shortened by 3.55 mm and segmented into two. A bunching section with 2 x 4 pairs of electrodes is added. Additionally there is a pull and push plate to move the ions within the bunching section.

Figure 7.1.: Modified screenshots of the SIMION simulation of the original RFQ cooler / buncher (a) and the modified version with the new bunching section (b). The dark grey electrodes are cylindrically symmetric and the light grey electrodes are quadrupolar electrodes. The applied voltages can be seen in Table 7.1 in the column "Init" for figure (a) and in the column "Final" for figure (b). The corresponding buffer gas pressures are given in Table 7.2. The black lines represent the trajectories of the ions. The red dots are collisions with the buffer gas. In figure (b) there are significantly fewer collisions because the ions are not stored in the main RFQ. The results of simulations with these geometries can be found in Figure 7.2 and in Table 7.3.

Table 7.1.: Voltage settings for the SIMION simulations. The voltage settings for the initial geometry (see Figure 7.1a) is given in the columns "init". Correspondingly the voltage settings for the final buncher geometry (see Figure 7.1b) is presented in the columns "final". The buffer gas pressure settings are shown in Table 7.2. All settings are used for accumulating ions. The changes for the ejection are the values behind the forward slash. More information is given in the text.

electrode	init			final		
	DC (V)	AC (V)	frequency (kHz)	DC (V)	AC (V)	frequency (kHz)
RFQ_{13}	4.6	200	600	2.4	244	600
RFQ_{14}	4.2	200	600	2.2	244	600
RFQ_{15}	4.0	200	600	2.0	244	600
RFQ_{16}	0	200	600	1.0	244	600
RFQ end plate	50/0	-	-	0.5	-	-
mini RFQ	-1.5	2.5	600	-	-	-
mini RFQ_1	-	-	-	0.0	4.2	600
mini RFQ_2	-	-	-	-0.5	4.2	600
push plate	-	-	-	-2/500	-	-
$buncher_1$	-	-	-	-2.5	30	600
$buncher_2$	-	-	-	-5.7	30	600
pull plate	-	-	-	2/-25	-	-
skimmer plate	-134	-	-	-200	-	-
skimmer	-300	-	-	-500	-	-

seen in Table 7.1 and the buffer gas pressures used for each section are given in Table 7.2. The concept of buffer gas cooling is already introduced in Section 2.3.2. The gas pressures in the simulation are one order of magnitude less than in Reference [NHJ+01], because otherwise the time-of-flight (ToF) distribution (see Figure 7.2a) would not match the experimental values at all. The lower pressure in the simulation is not assumed to be a problem, because the pressure read out in the experiment, which gives the pressure values in Reference [NHJ+01], is outside of the RFQ cooler / buncher and therefore, it is hard to estimate the real pressure in the path of the ions inside the device. Also, the simulation model for the buffer gas cooling may overestimate the efficiency of the cooling process. The model to implement the buffer gas cooling in the simulation is based on the Reference [LH97] and the only one available for SIMION. To speed up simulations, the ions are created near the end of the main RFQ structure (marked RFQ_{16} in Figure 7.1a) to avoid simulating the ion's path through the whole RFQ. To simulate a realistic case, singly charged mass 100 u ions are used, which have an average kinetic energy of 0.1 eV, a velocity pointing towards the skimmer and an energy spread of 0.01 eV. These values are chosen because it is not the actual cooling process of the RFQ cooler / buncher that is to be analyzed, but the behavior during ejection of the ions. There is a slight DC gradient on the three RFQ elements with a decreasing potential towards the RFQ end plate (see Table 7.1), that is kept at positive +50 V potential so the ions are first stored in the last element of the RFQ.

Table 7.2.: Buffer gas pressure settings for the SIMION simulations. The setting for the initial geometry (see Figure 7.1a) can be found in the second column. The setting for the final geometry (see Figure 7.1b) can be found in the third column. The areas correspond to the electrodes, which are named in the given figures.

area	initial simulation (10^{-3} mbar)	final simulation (10^{-3} mbar)
main RFQ	10	42
mini RFQ	0.6	2.5
new buncher	-	2.5
behind the skimmer plate	0.00001	0.00001

Table 7.3.: Characteristic parameters of the RFQ cooler / buncher. Values marked with $_{\text{sim.}}$ are determined using a SIMION simulation. Values with $_{\text{meas.}}$ are measured experimentally. The experimental values for the original RFQ cooler / buncher are taken from Reference [NHJ+01]. For all values except original$_{\text{meas.}}$ the corresponding distributions can be found in Figure 7.2.

version	FWHM ToF dist. (ns)	FWHM energy dist. (eV)	transmission efficiency (%)
original$_{\text{sim.}}$	10494 ± 321	0.796 ± 0.018	77
original$_{\text{meas.}}$	11000	< 1	60
modified$_{\text{sim.}}$	53.4 ± 0.3	9.617 ± 0.09	72
modified$_{\text{meas.}}$	441 ± 11	10.57 ± 0.69	30

After a storage time of 250 µs the endplate is switched to 0 V so that the ions exit towards the mini RFQ. Figure 7.2a shows the ToF and the energy spectrum. The ToF and energy spectrum can be seen in Figure 7.2a. Table 7.3 contains the results of the fits of the distributions in the row original$_{sim.}$. The simulation agrees well with the measurement results, especially since the performance of the RFQ cooler / buncher was optimized further over time and is even closer to the results of the simulation than in the publication of Nieminen *et al.* from 2001 [NHJ+01]. The used voltage settings are also similar to the experimental values. The strong tail in the ToF spectrum comes from the interaction of the ions with the buffer gas and is also evident in the measurement results. If the buffer gas is removed, the tail also disappears. For fitting the data first a Gaussian was used, but the tail made a modification necessary. The final results are achieved by fitting a combination of a Gaussian for the main distribution and an exponential decay for the tail. The possible error due to the changed fit function can be neglected, since the simulations carried out here are generally used for the rough determination of the FWHM.

7.1.2. Final geometry and performance

Starting from the original RFQ cooler / buncher simulations, more than 100 different geometries were tried. The final simulation was performed in close cooperation with the PostDoc in charge for the buncher modification Dr. Antoine de Roubin. The new geometry can be seen

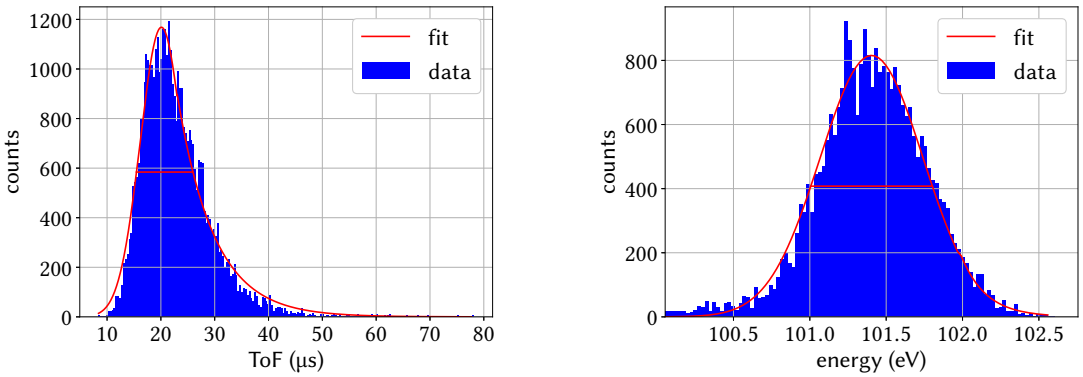

(a) Simulation results of the original RFQ cooler / buncher (see Figure 7.1a).

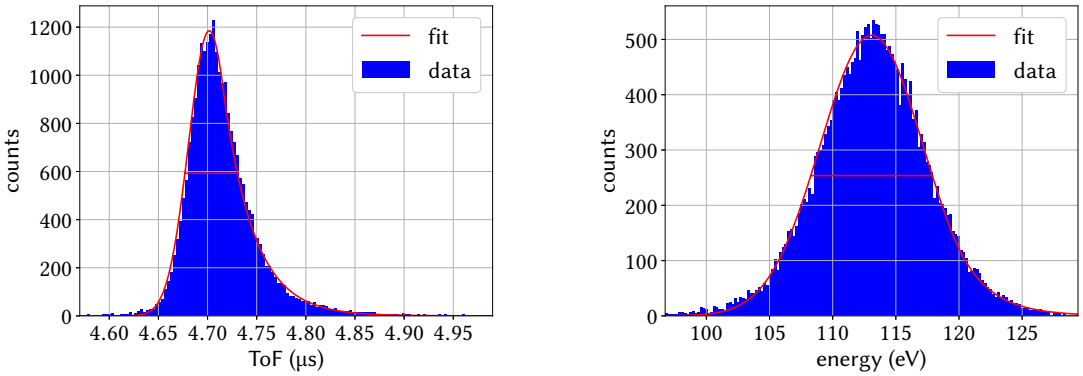

(b) Simulation results of the new bunching section (see Figure 7.1b).

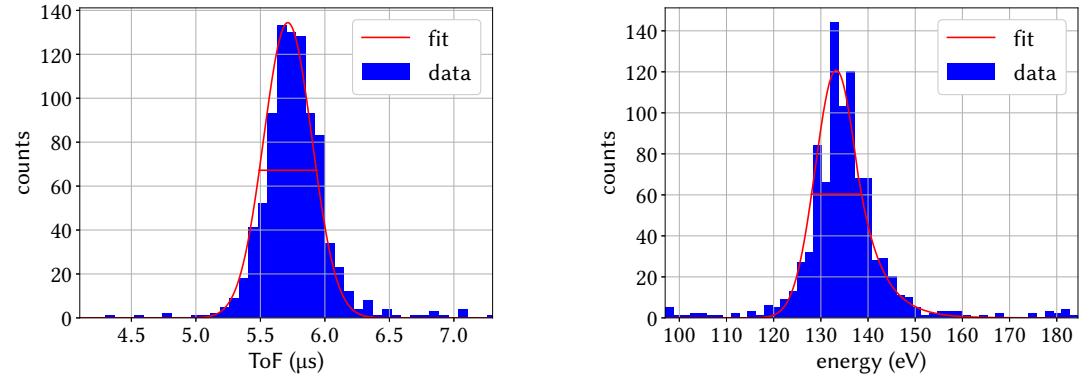

(c) Measurement result of the new bunching section (see Figure 7.4).

Figure 7.2.: Results of the simulations and measurements described in Section 7.1.1, 7.1.2 and 7.2 are displayed in (a), (b) and (c), respectively. On the left side the time-of-flight (ToF) distribution and on the right side the energy distribution of the ions can be found. The curves are fitted with a combination of a Gauss function and an exponential tail. The tail results from the interaction of the ions with the buffer gas. The red horizontal line describes the position and width of the FWHM. The values of the FWHM are given in Table 7.3. The absolute values of the x-axis of the ToF and the energy spectrum are irrelevant and arbitrary as only the FWHM is of interest.

in Figure 7.1b. The mini RFQ is shortened from 58.4 mm to 54.85 mm at the end towards the skimmer to generate space for the new bunching region. In addition, the mini RFQ is longitudinally divided into two parts to create a DC gradient. This should allow the ions to reach the new bunching section more efficiently. The rods of the new bunching section are 2.5 mm long. All electrodes have a gap of 0.5 mm between each other except to the skimmer plate, where it is more. The exact distance is unknown due to manufacturing reasons. The r_0 (see Figure 2.4) in the new bunching section is 3.65 mm, while it is 1.5 mm in the mini RFQ and 10 mm in the RFQ. In addition, a push and a pull plate was added to allow fast extraction of ions from the new bunching region. While in Figure 7.1b it seems that the push plate cannot be seen from the ions in the bunching section, this electrode is a quadrupole electrode, which is rotated by 45° with respect to the mini RFQ_2 electrode. As a result of the modifications, the ions do not gather in the main RFQ but in the new ion buncher, which can be seen by the black lines indicating the ion flight path. The necessary voltages and buffer gas settings can be found again in Table 7.1 and Table 7.2, respectively.

The pressure settings between the two different simulations are significantly different, because it turned out that a higher pressure is needed in the mini RFQ and the new bunching section to accumulate the ions as shown in the final simulation. As already mentioned in Section 4.1.1, a higher pressure in the main RFQ does not influence the transmission efficiency significantly. It can be assumed that the rest of the apparatus stays at a very good vacuum, because the holes in the skimmer and pull plate have a diameter of 2.5 mm, which reduces the helium flow significantly.

After a few ms of storage the ions are extracted from the new bunching section. First, the push plate is switched from -2 V to +500 V. This presses the ions to the right. 50 ns later, the pull plate is switched from +2 to -25 V to eject the ions. The result can be seen in Figure 7.2b and in row "$\text{modified}_{\text{sim.}}$" of Table 7.3. The simulation shows that the ions indeed have a much smaller temporal width. The goal of a pulse width of less than 100 ns with a simultaneous energy spread of less than 40 eV is achieved. The correlation of the ions' kinetic energy and time of flight can be seen in Figure 7.3. The position for taking the data of this plot is as for the other simulations 10 cm further to the right than the extraction electrode shown in Figure 7.1a. It is evident from the plot that the ions are at this plane in their time-focus.

7.2. Implementation and experimental characterization

Based on the simulations described in the previous sections, a technical model was developed, which contains all necessary support structures to actually attach the modified mini RFQ and the new bunching section to the main RFQ. This CAD model can be seen in Figure 7.4a. A new mini RFQ and the bunching section were manufactured according to these specifications. In August 2018 the parts were assembled. The result can be seen in Figure 7.4b. Before optimizing the ion buncher settings for short ion pulses, it was tested in the shoot through mode. This means that the main and mini RFQ still cool the ions but the ions are not bunched neither in the main RFQ nor in the new bunching section. A transmission efficiency of 60 % could be achieved. Thus, the new ion buncher does not decrease the general performance of the whole system RFQ cooler / buncher, when it is used in the shoot through mode. This is important, because

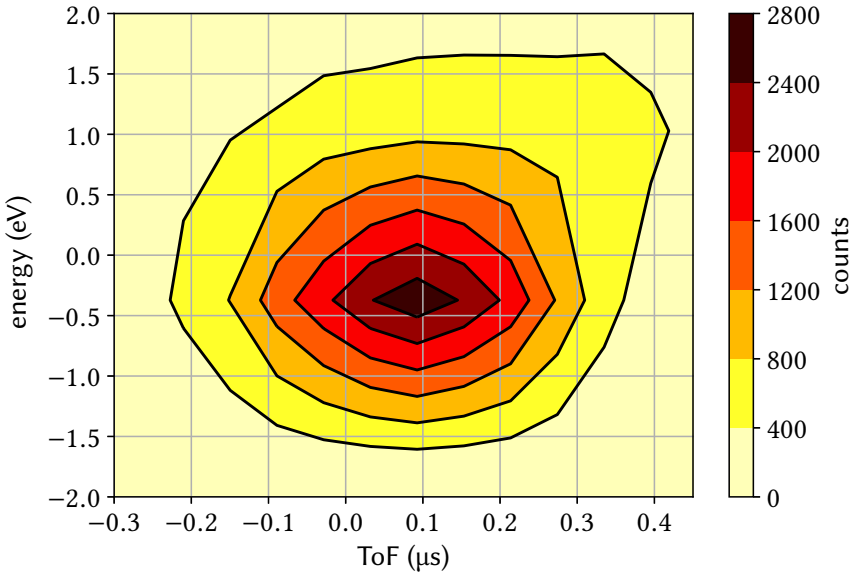

Figure 7.3.: Combined plot of the distributions shown in Figure 7.2b. Both distributions have been reduced by the average of their points.

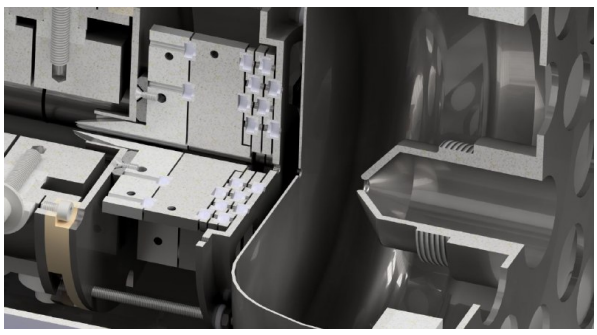

(a) CAD drawing of the new mini RFQ and ion buncher. On the left side of the picture the last electrode of the RFQ can be seen. It is followed by the longitudinally split new mini RFQ, the new bunching section including push and pull plate. At last the skimmer plate and the skimmer is shown.

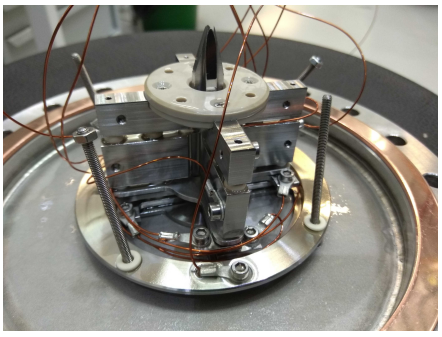

(b) The design shown in (a) can be seen in its realisation. The top of the mini RFQ, which points to the left in (a) points upwards here. In addition, the threaded rods as a holder and the wires for applying the voltages are shown.

Figure 7.4.: The finished design and realization of the new bunching section. In (a) the CAD model and in (b) a photo of the ion buncher can be seen.

some experiments at IGISOL will still use the RFQ cooler / buncher without the new bunching section.
The result of a short optimization of the new buncher during my stay in Jyväskylä can be see in Figure 7.2c and Table 7.3, respectively. The test was carried in cooperation with the IGISOL group and analysed by me. The FWHM is a factor of four larger than the design value. The energy spread is well below the assumed 40 eV maximum and the transmission efficiency dropped to 30 %. It was difficult to characterize the new bunching sections, because high-voltage sparks occurred once every few days. After a spark the settings of the buncher had to be readjusted, which took roughly a day. Due to this extra work the testing time had to be spent partly for other tasks than for the optimization of the buncher settings. Shortly after my departure from Jyväskylä a pulse with a temporal width of 100 ns could be achieved. The spectrum can be seen in Figure 7.5. The FWHM of 107 ns agrees almost with the target

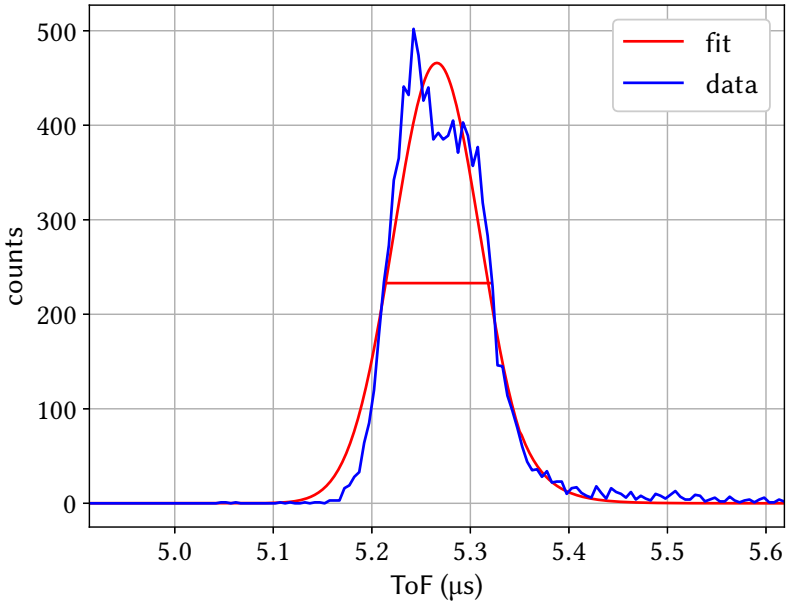

Figure 7.5.: Further improved bunch width with a FWHM of 107 ns ± 2 ns from September 2019.

of 100 ns but the distribution deviates clearly from a Gaussian distribution, because it is not symmetric and has a maximum at 5.24 µs while the center is at 5.27 µs. At the moment it is assumed that the ions are not accumulated long enough in the new bunching section, and they are just compressed by switching the pull and push plate, when the ions fly through. This could explain the peak at 5.24 µs, because the push plate kicks the slowest ions but there is no accumulation and releasing of the ions taking place which would lead to a Gaussian ToF distribution. An energy spectrum was not measured and the transmission efficiency dropped below 1 %, which is insufficient. Later performed tests even reached a FWHM of 50 ns but with the trade-off of an even lower transmission efficiency.

8. Conclusion and outlook

This thesis focused on the new development of a Python based control system for the THe-Trap experiment, on the numerical calculation of the image charge shift for precision Penning-trap experiments and on the development of an ion buncher for the IGISOL facility in Jyväskylä, Finland.

The migration from the old NI LabWindows™/CVI to the new Python based control system was successful. All functionalities of the old control system also have been implemented in the new one. The GUI works as a "State Display" and the user can see the status of the experiment at one glance. In addition, the script-based control of the experiment has become simpler and more powerful, because now Python based scripts can be directly used for performing measurements. The automatic documentation of the experiment settings during measurements became more accurate and reliable because it is directly implemented in the control software and manual interaction is not needed. Also, some PnP tests were performed with the control system. Unfortunately, there were experimental problems, so that although the control system had the possibility to apply the PnP method, it was never used for a measurement campaign. After the shutdown of THe-Trap parts of the control system can be used in the following and neighboring experiments. I will stay available for discussions and exchange of ideas after the end of my time at the Max-Planck-Institute for Nuclear Physics.

The approach to calculate the image charge shift (ICS) using the finite element method with the help of COMSOL multiphysics™ has been successful. The calculations are accurate to 1 % and confirm the old measurement method of Robert Van Dyck Jr., which was based on the frequency shift depending on the number of ions in the trap. At the same time, the predicted value from the simulation for the Liontrap-experiment was experimentally confirmed. Thus, the simulation shows its reliability and predictive power. For the future it is planned to simulate the ICS for other high-precision Penning-trap experiments, such as e.g. Pentatrap [RBD+12, RBCLU+12] or ALPHATRAP [SAE+19].

The results of the simulations are a factor four more accurate than all measurement results so far. It is likely that the new measurement method at Liontrap will be improved further, as it is mentioned in the outlook of Reference [SHE+18] and become more precise than the simulation. The greatest limitation in the simulation originates from the manufacturing tolerances. If it is possible to determine the trap diameter of cylindrical Penning traps better than the uncertainty of the manufacturing tolerances or to machine new Penning traps with a lower manufacturing tolerance, it will be possible to further improve the accuracy of the simulation as well.

At the last part of the thesis SIMION simulation studies of the original RFQ cooler / buncher at the experiment IGISOL have been carried out such that the time and energy spectrum match the experimental results. Afterwards the aim was to modify the mini RFQ section of the RFQ cooler / buncher so that an ion bunch with FWHM of less than 100 ns in the time domain and an energy spread below 40 eV can be created. One design could prove in the simulation that it can

produce ion bunches with the given requirements while employing experimentally accessible settings in voltages and buffer gas pressures. This design was then built, installed and tested. The first test showed that the ion buncher used in the shoot through mode does not influence the performance of the rest of the RFQ cooler / buncher, which is important as not all experiments will use the new buncher. When the new buncher is used, a short optimization could show a time spread of 400 ns and an energy spread of 10 eV for a reasonable transmission efficiency of 30 %. A bunch could be created with 107 ns and even better but there the transmission efficiency dropped by two orders of magnitude. These values are very promising for a first test and the aimed for 100 ns FWHM at a transmission efficiency of 30 % or better should be attainable soon. The parts for the new MR-ToF MS are currently being built. It will be very interesting to see how the ion buncher and the MR-ToF MS will work together in the future. In the meantime, it could be useful to simulate the gas pressures in the RFQ cooler / buncher using the molecular flow model of COMSOL MULTIPHYSICS™. As mentioned the gas pressure in the simulation is one order of magnitude smaller than the read-out at the experiment shows, otherwise the results of the simulation do not match those from the experiment. One reason could be that the pressure in the RFQ cooler / buncher is not distributed equally and inside of the RFQ elements the pressure is lower than at the read out. A simulation should be able to improve the knowledge on the gas pressures in the different sections, which can help to find the required gas pressure displayed at the read-out to be able to accumulate the ions in the bunching section. This could solve the problem that the transmission efficiency drops when the bunches become smaller in temporal width. Additionally, the model of the buffer gas cooling may overestimate the cooling effect. COMSOL MULTIPHYSICS™ is also able to simulate the buffer gas cooling and it would be a good idea to compare both simulations.

A. Control tabs

In the following the additional tabs of the THe-Controller (see Figure 5.2) are presented. The screenshots here have a slightly different color and font, because they are taken while the control system is running on a Linux computer. The main controller computer which is a Microsoft Windows 7 machine and was used for Figure 5.2 is not available anymore, because the experiment is shut down.

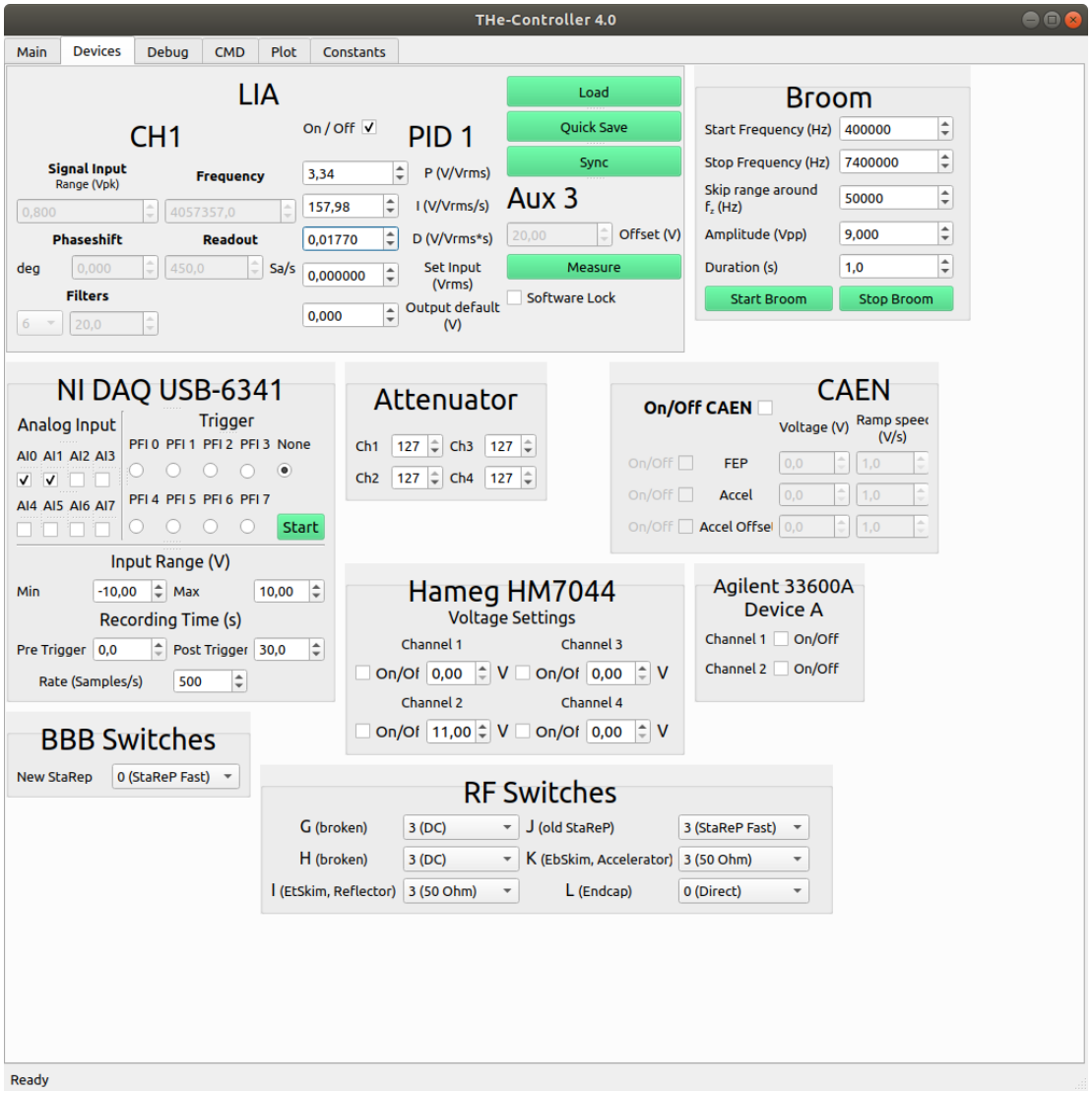

Figure A.1.: Gives control over and displays the status of devices that are not as frequently used as the devices in the main tab. The CAEN is grayed out, because it is switched off. This prevents that numbers are dialed in accidentally and when the CAEN starts the next time, a high voltage is applied unintentionally.

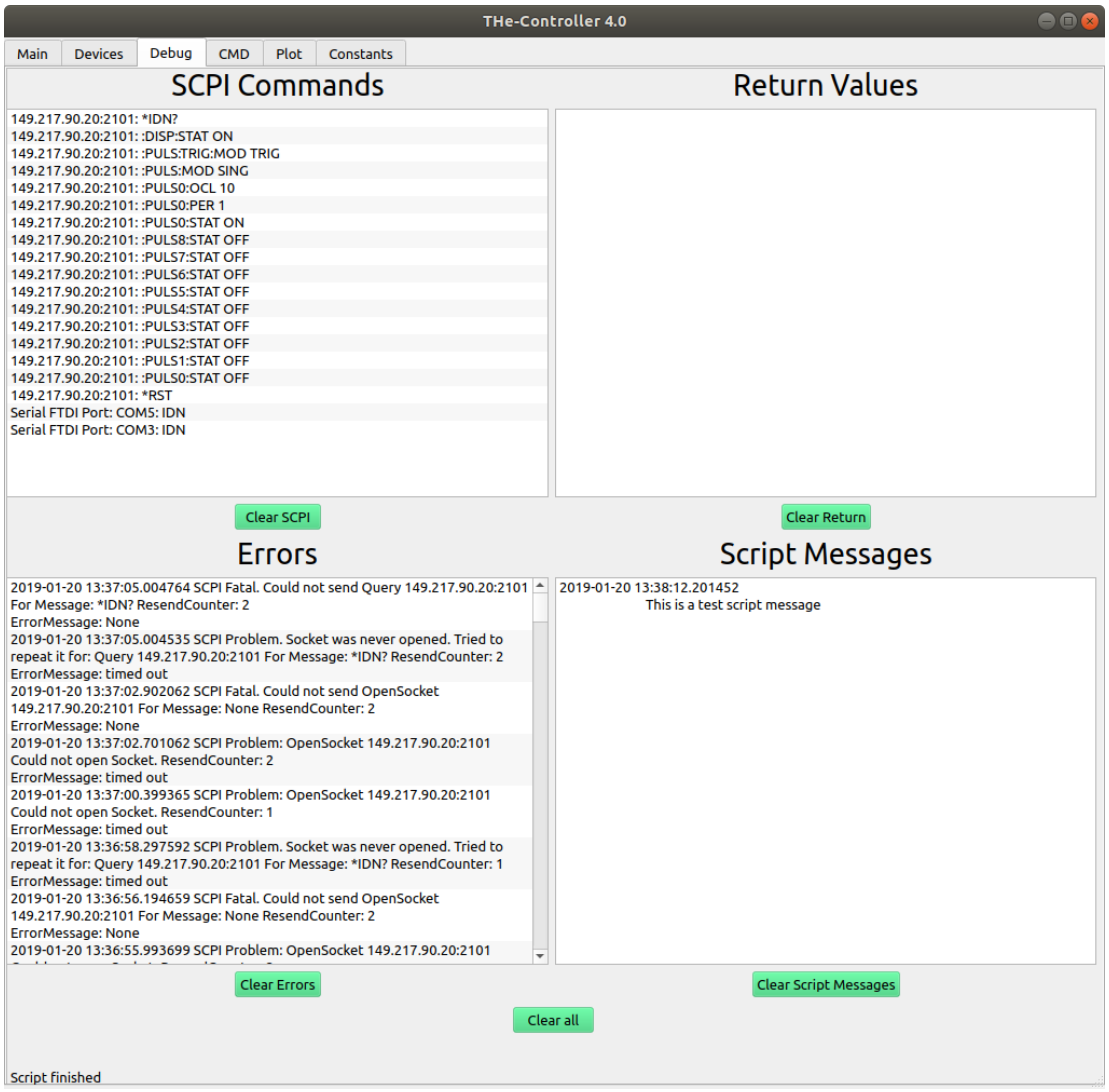

Figure A.2.: The control system is not running on the main experiment computer. Therefore, the SCPI commands displayed in the upper left do not get any return values that could be shown on the right. But the error messages in the lower left window indicate how errors are handled. The script message in the bottom right part is produced by a short test script.

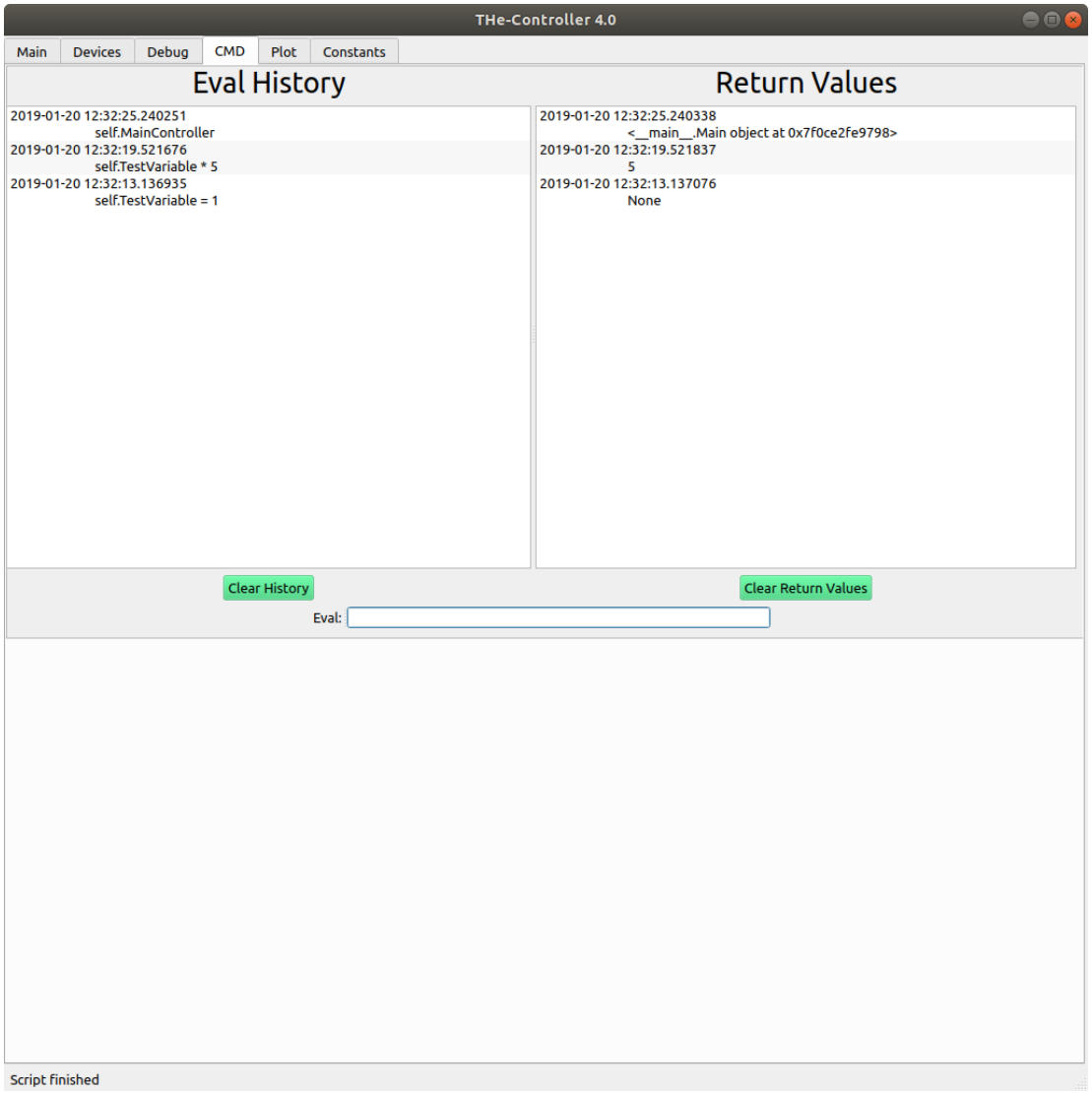

Figure A.3.: The text input line after "Eval:" offers to execute PYTHON commands directly within the framework of the control system. In the left window the procedure of defining a variable and using it later is shown. The return values are shown on the right. The variable "self.MainController" is the main variable which is forwarded to other classes for having access to the main frame of the control system. Due to this variable all other instances can be reached from this command line.

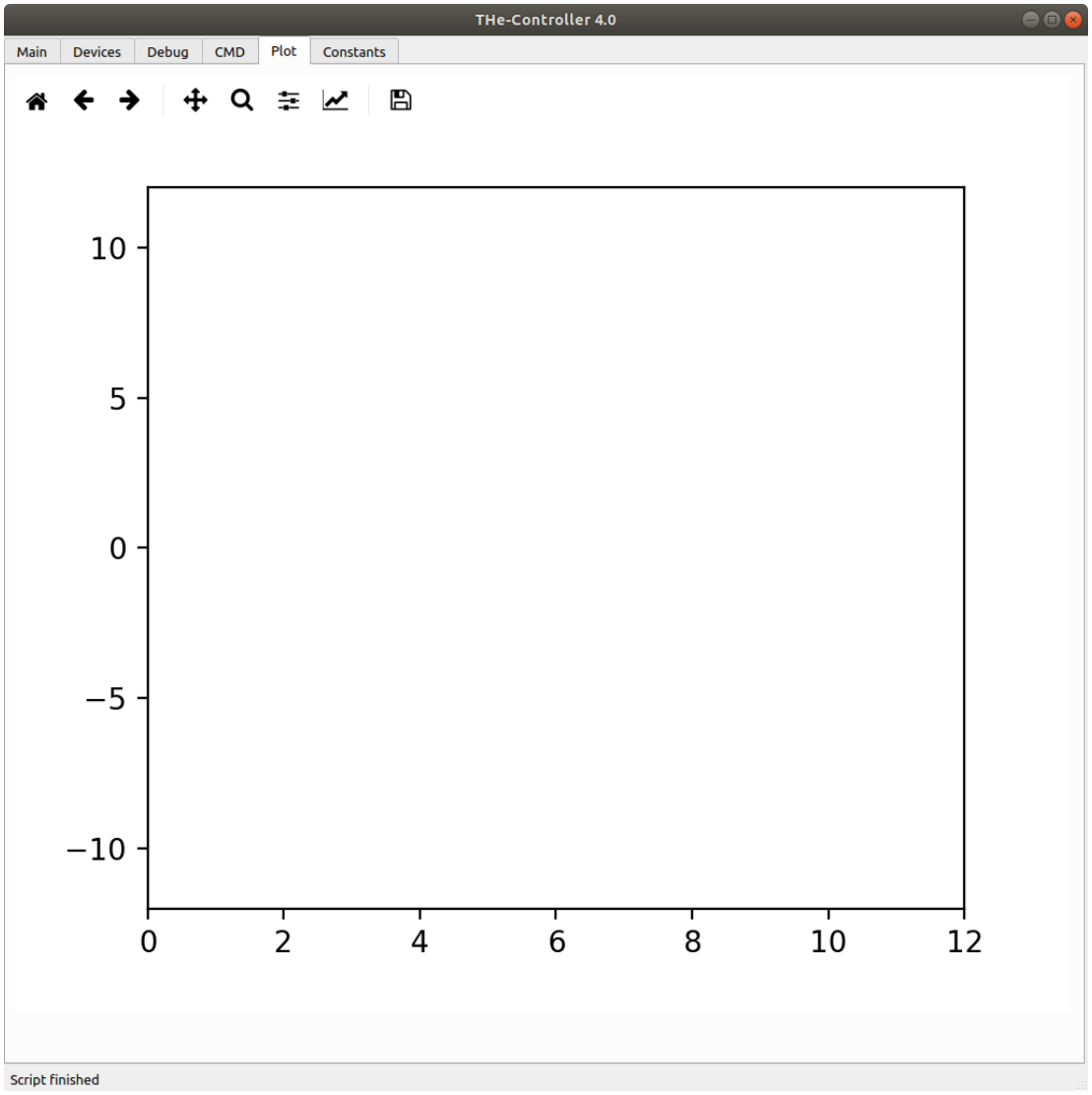

Figure A.4.: This window is made to show the result of the latest frequency sweep (see Figure 4.2.1). It was never used intensively because a website showing an overview of the latest sweeps was available.

Figure A.5.: Indicating if the initialization of the devices at the experiment was successful. Here it clearly was not successful, because the software is running on a computer which is not connected to any device. The devices shown here are supposed to be only very rarely changed.

Bibliography

[AGT07] M. Arnould, S. Goriely, and K. Takahashi. The r-process of stellar nucleosynthesis: Astrophysics and nuclear physics achievements and mysteries. *Physics Reports*, 450(4):97 – 213, 2007. (Cited on page 16.)

[ALB92] W.E. Austin, J.H. Leck, and J.H. Batey. Study of the performance of a group of quadrupole mass spectrometers. *Journal of Vacuum Science & Technology A*, 10(6):3563–3567, 1992. (Cited on page 25.)

[Ast20] F.W. Aston. Isotopes and atomic weights. *Nature*, 105:617–619, 1920. (Cited on page 13.)

[Ast37] F.W. Aston. A second-order focusing mass spectrograph and isotopic weights by the doublet method. *Proceedings of the Royal Society of London. Series A, Mathematical and physical sciences*, 163(A914):0391–0404, 1937. (Cited on page 13.)

[Ath71] M. Athans. On the design of p-i-d controllers using optimal linear regulator theory. *Automatica*, 7(5):643 – 647, 1971. (Cited on page 52.)

[Bar03] S.E. Barlow. Alternative electrostatic Green's function for a long tubeg. *Journal of Applied Physics*, 94(9):6221–6222, 2003. (Cited on page 73.)

[BBE+17] L. Bornschein, B. Bornschein, S. Ebenhöch, M. H., F. Priester, M. Röllig, M. Sturm, T. Thümmler, and KATRIN Collaboration. Status of the karlsruhe tritium neutrino mass experiment katrin. *Fusion Science and Technology*, 71(4):485–490, 2017. (Cited on page 15.)

[BG86] L.S. Brown and G. Gabrielse. Geonium theory: Physics of a single electron or ion in a Penning trap. *Review of Modern Physics*, 58:233–311, Jan 1986. (Cited on pages 19 and 21.)

[BGM+98] K. Blaum, C. Geppert, P. Müller, W. Nörtershäuser, E.W. Otten, A. Schmitt, N. Trautmann, K. Wendt, and B.A. Bushaw. Properties and performance of a quadrupole mass filter used for resonance ionization mass spectrometry. *International Journal of Mass Spectrometry*, 181(1):67 – 87, 1998. (Cited on pages 25, 28 and 29.)

[BGM+00] K. Blaum, C. Geppert, P. Müller, W. Nörtershäuser, K. Wendt, and B.A. Bushaw. Peak shape for a quadrupole mass spectrometer: comparison of computer simulation and experiment. *International Journal of Mass Spectrometry*, 202(1):81 – 89, 2000. (Cited on page 25.)

[BN36] N.E. Bradbury and R.A. Nielsen. Absolute values of the electron mobility in hydrogen. *Physical Review*, 49:388–393, Mar 1936. (Cited on page 30.)

[BNW10] K. Blaum, Y.N. Novikov, and G. Werth. Penning traps as a versatile tool for precise experiments in fundamental physics. *Contemporary Physics*, 51(2):149–175, 2010. (Cited on page 21.)

[BSB+12] T. Brunner, M.J. Smith, M. Brodeur, S. Ettenauer, A.T. Gallant, V.V. Simon, A. Chaudhuri, A. Lapierre, E. Mané, R. Ringle, M.C. Simon, J.A. Vaz, P. Delheij, M. Good, M.R. Pearson, and J. Dilling. TITAN's digital RFQ ion beam cooler and buncher, operation and performance. *Nuclear Instruments and Methods in Physics Research Section A: Accelerators, Spectrometers, Detectors and Associated Equipment*, 676:32 – 43, 2012. (Cited on page 29.)

[BT64] W.M. Brubaker and J. Tuul. Performance studies of quadrupole mass filter. *Review of Scientific Instruments*, 35(8):1007–&, 1964. (Cited on page 25.)

[C-S] ISO/IEC 9899. http://www.open-std.org/jtc1/sc22/wg14/www/standards. Accessed: 2018-11-14. (Cited on page 44.)

[CBB+09] F.C. Charlwood, K. Baczynska, J. Billowes, P. Campbell, B. Cheal, T. Eronen, D.H. Forest, A. Jokinen, T. Kessler, I.D. Moore, H. Penttilä, R. Powis, M. Rüffer, A. Saastamoinen, G. Tungate, and J. Äystö. Nuclear charge radii of molybdenum fission fragments. *Physics Letters B*, 674(1):23 – 27, 2009. (Cited on page 46.)

[CTB+02] P. Campbell, H.L. Thayer, J. Billowes, P. Dendooven, K.T. Flanagan, D.H. Forest, J.A. Griffith, J. Huikari, A. Jokinen, R. Moore, A. Nieminen, G. Tungate, S. Zemlyanoi, and J. Äystö. Laser spectroscopy of cooled zirconium fission fragments. *Physical Review Letters*, 89:082501, Aug 2002. (Cited on page 46.)

[CWB+89] E.A. Cornell, R.M. Weisskoff, K.R. Boyce, R.W. Flanagan, G.P. Lafyatis, and D.E. Pritchard. Single-ion cyclotron resonance measurement of $m(co^+)/m(n_2^+)$. *Physical Review Letters*, 63:1674–1677, Oct 1989. (Cited on page 14.)

[DF92] D.J. Douglas and J.B. French. Collisional focusing effects in radio frequency quadrupoles. *Journal of the American Society for Mass Spectrometry*, 3(4):398 – 408, 1992. (Cited on page 29.)

[Die11] Christoph Diehl. *First mass measurements with the MPIK/UW-PTMS*. PhD thesis, University of Heidelberg, 2011. (Cited on page 56.)

[Dou98] D.J. Douglas. Applications of collision dynamics in quadrupole mass spectrometry. *Journal of the American Society for Mass Spectrometry*, 9(2):101 – 113, 1998. (Cited on page 29.)

[DPB+15] T. Dickel, W.R. Plaß, A. Becker, U. Czok, H. Geissel, E. Haettner, C. Jesch, W. Kinsel, M. Petrick, C. Scheidenberger, A. Simon, and M.I. Yavor. A high-performance multiple-reflection time-of-flight mass spectrometer and isobar separator for the

research with exotic nuclei. *Nuclear Instruments and Methods in Physics Research Section A: Accelerators, Spectrometers, Detectors and Associated Equipment*, 777:172 – 188, 2015. (Cited on pages 19 and 29.)

[Ear42] S. Earnshaw. On the nature of the molecular forces which regulate the constitution of the luminiferous ether. *Transactions of the Cambridge Philosophical Society*, 7:97, 1842. (Cited on page 26.)

[Edd20] A.S. Eddington. The internal constitution of the stars. *Science*, 52:233–240, 1920. (Cited on page 13.)

[Els33] W.M. Elsasser. The pauli principle in nucleus. *Journal de Physique et le Radium*, 4:549–556, 1933. (Cited on page 13.)

[FHI+98] Y. Fukuda, T. Hayakawa, E. Ichihara, K. Inoue, K. Ishihara, H. Ishino, Y. Itow, T. Kajita, J. Kameda, S. Kasuga, K. Kobayashi, Y. Kobayashi, Y. Koshio, M. Miura, M. Nakahata, S. Nakayama, A. Okada, K. Okumura, N. Sakurai, M. Shiozawa, Y. Suzuki, Y. Takeuchi, Y. Totsuka, S. Yamada, M. Earl, A. Habig, E. Kearns, M.D. Messier, K. Scholberg, J.L. Stone, L.R. Sulak, C.W. Walter, M. Goldhaber, T. Barszczxak, D. Casper, W. Gajewski, P.G. Halverson, J. Hsu, W.R. Kropp, L.R. Price, F. Reines, M. Smy, H.W. Sobel, M.R. Vagins, K.S. Ganezer, W.E. Keig, R.W. Ellsworth, S. Tasaka, J.W. Flanagan, A. Kibayashi, J.G. Learned, S. Matsuno, V.J. Stenger, D. Takemori, T. Ishii, J. Kanzaki, T. Kobayashi, S. Mine, K. Nakamura, K. Nishikawa, Y. Oyama, A. Sakai, M. Sakuda, O. Sasaki, S. Echigo, M. Kohama, A.T. Suzuki, T.J. Haines, E. Blaufuss, B.K. Kim, R. Sanford, R. Svoboda, M.L. Chen, Z. Conner, J.A. Goodman, G.W. Sullivan, J. Hill, C.K. Jung, K. Martens, C. Mauger, C. McGrew, E. Sharkey, B. Viren, C. Yanagisawa, W. Doki, K. Miyano, H. Okazawa, C. Saji, M. Takahata, Y. Nagashima, M. Takita, T. Yamaguchi, M. Yoshida, S.B. Kim, M. Etoh, K. Fujita, A. Hasegawa, T. Hasegawa, S. Hatakeyama, T. Iwamoto, M. Koga, T. Maruyama, H. Ogawa, J. Shirai, A. Suzuki, F. Tsushima, M. Koshiba, M. Nemoto, K. Nishijima, T. Futagami, Y. Hayato, Y. Kanaya, K. Kaneyuki, Y. Watanabe, D. Kielczewska, R.A. Doyle, J.S. George, A.L. Stachyra, L.L. Wai, R.J. Wilkes, and K.K. Young. Evidence for oscillation of atmospheric neutrinos. *Physical Review Letters*, 81:1562–1567, Aug 1998. (Cited on page 15.)

[Gab84] G. Gabrielse. Detection, damping, and translating the center of the axial oscillation of a charged particle in a Penning trap with hyperbolic electrodes. *Physical Review A*, 29(2):462–469, Feb 1984. (Cited on page 23.)

[GAT+16] V. Guadilla, A. Algora, J.L. Tain, J. Agramunt, J. Äystö, J.A. Briz, D. Cano-Ott, A. Cucoanes, T. Eronen, M. Estienne, M. Fallot, L.M. Fraile, E. Ganioglu, W. Gelletly, D. Gorelov, J. Hakala, A. Jokinen, D. Jordan, A. Kankainen, V. Kolhinen, J. Koponen, M. Lebois, T. Martinez, M. Monserrate, A. Montaner-Pizá, I. Moore, E. Nácher, S. Orrigo, H. Penttilä, Zs. Podolyak, I. Pohjalainen, A. Porta, P. Regan, J. Reinikainen, M. Reponen, S. Rinta-Antila, B. Rubio, K. Rytkönen, T. Shiba, V. Sonnenschein, A.A. Sonzogni, E. Valencia, V. Vedia, A. Voss, J.N. Wilson, and

A.-A. Zakari-Issoufou. First experiment with the NUSTAR/FAIR Decay Total Absorption γ-ray Spectrometer (dtas) at the IGISOL IV facility. *Nuclear Instruments and Methods in Physics Research Section B: Beam Interactions with Materials and Atoms*, 376:334 – 337, 2016. Proceedings of the XVIIth International Conference on Electromagnetic Isotope Separators and Related Topics (EMIS2015), Grand Rapids, MI, U.S.A., 11-15 May 2015. (Cited on page 46.)

[Gho95] P.K. Ghosh. *Ion Traps*. Oxford University Press, 1995. (Cited on page 27.)

[GPQ+95] G. Gabrielse, D. Phillips, W. Quint, H. Kalinowsky, G. Rouleau, and W. Jhe. Special relativity and the single antiproton: Fortyfold improved comparison of $\bar{p}$ and p charge-to-mass ratios. *Physical Review Letters*, 74(18):3544–3547, May 1995. (Cited on page 14.)

[Häf00] Hartmut Häffner. *Präzisionsmessung des magnetischen Moments des Elektrons in wasserstoffähnlichem Kohlenstoff*. PhD thesis, Universität Mainz, 2000. (Cited on page 67.)

[HBD+03] H. Häffner, T. Beier, S. Djekić, N. Hermanspahn, H.-J. Kluge, W. Quint, S. Stahl, J. Verdú, T. Valenzuela, and G. Werth. Double Penning trap technique for precise g-factor determinations in highly charged ions. *The European Physical Journal D - Atomic, Molecular, Optical and Plasma Physics*, 22(2):163–182, Feb 2003. (Cited on page 25.)

[HBH+00] H. Häffner, T. Beier, N. Hermanspahn, H.-J. Kluge, W. Quint, S. Stahl, J. Verdú, and G. Werth. High-accuracy measurement of the magnetic moment anomaly of the electron bound in hydrogenlike carbon. *Physical Review Letters*, 85:5308–5311, Dec 2000. (Cited on page 15.)

[HDJ+04] J. Huikari, P. Dendooven, A. Jokinen, A. Nieminen, H. Penttilä, K. Peräjärvi, A. Popov, S. Rinta-Antila, and J. Äystö. Production of neutron deficient rare isotope beams at igisol; on-line and off-line studies. *Nuclear Instruments and Methods in Physics Research Section B: Beam Interactions with Materials and Atoms*, 222(3):632 – 652, 2004. (Cited on page 46.)

[Her03] F. Herfurth. Segmented linear RFQ traps for nuclear physics. *Nuclear Instruments and Methods in Physics Research Section B: Beam Interactions with Materials and Atoms*, 204:587 – 591, 2003. 14th International Conference on Electromagnetic Isotope Separators and Techniques Related to their Applications. (Cited on pages 19 and 29.)

[HKLR+17] F. Heiße, F. Köhler-Langes, S. Rau, J. Hou, S. Junck, A. Kracke, A. Mooser, W. Quint, S. Ulmer, G. Werth, K. Blaum, and S. Sturm. High-precision measurement of the proton's atomic mass. *Physical Review Letters*, 119:033001, Jul 2017. (Cited on pages 17 and 21.)

[Hua19] W. Huang. personal communication, February 2019. (Cited on page 14.)

[Hö16] Martin Jürgen Höcker. *Precision Mass Measurements at THe-Trap and the FSU trap*. PhD thesis, University of Heidelberg, 2016. (Cited on pages 52, 53, 54, 55 and 57.)

[ISW+13] Y. Ito, P. Schury, M. Wada, S. Naimi, T. Sonoda, H. Mita, F. Arai, A. Takamine, K. Okada, A. Ozawa, and H. Wollnik. Single-reference high-precision mass measurement with a multireflection time-of-flight mass spectrograph. *Phys. Rev. C*, 88:011306, Jul 2013. (Cited on page 31.)

[JEH+06] A. Jokinen, T. Eronen, U. Hager, I. Moore, H. Penttilä, S. Rinta-Antila, and J. Äystö. Precision experiments on exotic nuclei at igisol. *International Journal of Mass Spectrometry*, 251(2):204 – 211, 2006. Ultra-accurate mass spectrometry and related topics dedicated to H.-J. Kluge on the occasion of his 65th birthday anniversary. (Cited on page 46.)

[JLMP03] A. Jokinen, M. Lindroos, E. Molin, and M. Petersson. RFQ-cooler for low-energy radioactive ions at isolde. *Nuclear Instruments and Methods in Physics Research Section B: Beam Interactions with Materials and Atoms*, 204:86 – 89, 2003. 14th International Conference on Electromagnetic Isotope Separators and Techniques Related to their Applications. (Cited on page 29.)

[KEE+07] J. Kurpeta, V. V. Elomaa, T. Eronen, J. Hakala, A. Jokinen, P. Karvonen, I. Moore, H. Penttilä, A. Płochocki, S. Rahaman, S. Rinta-Antila, J. Rissanen, J. Ronkainen, A. Saastamoinen, T. Sonoda, W. Urban, Ch. Weber, and J. Äystö. Penning trap assisted decay spectroscopy of neutron-rich 115ru. *The European Physical Journal A*, 31(3):263–266, Mar 2007. (Cited on page 46.)

[KEG+13] V.S. Kolhinen, T. Eronen, D. Gorelov, J. Hakala, A. Jokinen, K. Jokiranta, A. Kankainen, M. Koikkalainen, J. Koponen, H. Kulmala, M. Lantz, A. Mattera, I.D. Moore, H. Penttilä, T. Pikkarainen, I. Pohjlainen, M. Reponen, S. Rinta-Antila, J. Rissanen, C. Rodríguez Triguero, K. Rytkönen, A. Saastamoinen, A. Solders, V. Sonnenschein, and J. Äystö. Recommissioning of jyfltrap at the new igisol-4 facility. *Nuclear Instruments and Methods in Physics Research Section B: Beam Interactions with Materials and Atoms*, 317:506 – 509, 2013. XVIth International Conference on ElectroMagnetic Isotope Separators and Techniques Related to their Applications, December 2–7, 2012 at Matsue, Japan. (Cited on page 46.)

[KEH+14a] J. Ketter, T. Eronen, M. Höcker, M. Schuh, S. Streubel, and K. Blaum. Classical calculation of relativistic frequency-shifts in an ideal Penning trap. *International Journal of Mass Spectrometry*, 361:34–40, March 2014. (Cited on page 22.)

[KEH+14b] J. Ketter, T. Eronen, M. Höcker, S. Streubel, and K. Blaum. First-order perturbative calculation of the frequency-shifts caused by static cylindrically-symmetric electric and magnetic imperfections of a Penning trap. *International Journal of Mass Spectrometry*, 358:1–16, January 2014. (Cited on pages 22 and 53.)

[Ket15] Jochen Ketter. *Theoretical treatment of miscellaneous frequency-shifts in Penning traps with classical perturbation theory*. PhD thesis, Ruprecht-Karls-Universität, Heidelberg, Germany, 2015. (Cited on page 23.)

[KKMV01] A. Kellerbauer, T. Kim, R.B. Moore, and P. Varfalvy. Buffer gas cooling of ion beams. *Nuclear Instruments and Methods in Physics Research Section A: Accelerators, Spectrometers, Detectors and Associated Equipment*, 469(2):276 – 285, 2001. (Cited on page 29.)

[KPT+73] R. Klapisch, R. Prieels, C. Thibault, A. M. Poskanzer, C. Rigaud, and E. Roeckl. On-line mass-spectrometric measurement of the masses of neutron-rich sodium isotopes. *Physical Review Letters*, 31:118–121, Jul 1973. (Cited on page 14.)

[KPU+18] J. Kurpeta, A. Płochocki, W. Urban, T. Eronen, A. Jokinen, A. Kankainen, V.S. Kolhinen, I.D. Moore, H. Penttilä, M. Pomorski, S. Rinta-Antila, T. Rząca-Urban, and J. Wiśniewski. Excited levels in the multishaped ^{117}Pd nucleus studied via β-decay of ^{117}Rh. *Physical Review C*, 98:024318, Aug 2018. (Cited on page 46.)

[Kö15] Florian Köhler. *Bound-Electron g-Factor Measurements for the Determination of the Electron Mass and Isotope Shifts in Highly Charged Ions*. PhD thesis, Ruprecht-Karls-Universität, Heidelberg, 2015. (Cited on page 71.)

[LBM92] M.D. Lunney, F. Buchinger, and R.B. Moore. The temperature of buffer-gas colled ions in a paul trap. *Journal of Modern Optics*, 39(2):349–360, 1992. (Cited on page 29.)

[LH97] D.M. Lubman and L. He. Simulation of external ion injection, cooling and extraction processes with simion 6.0 for the ion trap/reflectron time-of-flight mass spectrometer. *Rapid Communications in Mass Spectrometry*, 11(13):1467–1477, 1997. (Cited on pages 29 and 83.)

[LHL+03] M. Lugaro, F. Herwig, J.C. Lattanzio, R. Gallino, and O. Straniero. s-process nucleosynthesis in asymptotic giant branch stars: A test for stellar evolution. *The Astrophysical Journal*, 586(2):1305–1319, 2003. (Cited on page 16.)

[Mar02] R.C. Martin. *Agile Software Development, Principles, Patterns, and Practices*. Pearson, 1st edition, 2002. (Cited on page 58.)

[Max65] J.C. Maxwell. A dynamical theory of the electromagnetic field. *Philosophical Transactions*, 155:459–512, 1865. (Cited on page 33.)

[MD68] F.G. Major and H.G. Dehmelt. Exchange-collision technique for the rf spectroscopy of stored ions. *Physical Review*, 170:91–107, Jun 1968. (Cited on page 29.)

[MD86] P. Miller and M.B. Denton. The quadrupole mass filter: Basic operating concepts. *Journal of Chemical Education*, 63(7):617, 1986. (Cited on page 25.)

[MDA14] I.D. Moore, P. Dendooven, and J. Arje. The igisol technique - three decades of developments. *Hyperfine interactions*, 223(1-3):17–62, 2014. (Cited on pages 45 and 46.)

[MEG+13] I.D. Moore, T. Eronen, D. Gorelov, J. Hakala, A. Jokinen, A. Kankainen, V.S. Kolhinen, J. Koponen, H. Penttilä, I. Pohjalainen, M. Reponen, J. Rissanen, A. Saastamoinen, S. Rinta-Antila, V. Sonnenschein, and J. Äystö. Towards commissioning the new igisol-4 facility. *Nuclear Instruments and Methods in Physics Research Section B: Beam Interactions with Materials and Atoms*, 317:208 – 213, 2013. XVIth International Conference on ElectroMagnetic Isotope Separators and Techniques Related to their Applications, December 2–7, 2012 at Matsue, Japan. (Cited on page 45.)

[MH66] N.W. McLachlan and E. Hohn. Theory and application of mathieu functions. *Zeitschrift für angewandte Physik*, 22(1):51–&, 1966. (Cited on page 27.)

[MSMA16] M.R. Mumpower, R. Surman, G.C. McLaughlin, and A. Aprahamian. The impact of individual nuclear properties on r-process nucleosynthesis. *Progress in Particle and Nuclear Physics*, 86:86 – 126, 2016. (Cited on page 16.)

[Mye13] Edmund G. Myers. The most precise atomic mass measurements in Penning traps. *International Journal of Mass Spectrometry*, 349-350:107 – 122, 2013. 100 years of Mass Spectrometry. (Cited on page 16.)

[NCE+19] D.A. Nesterenko, L. Canete, T. Eronen, A. Jokinen, A. Kankainen, Y.N. Novikov, S. Rinta-Antila, A. de Roubin, and M. Vilen. High-precision measurement of the mass difference between ^{102}Pd and ^{102}Ru. *International Journal of Mass Spectrometry*, 435:204 – 208, 2019. (Cited on page 46.)

[NHJ+01] A. Nieminen, J. Huikari, A. Jokinen, J. Äystö, P. Campbell, and E.C. Cochrane. Beam cooler for low-energy radioactive ions. *Nuclear Instruments and Methods in Physics Research Section A: Accelerators, Spectrometers, Detectors and Associated Equipment*, 469(2):244 – 253, 2001. (Cited on pages 29, 46, 47, 48, 83 and 84.)

[Nie55] A.O. Nier. Determination of isotopic masses and abundances by mass spectrometry. *Science*, 121(3152):737–744, 1955. (Cited on page 14.)

[oS89] Royal Swedish Academy of Science. Press release, October 1989. (Cited on page 14.)

[Ott10] E. Otten. Searching the absolute neutrino mass in tritium β-decay—interplay between nuclear, atomic and molecular physics. *Hyperfine Interactions*, 196(1):3–23, Feb 2010. (Cited on page 16.)

[PCJY05] K. Pachucki, A. Czarnecki, U.D. Jentschura, and V.A. Yerokhin. Complete two-loop correction to the bound-electron g-factor. *Physical Review A*, 72:022108, Aug 2005. (Cited on page 15.)

[PDS13] W. Plass, T. Dickel, and C. Scheidenberger. Multiple-reflection time-of-flight mass spectrometry. *International Journal of Mass Spectrometry*, 349:134–144, 2013. (Cited on page 30.)

[PEE+12] H. Penttilä, V. V. Elomaa, T. Eronen, J. Hakala, A. Jokinen, A. Kankainen, I.D. Moore, S. Rahaman, S. Rinta-Antila, J. Rissanen, V. Rubchenya, A. Saastamoinen, C. Weber, and J. Äystö. Fission yield studies at the igisol facility. *The European Physical Journal A*, 48(4):43, Apr 2012. (Cited on page 46.)

[Pin07] David Brian Pinegar. *Tools for a Precise Tritium to Helium-3 Mass Comparison*. PhD thesis, University of Washington, 2007. (Cited on page 50.)

[Por01] J.V. Porto. Series solution for the image charge fields in arbitrary cylindrically symmetric Penning traps. *Physical Review A*, 64(2):023403, Jun 2001. (Cited on pages 67, 73 and 77.)

[PRvZ58] W. Paul, H.P. Reinhard, and U. von Zahn. Das elektrische Massenfilter als Massenspektrometer und Isotopentrenner. *Zeitschrift für Physik*, 152(2):143–182, 1958. (Cited on pages 26 and 27.)

[PyC] Jetbrains. https://www.jetbrains.com. Accessed: 2018-11-11. (Cited on page 44.)

[QtD] Qt group. https://www.qt.io. Accessed: 2018-11-08. (Cited on page 44.)

[RBCLU+12] J. Repp, C. Böhm, J.R. Crespo López-Urrutia, A. Dörr, S. Eliseev, S. George, M. Goncharov, Yu. N. Novikov, C. Roux, S. Sturm, S. Ulmer, and K. Blaum. PENTATRAP: a novel cryogenic multi-Penning-trap experiment for high-precision mass measurements on highly charged ions. *Applied Physics B*, 107(4):983–996, 2012. (Cited on pages 17 and 89.)

[RBD+12] C. Roux, C. Böhm, A. Dörr, S. Eliseev, S. George, M. Goncharov, Y.N. Novikov, J. Repp, S. Sturm, S. Ulmer, and K. Blaum. The trap design of PENTATRAP. *Applied Physics B*, 107(4):997–1005, 2012. (Cited on page 89.)

[Ris18] Alexander Rischka. *The First Direct Q_{EC} Measurement in ^{163}Ho and the Development of the High-Precision Mass Spectrometer PENTATRAP for Neutrino Physics*. PhD thesis, University of Heidelberg, 2018. (Cited on page 17.)

[RMSM06] M. Redshaw, J. McDaniel, W. Shi, and E.G. Myers. Mass ratio of two ions in a Penning trap by alternating between the trap center and a large cyclotron orbit. *International Journal of Mass Spectrometry*, 251(2-3):125–130, 2006. (Cited on page 19.)

[SAE+19] S. Sturm, I. Arapoglou, A. Egl, M. Höcker, S. Kraemer, T. Sailer, B. Tu, A. Weigel, R. Wolf, J.C. López-Urrutia, and K. Blaum. The ALPHATRAP experiment. *The European Physical Journal Special Topics*, 227(13):1425–1491, Feb 2019. (Cited on page 89.)

[SAG+98] H. Schatz, A. Aprahamian, J. Görres, M. Wiescher, T. Rauscher, J.F. Rembges, F.-K. Thielemann, B. Pfeiffer, P. Möller, K.-L. Kratz, H. Herndl, B.A. Brown, and H. Rebel. rp-process nucleosynthesis at extreme temperature and density conditions. *Physics Reports*, 294(4):167 – 263, 1998. (Cited on page 16.)

[SBB+90] H. Stolzenberg, S. Becker, G. Bollen, F. Kern, H.J. Kluge, T. Otto, G. Savard, L. Schweikhard, G. Audi, and R.B. Moore. Accurate mass determination of short-lived isotopes by a tandem Penning-trap mass spectrometer. *Physical Review Letters*, 65:3104–3107, Dec 1990. (Cited on page 14.)

[Sch14] Marc Schuh. *Simulations of the electrostatic and magnetic field properties and tests of the Penning-ion source at THe-Trap*. Master thesis, Ruperto-Carola University of Heidelberg, 2014. (Cited on page 49.)

[SEH+14] S. Streubel, T. Eronen, M. Höcker, J. Ketter, M. Schuh, R.S. van Dyck, Jr., and K. Blaum. Toward a more accurate Q-value measurement of tritium: status of THe-Trap. *Applied Physics B*, 114(1–2):137–145, 2014. (Cited on pages 22, 45, 55 and 56.)

[SHE+18] M. Schuh, F. Heiße, T. Eronen, J. Ketter, F. Köhler-Langes, S. Rau, T. Segal, W. Quint, S. Sturm, and K. Blaum. Image charge shift in high-precision Penning traps. *Physical Review A*, 2018. (Cited on pages 23, 24, 67, 77, 78, 79 and 89.)

[Sim] Simion. https://simion.com/. Accessed: 2018-11-14. (Cited on page 42.)

[SKZ+14] S. Sturm, F. Köhler, J. Zatorski, A. Wagner, Z. Harman, G. Werth, W. Quint, C.H. Keitel, and K. Blaum. High-precision measurement of the atomic mass of the electron. *Nature*, 506(7489):467–470, 2014. (Cited on pages 15 and 17.)

[SMB+17] G. Schneider, A. Mooser, M. Bohman, N. Schoen, J. Harrington, N. Schön, T. Higuchi, H. Nagahama, S. Sellner, C. Smorra, K. Blaum, Y. Matsuda, W. Quint, J. Walz, and S. Ulmer. Double-trap measurement of the proton magnetic moment at 0.3 parts per billion precision. *Science*, 358(6366):1081–1084, 2017. (Cited on page 15.)

[SMF+15] C. Smorra, A. Mooser, K. Franke, H. Nagahama, G. Schneider, T. Higuchi, S.V. Gorp, K. Blaum, Y. Matsuda, W. Quint, J. Walz, Y. Yamazaki, and S. Ulmer. A reservoir trap for antiprotons. *International Journal of Mass Spectrometry*, 389:10 – 13, 2015. (Cited on page 19.)

[SSH+17] C. Smorra, S. Sellner, J. Harrington, T. Higuchi, H. Nagahama, M.J. Borchert, T. Tanaka, M. Besirli, A. Mooser, G. Schneider, K. Blaum, Y. Matsuda, C. Ospelkaus, W. Quint, J. Walz, Y. Yamazaki, and S. Ulmer. Sixfold improved single particle measurement of the magnetic moment of the antiproton. *Nature Communications*, 8, 2017. (Cited on page 15.)

[Str14] Sebastian Dennis Streubel. *Kontrolle der Umwelteinflüsse auf THe-Trap am Beispiel der Bestimmung des Massenverhältnisses von Sauerstoff-16 zu Kohlenstoff-12*. PhD thesis, University of Heidelberg, 2014. (Cited on pages 49, 55 and 56.)

[SVWP14] T. Sriarunothai, A.F. Varon, C. Wunderlich, and C. Piltz. A trapped-ion-based quantum byte with 10(-5) next-neighbour cross-talk. *Nature Communications*, 5, 2014. (Cited on page 19.)

[SWK+13] S. Sturm, A. Wagner, M. Kretzschmar, W. Quint, G. Werth, and K. Blaum. g-factor measurement of hydrogenlike $^{28}Si^{13+}$ as a challenge to QED calculations. *Physical Review A*, 87(3):030501, Mar 2013. (Cited on pages 15, 17, 67 and 73.)

[SWSB11] S. Sturm, A. Wagner, B. Schabinger, and K. Blaum. Phase-Sensitive Cyclotron Frequency Measurements at Ultralow Energies. *Physical Review Letters*, 107(14):143003, Sep 2011. (Cited on pages 23, 57 and 76.)

[TB01] M.D. Tinkle and S.E. Barlow. Image charge forces inside conducting boundaries. *Journal of Applied Physics*, 90(3):1612–1624, 2001. (Cited on page 73.)

[USM+15] S. Ulmer, C. Smorra, A. Mooser, K. Franke, H. Nagahama, G. Schneider, T. Higuchi, S. Van Gorp, K. Blaum, Y. Matsuda, W. Quint, J. Walz, and Y. Yamazaki. High-precision comparison of the antiproton-to-proton charge-to-mass ratio. *Nature*, 524(7564):196–199, 2015. (Cited on page 15.)

[vBP61] F. v. Busch and W. Paul. Über nichtlineare resonanzen im elektrischen massenfilter als folge von feldfehlern. *Zeitschrift für Physik*, 164(5):588–594, Oct 1961. (Cited on pages 25 and 29.)

[VDacS+04] J. Verdú, S. Djekić, S. Stahl, T. Valenzuela, M. Vogel, G. Werth, T. Beier, H.-J. Kluge, and W. Quint. Electronic g-factor of hydrogenlike oxygen $^{16}O^{7+}$. *Physical Review Letters*, 92:093002, Mar 2004. (Cited on page 15.)

[vDMFS86] R.S. van Dyck, Jr., F.L. Moore, D.L. Farnham, and P.B. Schwinberg. Variable magnetic bottle for precision geonium experiments. *Review of Scientific Instruments*, 57(4):593–597, 1986. (Cited on page 14.)

[vDMFS89] R.S. van Dyck, Jr., F.L. Moore, D.L. Farnham, and P.B. Schwinberg. Number dependency in the compensated Penning trap. *Physical Review A*, 40(11):6308–6313, Dec 1989. (Cited on page 67.)

[vDPVLZ06] R.S. van Dyck, Jr., D.B. Pinegar, S. Van Liew, and S.L. Zafonte. The UW-PTMS: Systematic studies, measurement progress, and future improvements. *International Journal of Mass Spectrometry*, 251(2–3):231–242, 2006. (Cited on pages 67, 78 and 79.)

[vDSD87] R.S. van Dyck, Jr., P.B. Schwinberg, and H.G. Dehmelt. New high-precision comparison of electron and positron g-factors. *Physical Review Letters*, 59(1):26–29, Jul 1987. (Cited on page 14.)

[Vis] Microsoft visual studio. https://visualstudio.microsoft.com/. Accessed: 2018-11-14. (Cited on page 44.)

[VVB+18] L. J. Vormawah, M. Vilén, R. Beerwerth, P. Campbell, B. Cheal, A. Dicker, T. Eronen, S. Fritzsche, S. Geldhof, A. Jokinen, S. Kelly, I. D. Moore, M. Reponen, S. Rinta-Antila, S. O. Stock, and A. Voss. Isotope shifts from collinear laser spectroscopy of doubly charged yttrium isotopes. *Physical Review A*, 97:042504, Apr 2018. (Cited on page 46.)

[WBB+12] R.N. Wolf, D. Beck, K. Blaum, C. Böhm, C. Borgmann, M. Breitenfeldt, F. Herfurth, A. Herlert, M. Kowalska, S. Kreim, D. Lunney, S. Naimi, D. Neidherr, M. Rosenbusch, L. Schweikhard, J. Stanja, F. Wienholtz, and K. Zuber. On-line separation of short-lived nuclei by a multi-reflection time-of-flight device. *Nuclear Instruments and Methods in Physics Research Section A: Accelerators, Spectrometers, Detectors and Associated Equipment*, 686:82 – 90, 2012. (Cited on page 30.)

[WBB+13] F. Wienholtz, D. Beck, K. Blaum, Ch. Borgmann, M. Breitenfeldt, R. B. Cakirli, S. George, F. Herfurth, J. D. Holt, M. Kowalska, S. Kreim, D. Lunney, V. Manea, J. Menéndez, D. Neidherr, M. Rosenbusch, L. Schweikhard, A. Schwenk, J. Simonis, J. Stanja, R.N. Wolf, and K. Zuber. Masses of exotic calcium isotopes pin down nuclear forces. *Nature*, 498:346, June 2013. (Cited on page 19.)

[WD75] D.J. Wineland and H.G. Dehmelt. Principles of the stored ion calorimeter. *Journal of Applied Physics*, 46(2):919–930, 1975. (Cited on page 23.)

[WED73] D. Wineland, P. Ekstrom, and H. Dehmelt. Monoelectron oscillator. *Physical Review Letters*, 31(21):1279–1282, Nov 1973. (Cited on page 14.)

[WEMS11] R.N. Wolf, M. Eritt, G. Marx, and L. Schweikhard. A multi-reflection time-of-flight mass separator for isobaric purification of radioactive ion beams. *Hyperfine Interactions*, 199(1):115–122, Jul 2011. (Cited on page 30.)

[WHW02] S.E. Woosley, A. Heger, and T.A. Weaver. The evolution and explosion of massive stars. *Review of Modern Physics*, 74:1015–1071, Nov 2002. (Cited on page 16.)

[Wol13] H. Wollnik. History of mass measurements in time-of-flight mass analyzers. *International journal of mass spectrometry*, 349:38–46, 2013. (Cited on page 31.)

[WVST06] D.F. Winters, M. Vogel, D.M. Segal, and R.C. Thompson. Electronic detection of charged particle effects in a Penning trap. *Journal of Physics B: Atomic, Molecular and Optical Physics*, 39(14):3131, 2006. (Cited on page 23.)

[WWA+13] R.N. Wolf, F. Wienholtz, D. Atanasov, D. Beck, and K. Blaum. Isoltrap's multi-reflection time-of-flight mass separator/spectrometer. *International Journal of Mass Spectrometry*, 349:123–133, 2013. (Cited on pages 19, 30 and 31.)

[Zoh17] T.I. Zohdi. *A Finite Element Primer for Beginners: The Basics*. Springer, 2017. (Cited on pages 33, 37 and 39.)

Acknowledgments

Diese Arbeit wäre ohne die Mithilfe vieler Personen unmöglich gewesen. Gerne möchte ich im Folgenden einigen danken. Diese Auflistung hat jedoch keinen Anspruch auf Vollständigkeit. Sollte ich Sie vergessen haben, so bitte ich um Nachsicht.

Klaus Blaum:
Danke lieber Klaus, dass Du es mir ermöglicht hast, über so viele Jahre Dein Student zu sein. Es hat mit einem Praktikum im Jahr 2010 angefangen und ich bin 9 Jahre gerne bei Dir geblieben. Du hast es geschafft, eine ruhige und meist sorgenfreie Arbeitsatmosphäre zu schaffen, die von großem Vertrauen geprägt war. Die Möglichkeit, den Arbeitsrhythmus bereits früh so frei gestalten zu dürfen, war eine große Bereicherung. Auch Dein Umgang als Mensch und Arbeitgeber mit meiner Behinderung war und ist vorbildhaft! Ich hatte nie das Gefühl, dass mir hierdurch Nach- oder für mich ebenfalls genauso wichtig Vorteile entstehen. Es hat mir großen Spaß bereitet, für Dich zu arbeiten und ohne Deine großartige Unterstützung wäre die Kombination aus den wissenschaftlichen und sportlichen Erfolgen undenkbar gewesen.

Tommi Eronen:
Your time as a Postdoc in Heidelberg had a great influence on me as a master student. Your open, honest and always friendly nature gave me a great pleasure to work with you. I came gladly to Jyväskylä in February 2017 and you had just the perfect project for me. The second visit in August 2018 was also exciting when I could see how my simulation results were implemented. I'm also very grateful for all the corrections you have made to the various documents I've sent you.

Yuri Litvinov:
Thank you for agreeing to be the second referee of the thesis. I remember your lecture from 2013 with pleasure.

Rima Schüssler:
Vielen lieben Dank für das häufigere Helfen bei der Suche nach dem "Motivat"-ion. Die diversen Unterhaltungen über Themen innerhalb und außerhalb der Physik habe ich stets sehr geschätzt. Ohne Deine unermüdliche Korrekturarbeit meiner Texte wäre diese Arbeit nie auf dieses Niveau gekommen! Ich hoffe der Kontakt hält noch lange über die Zeit am MPIK hinaus.

Tom Segal:
Danke, dass Du THe-Trap am Leben erhalten und die ersten Bugs des neuen Kontrollprogramms ausgehalten hast. Auch schätze ich die anderen Blickwinkel auf die Welt, die Du mir gegeben hast.

Jochen Ketter:
Deine Dokumentationen sind bis heute legendär. Sie haben das Verstehen auch schwierigster Abläufe selbst im Nachhinein möglich gemacht hat. Die vielen Unterhaltungen und Ideen zum Image Charge Shift haben mir sehr geholfen.

Sebastian Streubel:
Deine geduldigen Erklärungen des Experiments und des Kontrollsystems haben mir sehr geholfen. Auch standest Du mir stets mit Rat und Tat zur Seite.

Martin Höcker:
Danke für die Matlab Magie, das Gefühl für schöne Plots, die neuen Messkonzepte, die Du aus den USA mitgebracht hast und vor allem Danke für eine hervorragend geschriebene Doktorarbeit. Erst durch sie konnte ich eine unabhängige Datenauswertung von Tom's Daten durchführen.

Andreas Weigel:
Die Zusammenarbeit mit Dir am FP-Versuch Raman Spektroskopie hat mir großen Spaß gemacht und Deine Arbeit beim Einstellen des Strahlganges sowie der Detektorelektronik war hervorragend.

Antoine de Roubin:
Thank you for the help with the final simulations, implementing, optimizing and analyzing the ion buncher at IGISOL and particularly for a fantastic time in Jyväskylä in August 2019.

IT Abteilung:
Danke für die Bereitstellung einer hervorragenden IT-Infrastruktur, ohne welche die Simulationen für den Image Charge Shift nicht möglich gewesen wären.

Das gesamte MPIK:
Danke für eine tolle Arbeitsatmosphäre und die stets schnellen und unkomplizierten Lösungen bei den diversen Problemen im Alltag.

Klaus Höller:
Ohne Dein Verständnis für die Kombination aus Spitzensport und Studium, wäre es nie möglich gewesen mein Studium und damit auch diese Doktorarbeit in Heidelberg durchzuhalten.

Sportpartnern und Sponsoren:
Die jahrelange treue Unterstützung diverser Partner im Sport hat wesentlich zu meiner Karriere im Sport und in der Physik beigetragen. Hätte ich meinen Sport nicht auf Weltniveau ausführen können, so hätte ich mein Physikstudium in Heidelberg recht früh abgebrochen und wäre zurück nach Köln gegangen.